

NASA Technical Memorandum 100826

Active Feed Array Compensation for Reflector Antenna Surface Distortions

(NASA-TM-100826) ACTIVE FEED ARRAY
COMPENSATION FOR REFLECTOR ANTENNA SURFACE
DISTORTIONS Ph.D. Thesis - Akron Univ., Ohio
(NASA) 177 p CSCI 20N

N88-25762

G3/32 Unclass
 0148113

Roberto J. Acosta
Lewis Research Center
Cleveland, Ohio

June 1988

NASA

ACKNOWLEDGEMENTS

I express my heartfelt gratitude to Dr. Kai-Fong Lee, dissertation advisor, for his encouragement and guidance throughout the research. I sincerely thank Dr. L. Roemer, Dr. D. Bowman, Dr. K.C. Choy, and Dr. C.S. Chen for serving in my advisory committee.

I would like to express my gratitude and appreciation to Professor S.W. Lee of University of Illinois for providing me with many perceptive insights throughout this work.

PRECEDING PAGE BLANK NOT FILMED

TABLE OF CONTENTS

	Page
SUMMARY	i
ACKNOWLEDGMENTS	ii
CHAPTER	
1. INTRODUCTION	1
2. REFLECTOR ANTENNA SECONDARY PATTERN COMPUTATION	4
2.1 Introduction	4
2.2 Description of Problem	6
2.3 Incident Field Computation	7
2.4 Aperture Integration Method	15
2.5 Aperture Integration Method and the Fast Fourier Transform (FFT)	19
2.6 Computation of the Aperture Plane Tangential Fields	22
2.7 Physical Optics Method	25
2.8 Directivity Computation	29
2.9 Numerical Results and Discussion	30
3. REFLECTOR ANTENNA SURFACE ERROR REPRESENTATION	38
3.1 Introduction	38
3.2 Description of the Problem	39
3.3 Undistorted Surface Component	41
3.4 Surface Error Component	52
3.5 Numerical Results and Discussion	57

3.6 Concluding Remarks	67
4. COMPENSATION METHOD I: TRANSMITTING APPROACH	68
4.1 Introduction	68
4.2 Determination of the Compensating Feed Array Geometry	71
4.3 Computation of the Compensating Feed Array Excitation Coefficients	74
4.4 Numerical Results and Discussion	78
5. COMPENSATION METHOD II: RECEIVING APPROACH	89
5.1 Introduction	89
5.2 Problem Description	90
5.3 Computation of the Focal Plane Fields	93
5.4 Determination of the Compensating Feed Array Geometry and Element Complex Excitation Coefficients	99
5.5 Numerical Implementation	104
5.6 Numerical Results and Discussion	108
6. SUMMARY	141
6.1 Concluding Remarks	141
6.2 Suggestion for Future Work	141
REFERENCES	143
APPENDICES	153
APPENDIX A: POWER RADIATED BY AN ARRAY FEED	154
APPENDIX B: SPECULAR REFLECTION	159
APPENDIX C: PRINCIPAL RADII OF CURVATURES OF REFLECTED WAVEFRONT	162
APPENDIX D: FOCAL PLANE FIELDS COMPUTATION BY THE RECIPROCITY PRINCIPLE	167

ACTIVE FEED ARRAY COMPENSATION FOR REFLECTOR ANTENNA
SURFACE DISTORTIONS

Roberto J. Acosta
National Aeronautics and Space Administration
Lewis Research Center
Cleveland, Ohio 44135

SUMMARY

The feasibility of electromagnetic compensation for reflector antenna surface distortions (non-random) is investigated. The performance characteristics (gain, sidelobe levels, etc.) of large satellite communication reflector antenna systems degrade as the reflector surface distorts, mainly due to thermal effects from a solar radiation. The technique developed in this dissertation can be used to maintain the antenna boresight directivity and sidelobe level independent of thermal effects on the reflector surface. With the advent of monolithic microwave integrated circuits (MMIC), a greater flexibility in array-fed reflector antenna systems can be achieved. MMIC arrays provide independent control of amplitude and phase for each of the many radiating elements in the feed array. By assuming a known surface distortion profile, a simulation study is carried out to examine the antenna performance as a function of feed array size and number of elements. Results indicate that the compensation technique can effectively control boresight directivity (within 1-3 dB of the undistorted) and sidelobe level (within 1-5 dB of the undistorted) under peak surface distortion in the order of tenth of a wavelength. Furthermore, the computational ease of the compensation technique allows it to be implemented adaptively in a large satellite reflector antenna system.

CHAPTER 1

INTRODUCTION

Future space communication multibeam antenna system will utilize large reflector surfaces. Maintaining the surface accuracy of this large reflector antennas is important, particularly when high gain (higher than 50 dB) and low sidelobes (lower than -30 dB) are required. Reflector surface errors are generally classified into the following types:

- (i) Random surface error in the order of several mils due to manufacturing imperfection (Refs. 1-3).
- (ii) Large-scaled surface error in the order of inches due to thermal, gravitational and other effects (Ref. 4).

It is the large-scale surface error that is of interest in this dissertation work. Methods for reducing this type of surface error include the use of better antenna supporting structure, better thermally-insensitive material, and mechanically tunable surfaces. A different approach is to compensate for the degraded antenna performance due to surface distortions by using an active phased array feed. The later approach is becoming increasingly attractive due to recent advances in monolithic microwave integrated circuits (MMIC). MMIC arrays provide independent control of amplitude and phase for each of the many radiating elements in the feed array. Surface error reduction methods (mechanical/material) and surface error

compensation techniques (electromagnetically) are complementary, each approach can further improve the antenna performance independently of the other.

This dissertation investigates surface error compensation techniques for large scale surface distortions. In chapter 2, techniques for calculating the reflector antenna secondary pattern are presented. A special emphasis is placed on the aperture integration and the physical optics methods. These techniques are necessary tools in evaluating the reflector antenna performance (directivity, sidelobe levels, etc.).

In chapter 3, a method for uniquely representing the surface errors of a distorted reflector antenna is developed. The distorted reflector surface (numerically specified) is separated into two components: an undistorted surface component (represented by a best fit paraboloid) and a surface error component (expanded into a fourier series). Correlation between surface error spectral components and antenna radiation performance is examined. The result is compared with the ones obtained by using a spline interpolation algorithm.

Chapter 4 presents one of the two approaches for calculating the compensating feed array complex excitations, namely the indirect conjugate field matching (ICFM) approach. It is "indirect" because the compensating feed array excitations are determined by using the transmitting mode and the reciprocity theorem. The design of the compensating feed array (array size, number of elements, etc.) and its relation to the surface distortion are examined.

Chapter 5 presents the second compensation approach based on the receiving mode, namely the direct conjugate field matching (DCFM) approach. It is "direct" because the compensating array excitations are determined by integrating directly the induced surface currents on the reflector under a receiving condition. In contrast to the first approach, the DCFM allows the reflector be illuminated by an incident plane wave with a tapered amplitude. The level of taper can effectively control the sidelobe level of the compensated antenna pattern. A case study is presented for comparing results between the DCFM and ICFM techniques.

Finally, concluding remarks are given and some future work evolving from this dissertation research are discussed in chapter 6.

CHAPTER 2

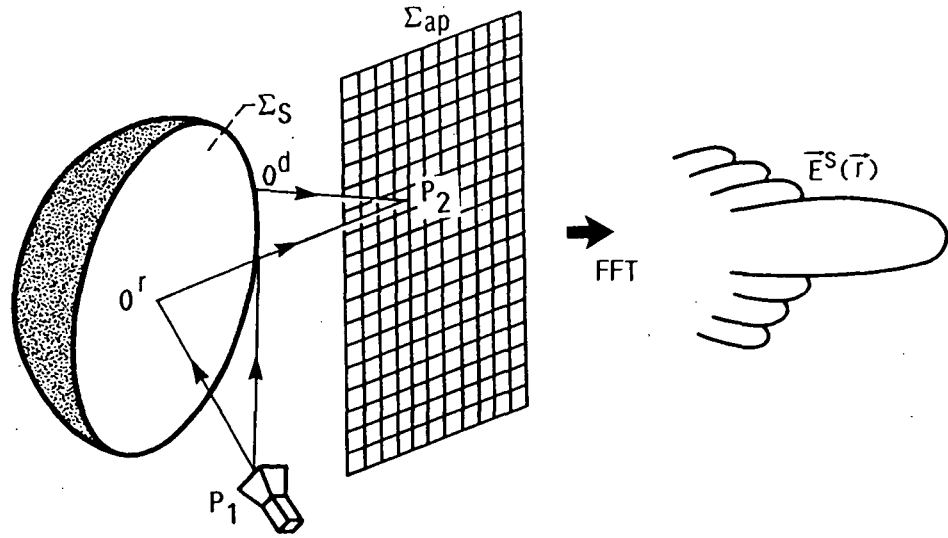
REFLECTOR ANTENNA SECONDARY PATTERN COMPUTATION

2.1 Introduction

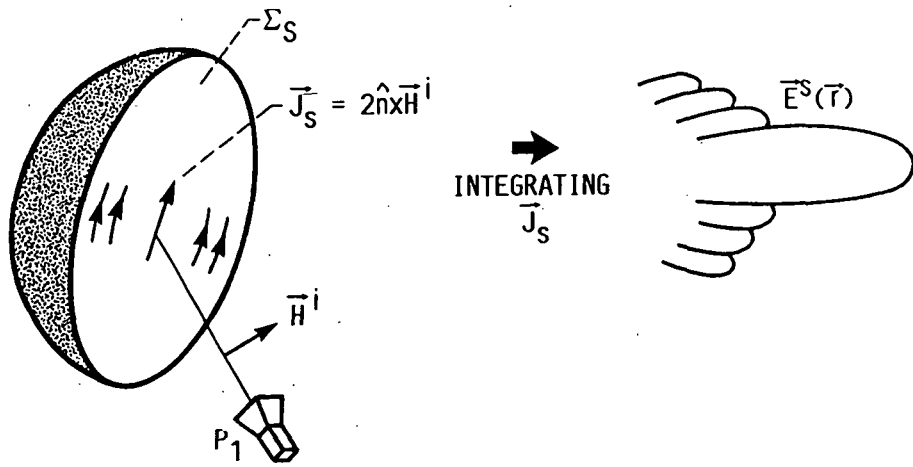
Reflector antennas are widely used in communication satellite systems because they provide high gain at low cost. In analysing reflector antennas the computation of the secondary pattern is the main concern. The basic techniques for calculating the scattered vector fields from a reflector surface has been extensively developed in the open literature (Refs. 5 to 25). The best known of these techniques are the ones based upon aperture integration and physical optics methods.

(i) Aperture Integration Method (AI, Fig. 1(a)). The fields on the aperture plane Σ_{ap} are first calculated by tracing a reflected ray $P_1 O^r P_2$ using geometrical optics (GO) theory and an edge diffracted ray $P_1 O^d P_2$ using geometrical theory of diffraction (GTD). The fields over the aperture plane Σ_{ap} are then integrated via a fast fourier transform algorithm (FFT) to obtain the scattered vector fields.

(ii) Physical Optics Method (PO, Fig. 1(b)). The induced currents on the reflector surface Σ_s is approximated by $2 \cdot \hat{n} \times \vec{H}^i$. Where \vec{H}^i is the incident magnetic field intensity on the surface, and \hat{n} is the surface normal. An integration of this current over the curved reflector surface Σ_s gives the scattered vector fields.



(a) Aperture integration method.



(b) Physical optics.

1 Methods for calculating the scattered vector fields $\vec{E}^s(r)$ from a reflector surface

The exact solution of the scattered vector field can be expanded in a high-frequency asymptotic series (Refs. 26 to 27), namely,

$$\vec{E}^s(r) \sim e^{-jKS(r)} (\vec{A}_0(r) + K^{-1/2} \vec{A}_1(r) + K^{-1} \vec{A}_2(r) + \dots) \text{ for } K \rightarrow \infty \quad (2.1)$$

Where K is the free space wavenumber.

The two pattern computational methods described above recover terms in (2.1) to various degrees, as summarized in Table 1.

TABLE 1. - ACCURACY AND LIMITATIONS OF PO AND AI

Methods	Accuracy	Limitation
AI (with GO rays and no edge diffracted rays)	Recover \vec{A}_0	Not accurate for wide-angle sidelobes
PO	Recover \vec{A}_0 and partial \vec{A}_1	
AI (with GO rays and edge diffracted rays)	Recover \vec{A}_0 and \vec{A}_1	Infinite field at caustics

A detailed description of the computation of the incident field and the power radiated by the feed source is presented in section 2.3. The AI and PO methods are described in sections 2.4 and 2.7 respectively. A numerical discussion is presented in section 2.8.

2.2 Description of Problem

The goal of reflector antenna secondary pattern computation can be described as follows: Given the feed element characteristics (location, polarization and element pattern) and reflector surface

characteristics (x, y, z , its first and second derivatives), it is required to compute the scattered vector field at an arbitrary observation point in the far-field zone. The geometry of the problem under consideration is depicted in Fig. 2.

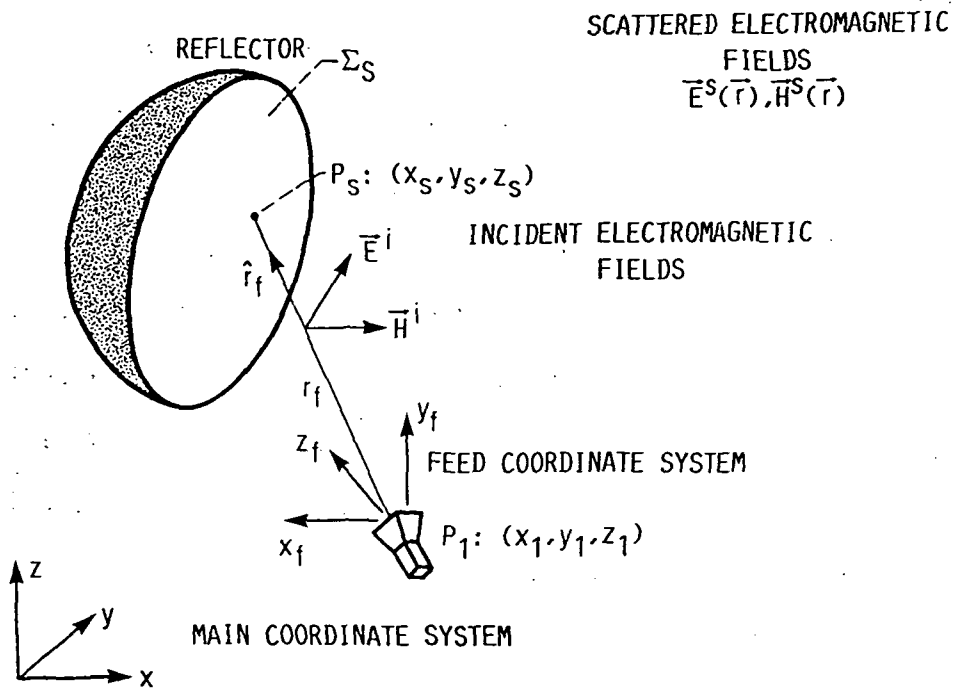
The reflector is shown in the main coordinate system (x, y, z). The feed coordinate system (x_f, y_f, z_f) facilitates the description of the feed polarization and radiation characteristics. This coordinate system is related to the main coordinate system by a set of Eulerian angles (Ref. 29). The time factor $e^{-j\omega t}$ is suppressed throughout. It is assumed that the feed source has a well defined "phased center" at P_1 with coordinates (x_1, y_1, z_1), and radiates a spherical wave denoted by (\vec{H}^i, \vec{E}^i) . If the feed source is an array, each element in the array is considered separately. The secondary pattern of the array-fed reflector antenna is then obtained by vectorially adding the individual element scattered fields. The conducting reflector surface may be described by an analytical equation or by a set of points. For the numerically specified case, an interpolating technique (Refs. 30 to 32) should be used for obtaining the required surface derivatives (first and second derivatives).

2.3 Incident Field Computation

The radiated electric and magnetic fields from the feed source have the following asymptotic form

$$\vec{E}^i(r_f) \sim \frac{e^{-jKr_f}}{r_f} \vec{F}(\theta_f, \phi_f) \quad (2.2a)$$

$$\vec{H}^i(r_f) \sim \frac{\hat{r}_f \times \vec{E}^i(r_f)}{Z} \quad (2.2b)$$



- 2 Geometry for calculating the scattered electromagnetic vector fields from a reflector antenna

Where (r_f, θ_f, ϕ_f) are spherical coordinates of an arbitrary observation point in the feed coordinate system, Z is the wave impedance, $\vec{F}(\theta_f, \phi_f)$ is a vector function describing the feed source radiation pattern, $K = 2\pi/\lambda$ is the wavenumber, λ is the wavelength, and r_f is the distance from the source to an arbitrary point in the reflector surface. The vector function $\vec{F}(\theta_f, \phi_f)$ in Eq. (2.2a) can be approximated (Ref. 23) by Eq. (2.3).

$$\vec{F}(\theta_f, \phi_f) = \hat{\theta}_f UE(\theta_f) (ae^{j\psi} \cos \phi_f + b \sin \phi_f) + \hat{\phi}_f UH(\theta_f) (b \cos \phi_f - ae^{j\psi} \sin \phi_f) \quad (2.3)$$

where $UE(\theta_f)$ is the feed E-plane pattern and $UH(\theta_f)$ is the corresponding H-plane pattern. $a, b,$ and ψ are the feed polarization parameters:

TABLE 2. - FEED POLARIZATION PARAMETERS

Polarization type	a	b	ψ
Linear X	1	0	0
Linear Y	0	1	0
Right-hand circular (RHCP)	0.707	0.707	90°
Left-hand circular (LHCP)	0.707	0.707	-90°

Typically the element pattern can be approximated by a $(\cos(\theta_f))^q$ function that is,

$$UE(\theta_f) = (\cos(\theta_f))^{qE} \quad (2.4a)$$

$$UH(\theta_f) = (\cos(\theta_f))^{qH} \quad (2.4b)$$

If Eqs. (2.4a) and (b) are used to represent the feed radiation pattern, the power radiated by a single feed source is given as

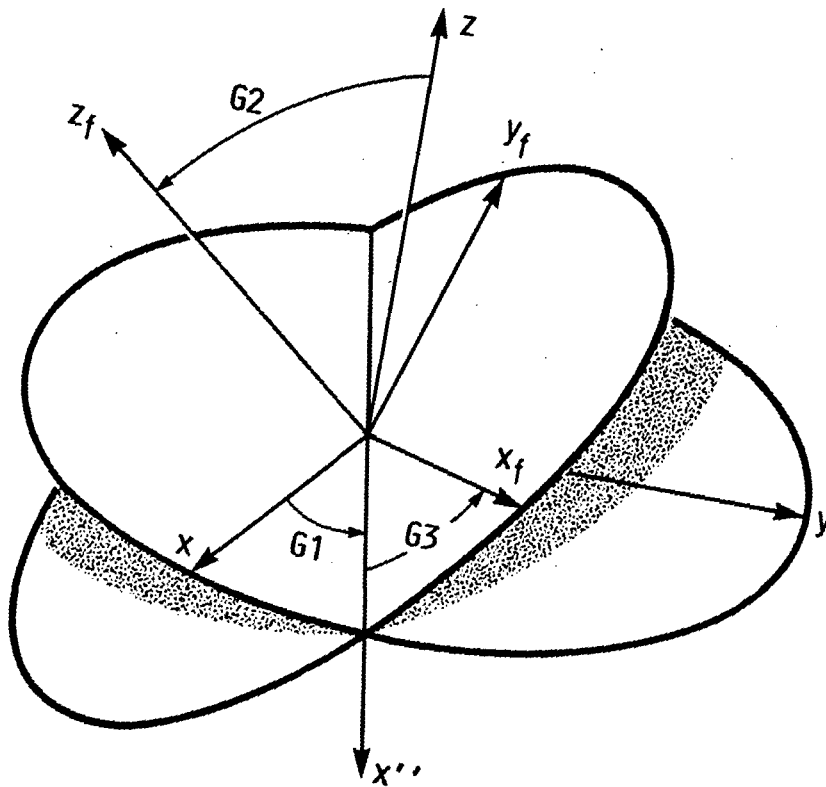
$$P_{\text{rad}} = \frac{(qE + qH + 1)}{60(2qE + 1)(2qH + 1)} \quad (2.5)$$

For a feed array with M elements (Ref. 33) the power radiated is given by Eq. (2.6).

$$P_{\text{rad}} = \sum_{m=1}^M \sum_{n=1}^M I_m I_n^* A_{mn} \quad (2.6)$$

where I_m is the m -th element complex excitation, \bar{A} is a square matrix. The derivation for the matrix \bar{A} is included in appendix A. The radiated power of an antenna is an important quantity, since it is used in the computation of its directivity (section 2.8).

Figure 3 illustrates the Eulerian angles (G_1, G_2, G_3) which determine the rotational relationship between the main coordinate system (x, y, z) and the feed coordinate system (x_f, y_f, z_f). The definition of these angles are as follows. The angle G_1 describes a counterclockwise (ccw) rotation about the z axis which brings the x axis to the x'' axis aligned with the line of nodes (line of intersection between $x-y$ and x_f-y_f planes), angle G_2 defines a rotation about the line of nodes in a ccw sense as indicated so that



3 Illustration of the Eulerian angles

this brings the z axis to z_f , and angle G_3 is another rotation about the z_f axis and aligns the x'' axis with the x_f axis in a ccw sense.

In general the feed coordinate system orientation is expressed relative to the main coordinate system by a set of three orthogonal unit vectors $(\hat{x}_f, \hat{y}_f, \hat{z}_f)$. Let these unit vectors be expressed by:

$$\hat{x}_f = a_{x1} \hat{x} + a_{x2} \hat{y} + a_{x3} \hat{z} \quad (2.7a)$$

$$\hat{y}_f = a_{y1} \hat{x} + a_{y2} \hat{y} + a_{y3} \hat{z} \quad (2.7b)$$

$$\hat{z}_f = a_{z1} \hat{x} + a_{z2} \hat{y} + a_{z3} \hat{z} \quad (2.7c)$$

Then, the Eulerian angles are given by:

$$G_1 = \tan^{-1} \left(\frac{a_{z1}}{-a_{z2}} \right) \quad (2.8a)$$

$$G_2 = \tan^{-1} \left(\frac{\sqrt{1 - a_{z3}^2}}{a_{z3}} \right) \quad (2.8b)$$

$$G_3 = \tan^{-1} \left(\frac{a_{x3}}{a_{z1} \times a_{x2} - a_{x1} \times a_{z2}} \right) \quad (2.8c)$$

It can be shown that

$$(\hat{x}_f \hat{y}_f \hat{z}_f)^T = \overset{=}{B} (\hat{x} \hat{y} \hat{z})^T \quad (2.9)$$

where

$$\overset{=}{B} = \begin{bmatrix} b_{11} & b_{12} & b_{13} \\ b_{21} & b_{22} & b_{23} \\ b_{31} & b_{32} & b_{33} \end{bmatrix} \quad (2.10)$$

in which the elements of the Eulerian matrix $\overset{=}{B}$ are defined as follows:

$$b_{11} = \cos G_1 \cos G_3 - \sin G_1 \cos G_2 \sin G_3 \quad (2.11a)$$

$$b_{12} = \sin G_1 \cos G_3 + \cos G_1 \cos G_2 \sin G_3 \quad (2.11b)$$

$$b_{13} = \sin G_2 \sin G_3 \quad (2.11c)$$

$$b_{21} = -\cos G_1 \sin G_3 - \sin G_1 \cos G_2 \cos G_3 \quad (2.11d)$$

$$b_{22} = -\cos G_1 \cos G_2 \cos G_3 - \sin G_1 \sin G_3 \quad (2.11e)$$

$$b_{23} = \sin G_2 \cos G_3 \quad (2.11f)$$

$$b_{31} = \sin G_1 \sin G_3 \quad (2.11g)$$

$$b_{32} = -\cos G_1 \sin G_2 \quad (2.11h)$$

$$b_{33} = \cos G_2 \quad (2.11i)$$

Thus, a point on the reflector surface with coordinates P_S :

(x_S, y_S, z_S) in the main coordinate system is transformed into the feed coordinate system through the transformation.

$$\begin{bmatrix} x_{fS} \\ y_{fS} \\ z_{fS} \end{bmatrix} = \mathbf{B} \begin{bmatrix} x_S - x_1 \\ y_S - y_1 \\ z_S - z_1 \end{bmatrix} \quad (2.12)$$

where (x_1, y_1, z_1) is the origin of feed coordinate system indicating its transformation with respect to the main coordinate system. The corresponding spherical coordinates for this point is given by

$$r_f = \sqrt{(x_{fS}^2 + y_{fS}^2 + z_{fS}^2)} \quad (2.13a)$$

$$\theta_f = \cos^{-1} \left(\frac{z_{fS}}{r_f} \right) \quad (2.13b)$$

$$\phi_f = \tan^{-1} \left(\frac{y_{fS}}{x_{fS}} \right) \quad (2.13c)$$

The incident electric and magnetic fields are obtained from Eqs. (2.2a), (b) and (2.13a) to (c). Notice that $\vec{E}^i(r_f)$ and $\vec{H}^i(r_f)$ are in the feed coordinate system. Let the spherical vector components of $\vec{E}^i(r_f)$ and $\vec{H}^i(r_f)$ be denoted by

$$\vec{E}^i(r_f) = (E_{rf}, E_{\theta f}, E_{\phi f})^T \quad (2.14a)$$

$$\vec{H}^i(r_f) = \frac{\vec{r}_f \times \vec{E}^i(r_f)}{Z} = (H_{rf}, H_{\theta f}, H_{\phi f})^T \quad (2.14b)$$

The incident field is converted from spherical into rectangular components by using the following transformation equations:

$$(H_{xf}, H_{yf}, H_{zf})^T = \bar{D} (H_{rf}, H_{\theta f}, H_{\phi f})^T \quad (2.15a)$$

$$(E_{xf}, E_{yf}, E_{zf})^T = \bar{D} (E_{rf}, E_{\theta f}, E_{\phi f})^T \quad (2.15b)$$

Where \bar{D} is defined by:

$$\bar{D} = \begin{bmatrix} \sin \theta_f \cos \phi_f & \cos \theta_f \cos \phi_f & -\sin \phi_f \\ \sin \theta_f \sin \phi_f & \cos \theta_f \sin \phi_f & \cos \phi_f \\ \cos \theta_f & -\sin \theta_f & 0 \end{bmatrix} \quad (2.16)$$

Finally, the incident field \vec{E}^i and \vec{H}^i in the feed coordinate system (x_f, y_f, z_f) is transformed into the main coordinate system (x, y, z) by using the following equations:

$$\begin{bmatrix} E_x \\ E_y \\ E_z \end{bmatrix} = \begin{matrix} =T \\ B \end{matrix} \begin{bmatrix} E_{xf} \\ E_{yf} \\ E_{zf} \end{bmatrix} \quad (2.17a)$$

$$\begin{bmatrix} H_x \\ H_y \\ H_z \end{bmatrix} = \begin{matrix} =T \\ B \end{matrix} \begin{bmatrix} H_{xf} \\ H_{yf} \\ H_{zf} \end{bmatrix} \quad (2.17b)$$

Where \vec{B} is given by 2.10.

2.4 Aperture Integration Method

The Aperture Integration Method is illustrated in Fig. 4. The surface Σ_g is a Huygen surface enclosing the reflector and feed. This surface can be of arbitrary shape (typically spherical, cylindrical, etc). For the special case of a planar surface Σ_{ap} (aperture plane) located in the radiation side of the reflector (the field over the shadow portion Σ_{SH} are assumed to be zero), the tangential fields on the aperture plane and the radiated far-fields are related by a Fourier transform (Ref. 6). The equivalence principle (Ref. 9) provides the basis for obtaining the radiated far-fields from the tangential \vec{E} and \vec{H} at Σ_{ap} . Note that the aperture plane Σ_{ap} is taken perpendicular to the z-axis.

Let the tangential electric and magnetic field at Σ_{ap} be denoted by \vec{E}_{ap} and \vec{H}_{ap} respectively. Consider the following vector functions:

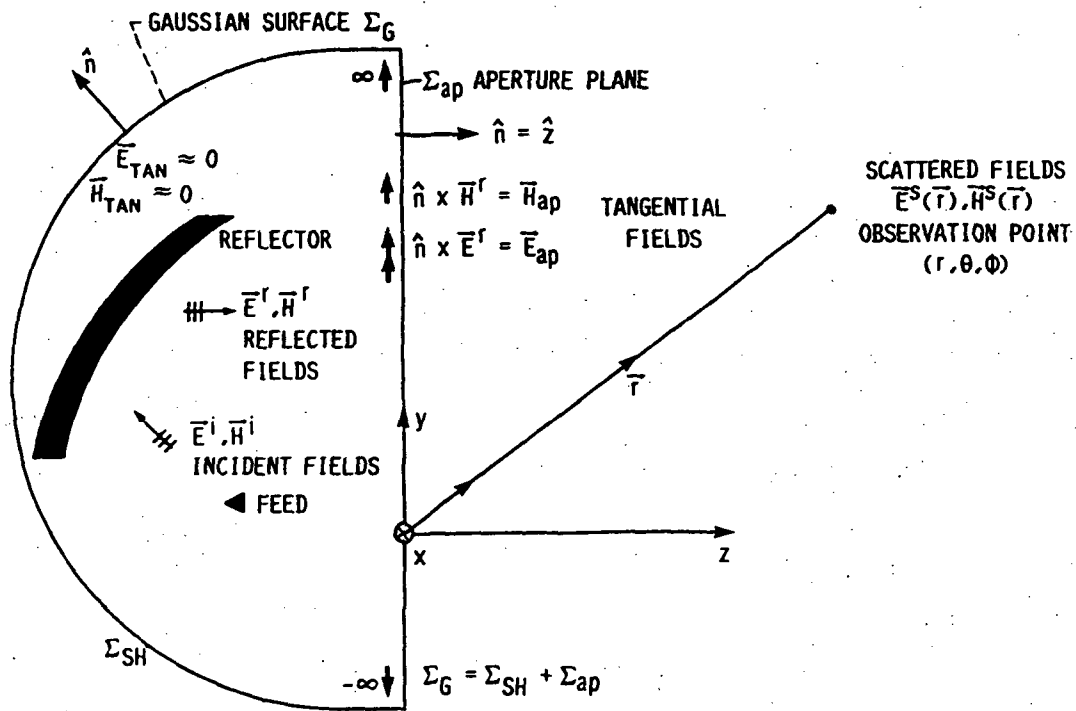
$$\vec{f}(u,v) = \iint_{\Sigma_{ap}} \vec{E}_{ap}(x,y) e^{jK(ux + vy)} dx dy \quad (2.18a)$$

$$\vec{g}(u,v) = \iint_{\Sigma_{ap}} \vec{H}_{ap}(x,y) e^{jK(ux + vy)} dx dy \quad (2.18b)$$

where $u = \sin \theta \cos \phi$

$v = \sin \theta \sin \phi$

$K = 2\pi/\lambda$



4 Aperture and observation parameters for constructing the aperture integration (AI) formulation

(r, θ, ϕ) spherical coordinates of the far-field observation point.

Since the aperture fields are tangent to the x - y plane, then

$$\vec{f}(u, v) = f_x(u, v)\hat{x} + f_y(u, v)\hat{y} \quad (2.19a)$$

$$\vec{g}(u, v) = g_x(u, v)\hat{x} + g_y(u, v)\hat{y} \quad (2.19b)$$

The radiated far-fields from a current distribution can be obtained using potential theory (Ref. 10). In the aperture plane Σ_{ap} the induced currents are given by the following

$$\vec{J}_s = \hat{n} \times \vec{H}^r \quad (\text{Electric current}) \quad (2.20a)$$

$$\vec{J}_{ms} = -\hat{n} \times \vec{E}^r \quad (\text{Magnetic current}) \quad (2.20b)$$

Where \vec{E}^r, \vec{H}^r are reflected electric and magnetic fields (section 2.6). The vector potential corresponding to the two induced currents (far-field approximation) are obtained from the following equations.

$$\vec{A}(\mathbf{r}) = \frac{\mu e}{4\pi r} e^{-jKr} \iint_{\Sigma_{ap}} (\hat{n} \times \vec{H}^r) e^{-jK(\hat{r} \cdot \vec{r}')} dx dy \quad (2.21a)$$

$$\vec{F}(\mathbf{r}) = \frac{\epsilon e}{4\pi r} e^{-jKr} \iint_{\Sigma_{ap}} -(\hat{n} \times \vec{E}^r) e^{-jK(\hat{r} \cdot \vec{r}')} dx dy \quad (2.21b)$$

where, \vec{A} and \vec{F} are the magnetic and electric vector potential respectively.

$$\hat{r} = \hat{x} \sin \theta \cos \phi + \hat{y} \sin \theta \sin \phi + \hat{z} \cos \theta \quad (2.21c)$$

$$\vec{r}' = x \hat{x} + y \hat{y} \quad (2.21d)$$

In the far-field region, \vec{E}^s and \vec{H}^s are related as in a spherical TEM wave,

$$\vec{E}^s(\mathbf{r}) = -\frac{\hat{r} \times \vec{H}^s(\mathbf{r})}{Z} \quad (2.22)$$

The far-fields $\vec{E}^s(r)$ and $\vec{H}^s(r)$ expressed in terms of vector potential functions $\vec{A}(r)$ and $\vec{F}(r)$ are given by,

$$\vec{E}^s(r) = -j\omega \vec{A}(r) + j\omega Z \hat{r} \times \vec{F}(r) \quad (2.23a)$$

$$\vec{H}^s(r) = -j\omega \vec{F}(r) - \frac{j\omega}{Z} \hat{r} \times \vec{A}(r) \quad (2.23b)$$

Equations (2.23a) and (b) imply that both electric (\vec{J}_s) and magnetic currents (\vec{J}_{ms}) are included in the evaluation of far fields. If only the electric current or the magnetic current is present, the far-field electric field $\vec{E}^s(r)$ is determined by $\vec{A}(r)$ or $\vec{F}(r)$ alone. From the field equivalence principle (Love's equivalence principles) formulations, three different expressions arise for $\vec{E}^s(r)$, namely,

(1) Using both \vec{J}_s and \vec{J}_{ms} ;

$$E_{\theta}^s = \frac{jKe^{-jKr}}{4\pi r} (f_x \cos \phi + f_y \sin \phi + Z \cos \theta (g_y \cos \phi - g_x \sin \phi)) \quad (2.24a)$$

$$E_{\phi}^s = \frac{jKe^{-jKr}}{4\pi r} (\cos \theta (f_y \cos \phi - f_x \sin \phi) - Z (g_y \sin \phi + g_x \cos \phi)) \quad (2.24b)$$

(2) Using $2\vec{J}_s$ (Assume the aperture surface is a perfect electric conducting surface)

$$E_{\theta}^s = \frac{jKZ e^{-jKr} \cos \theta}{2\pi r} (g_y \cos \phi - g_x \sin \phi) \quad (2.24c)$$

$$E_{\phi}^s = \frac{jKZ e^{-jKr} \cos \theta}{2\pi r} (g_y \sin \phi - g_x \cos \phi) \quad (2.24d)$$

(3) Using $2\vec{J}_{ms}$ (Assume the aperture surface is a perfect electric conducting surface)

$$E_{\theta}^s = \frac{jKe^{-jKr}}{2\pi r} (f_x \cos \phi + f_y \sin \phi) \quad (2.24e)$$

$$E_{\phi}^S = \frac{jKe^{-jKr \cos \theta}}{2\pi r} (f_y \cos \phi - f_x \sin \phi) \quad (2.24f)$$

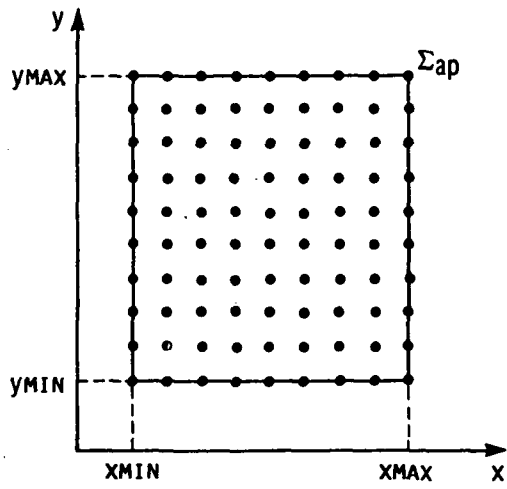
The results given by (2.24a) and (b) are the average of (2.24c) to (f) respectively. It requires the values of both tangential electric and magnetic fields at \sum_{ap} . In practice it is more convenient to use either (2.24c) to (f) since they require the knowledge of only either the tangential magnetic or electric field over the aperture plane. This method is exact if the fields everywhere in \sum_G are known accurately. For electrically large reflectors the fields in the aperture plane will be usually small outside an area defined by the projection of the reflector boundary on the aperture plane.

2.5 Aperture Integration Method and the Fast Fourier Transform (FFT)

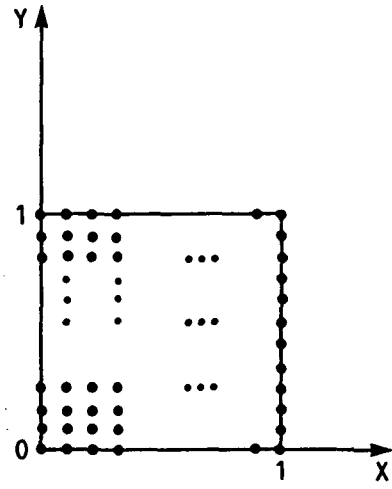
To employ an FFT algorithm, the integrals in (2.18a) and (b) must be rearranged so that the form of integral matches the definition given by the FFT subroutines. In general, two dimensional FFT subroutines assumes the function being considered to be periodic in x and in y with period of 1 in both dimensions. Hence, a typical aperture plane grid as shown in Fig. 5, must be scaled accordingly.

To illustrate the transformation of the given integrals into integrals with an FFT format consider the equation (2.18a) and extend the result to (2.18b). Each of these equations have two components, (f_x, f_y) for Eq. (2.18a) and (g_x, g_y) for (2.18b). First consider the component f_x in Eq. (2.18a).

$$f_x(u, v) = \int_{y_{\min}}^{y_{\max}} \int_{x_{\min}}^{x_{\max}} E_{ax}(x, y) e^{jK(ux+vy)} dx dy \quad (2.25)$$



(a) Aperture grid.



(b) FFT grid.

5 Typical aperture plane grid and its corresponding FFT grid

where E_{ax} is the x-component of $\vec{E}_{ap}(x,y)$ in (2.18a). Using the following change in variable,

$$X = \frac{x - x_{min}}{x_{max} - x_{min}} \quad (2.26a)$$

$$Y = \frac{y - y_{min}}{y_{max} - y_{min}} \quad (2.26b)$$

and $(x_{max} - x_{min}) = L_x$, $(y_{max} - y_{min}) = L_y$, Eq. (2.25) becomes,

$$f_x(u,v) = C_1 \int_0^1 \int_0^1 E_{ax}(x_{min} + X(L_x), y_{min} + Y(L_y)) e^{jK(u(L_x)X + v(L_y)Y)} dX dY \quad (2.27a)$$

where

$$C_1 = (L_x)(L_y)e^{jK(u x_{min} + v y_{min})} \quad (2.27b)$$

The expression $E_{ax}(x_{min} + (L_x)X, y_{min} + (L_y)Y)$ within the integral may be interpreted as $E_{ax}(x,y)$ scaled in $FE_{ax}(a,b)$ within the limits $0 < a < 1$ and $0 < b < 1$ (Fig. 5b). $FE_{ax}(a,b)$ may be approximated by

$$FE_{ax}(a,b) = \sum_{n=N1}^{N2} \sum_{m=M1}^{M2} T_{mn} e^{j2\pi(mX+nY)} \quad (2.28)$$

where T_{mn} are the Fourier coefficients obtained by using an FFT subroutine. For example if one considers a 32 by 32 FFT grid points, then

$$N1 = M1 = -15 \quad \text{and} \quad N2 = M2 = 16$$

From (2.27a) and (b) and (2.28),

$$f_x(u,v) = C_1 \int_0^1 \int_0^1 \sum_{n=N1}^{N2} \sum_{m=M1}^{M2} T_{mn} \text{EXP}(m,n,u,v) dX dY \quad (2.28a)$$

where

$$\text{EXP}(m,n,u,v) = e^{jK((m\lambda+u(L_x))X+(n\lambda+v(L_y))Y)} \quad (2.28b)$$

Interchanging the summation and integral signs and noting that

$$\int_0^1 e^{jKcx} dx = \frac{\sin\left(\frac{\pi C}{\lambda}\right) e^{j\left(\frac{\pi C}{\lambda}\right)}}{\left(\frac{\pi C}{\lambda}\right)} \quad (2.29)$$

the expression for f_x is given by,

$$f_x(u,v) = C_1 \sum_{n=N1}^{N2} \sum_{m=M1}^{M2} C_{mn} e^{j\frac{\pi}{\lambda}(m+n)} \text{SF}(m,n,u,v) \quad (2.30a)$$

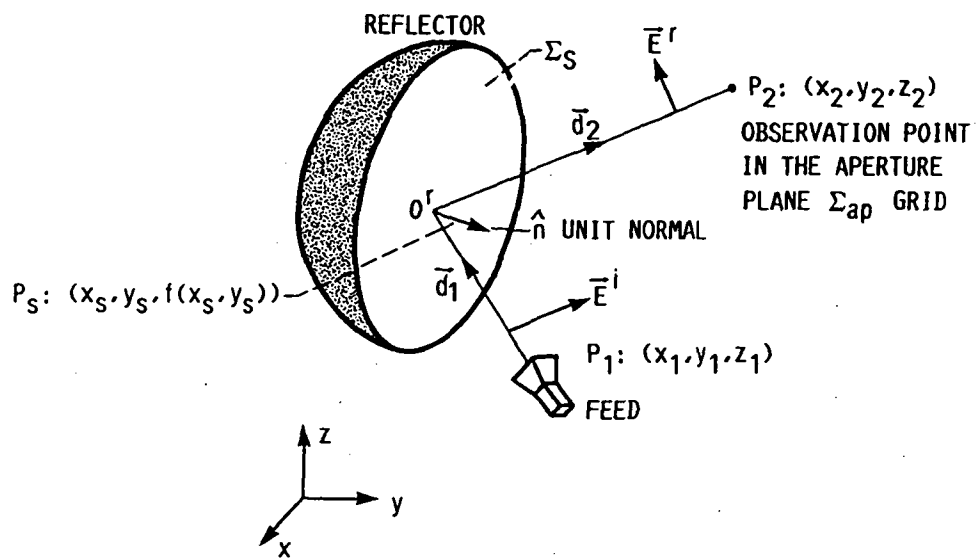
where $\text{SF}(m,n,u,v)$ is given by,

$$\text{SF}(m,n,u,v) = \frac{\sin\left(\frac{\pi}{\lambda}(m\lambda + u(L_x))\right) \sin\left(\frac{\pi}{\lambda}(n\lambda + v(L_y))\right)}{\left(\frac{\pi}{\lambda}(m\lambda + u(L_x))\right) \times \left(\frac{\pi}{\lambda}(n\lambda + v(L_y))\right)} \quad (2.30b)$$

In summary, to evaluate the integrals (2.18a) and (b) one needs to first calculate T_{mn} of Eq. (2.28) by an FFT algorithm and then calculate $f_x(u,v)$ via (2.30a) and (b). The other components (f_y, g_x, g_y) in Eqs. (2.18a) and (b) can be easily transformed into an FFT format (Eq. (2.30a) and (b)) following a similar approach.

2.6 Computation of the Aperture Plane Tangential Fields

The geometry for calculating the tangential fields on the aperture plane is depicted in Fig. 6. For a given feed point P_1 and an observation point P_2 , a reflection point O^r may exist on the reflector surface. This point is called a specular point (Ref. 34). This type of reflection satisfies Snell's law of reflection. The



6 Geometrical optics ray tracing for calculating the aperture fields

reflector surface is assumed to be a perfect conductor. Appendix B presents a method for obtaining the specular points on the reflector surface. The geometrical optics approximation of the reflected electric fields (Refs. 35 - 36) at an observation point P_2 is given by,

$$\vec{E}^r(P_2) = DF e^{-jKd_2} (2(\hat{n} \cdot \vec{E}^i)\hat{n} - \vec{E}^i) \quad (2.31)$$

where,

d_2 distance between P_2 and O^r

\vec{E}^i incident electric field (see Section 2.3)

\hat{n} the reflector surface unit normal at O^r

DF divergence factor given by Eq. (2.32)

$$DF = \frac{1}{\sqrt{1 + (d_2/R_1^r)}} \frac{1}{\sqrt{1 + (d_2/R_2^r)}} \quad (2.32)$$

R_1^r, R_2^r Principal radii of curvature of the reflected wavefront passing through O^r .

Appendix C contains a derivation of the principal radii of curvature of the reflected wavefront for a general surface of revolution. In summary for a given P_1 and P_2 , there may be more than one reflection point. Then the total reflected field at the aperture grid is the superposition of the contribution from each reflection point. If for any P_2 there is no specular reflection point on the the reflector surface, then the reflected field is zero. The approximation in Eq. (2.31) only takes into account the reflected rays. To improve the computation of the tangential fields on the aperture plane one may include edge diffracted rays (Refs. 37 to 43).

A similar expression to (2.31) can be found (Ref. 23) for this type of fields. In general edge diffracted fields and reflected field are superimposed at the aperture plane. For electrically large reflector antennas the contribution due to edge diffracted fields is very small and generally can be neglected.

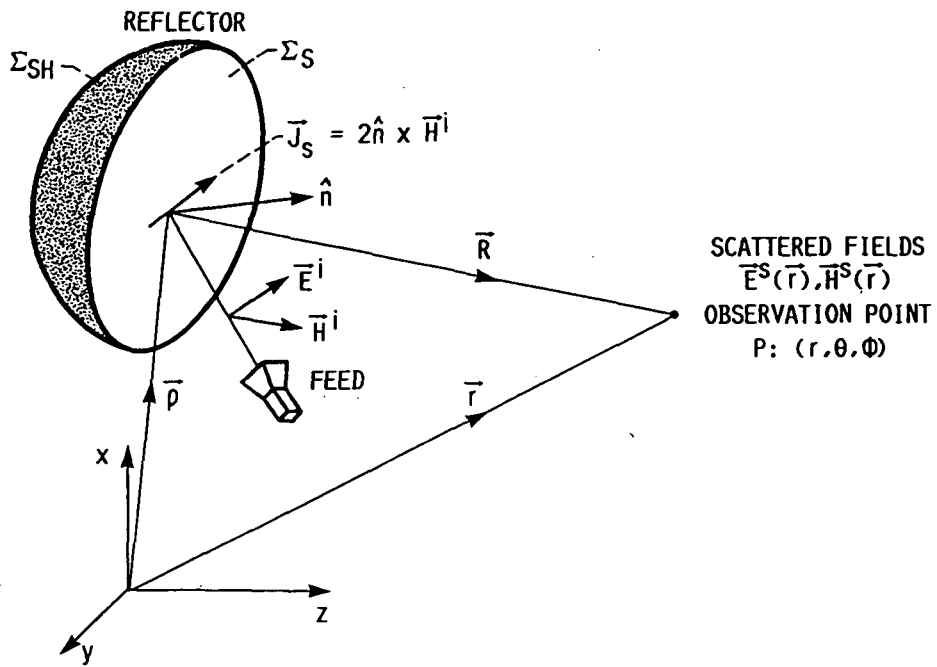
2.7 The Physical Optics Method

The currents which excite the scattered field are induced on the reflector surface (assuming a perfect conductor) by an incident electromagnetic field \vec{E}_i, \vec{H}_i (see section 2.3). Figure 7 illustrates the geometry for calculating the scattered fields using the physical optics approach. In the physical optics method the induced surface current distribution (Refs. 5 to 6) is approximated by

$$\vec{J}_S = 2(\hat{n} \times \vec{H}_i) \quad \text{On the illuminated side } \Sigma_S. \quad (2.33a)$$

$$\vec{J}_S = 0 \quad \text{On the shadowed side } \Sigma_{SH}. \quad (2.33b)$$

These approximations to the induced surface current are valid when the reflector size, the radii of curvature of the reflector surface, and the radius of curvature of the incident wavefront are all much larger than the wavelength. A fringing current component can be added to improve the current accuracy (Ref. 44). The fringing component is needed for applications that require the scattered fields to be known over wide observation angles away from the antenna boresight.



- 7 Geometry and parameters for constructing the physical optics (PO) formulation

The electromagnetic field solution to Maxwell's equations due to an electric current distribution in an unbounded region (Ref. 6) is given by Eqs. (2.34a) and (b).

$$\vec{E}^s(r) = \frac{-j}{4\pi\omega\epsilon} \iint_{\Sigma_s} ((\vec{J}_s \cdot \vec{\nabla})\vec{\nabla} + K^2 \vec{J}_s) \frac{e^{-jKR}}{R} dS \quad (2.34a)$$

$$\vec{H}^s(r) = \frac{-j}{4\pi\omega\mu} \iint_{\Sigma_s} (j\omega\mu\vec{J}_s \times \vec{\nabla}) \frac{e^{-jKR}}{R} dS \quad (2.34b)$$

Equations (2.34a) and (b) are valid at any arbitrary observation point $P:(r,\theta,\phi)$. In the integrands of Eqs. (2.34a) and (b) the operator $\vec{\nabla}$ operates on the coordinates of the source current alone. Expanding all the terms involved in the above integrands one obtains the following expressions,

$$\vec{\nabla} \left(\frac{e^{-jKR}}{R} \right) = \left(jK + \frac{1}{R} \right) \frac{e^{-jKR}}{R} \hat{R} \quad (2.35a)$$

$$(\vec{J}_s \cdot \vec{\nabla}) \vec{\nabla} \left(\frac{e^{-jKR}}{R} \right) = \left\{ -K^2 (\vec{J}_s \cdot \hat{R}) \hat{R} + \frac{3}{R} \left(jK + \frac{1}{R} \right) (\vec{J}_s \cdot \hat{R}) \hat{R} - \frac{\vec{J}_s}{R} \left(jK + \frac{1}{R} \right) \right\} \frac{e^{-jKR}}{R} \quad (2.35b)$$

where

$$K = \frac{2\pi}{\lambda} = \omega\sqrt{\mu\epsilon} \quad \text{wavenumber}$$

R The distance from source element to the observation point P .
A far-field approximation to Eqs. (2.34a) and (b) can be obtained by considering

$$R \cong r - \hat{r} \cdot \vec{r}' \quad (\text{for phase terms}) \quad (2.36a)$$

$$R \cong r \quad (\text{for amplitude terms}) \quad (2.36b)$$

and by taking into account only $1/R$ variations in Eq. (2.35a) and (b). With these approximations, Eqs. (2.34a) and (b) are simplified into the following forms.

$$\vec{E}^s(\vec{r}) = \frac{-j\omega\mu}{4\pi r} e^{-jKr} \iint_{\Sigma_s} (\vec{J}_s - (\vec{J}_s \cdot \hat{r})\hat{r}) e^{jk\hat{\rho} \cdot \hat{r}} dS \quad (2.37a)$$

$$\vec{H}^s(\vec{r}) = \frac{j\omega\epsilon}{4\pi r} e^{-jKr} \iint_{\Sigma_s} \left(\frac{\mu}{\epsilon}\right)^{1/2} (\vec{J}_s \times \hat{r}) e^{jk\hat{\rho} \cdot \hat{r}} dS \quad (2.37b)$$

where r is such that the following constraint is satisfied.

$$r > \frac{2D^2}{\lambda} \quad (2.38)$$

D the diameter of reflector antenna

λ the operating wavelength

The surface integration appearing in Eqs. (2.37a) and (b) is performed on the reflector curved surface. The differential area is

$$dS = dx dy \sqrt{1 + \left(\frac{df}{dx}\right)^2 + \left(\frac{df}{dy}\right)^2} \quad (2.38)$$

The square root factor above is commonly known as the Jacobian of the surface. It can be shown that the integral (2.37) and dS given in (2.38) may be represented in terms of a series of many two-dimensional Fourier transforms (Ref. 45). Typically, one needs the first few terms in this series to achieve a converging solution. The physical optics radiation integrals may be evaluated in many different ways (Refs. 12 to 14) and its efficient evaluation has been a challenging problem.

2.8 Directivity Computation

The far-zone electric field is usually divided into two orthogonal polarizations. Following Ludwig's definition 3 (Ref. 46), the following unit polarization vectors are introduced:

$$\hat{R} = \hat{\theta} (a_p e^{j\psi_p} \cos \phi + b_p \sin \phi) + \hat{\phi} (-a_p e^{j\psi_p} \sin \phi + b_p \cos \phi) \quad (2.39a)$$

$$\hat{C} = \hat{\theta} (a_p e^{-j\psi_p} \sin \phi - b_p \cos \phi) + \hat{\phi} (-a_p e^{-j\psi_p} \cos \phi + b_p \sin \phi) \quad (2.39b)$$

where (a_p, b_p, ψ_p) are the far-field polarization parameters. These are related to the feed polarization parameters (section 2.3). For a single reflector these relationships are given by;

$$a_p = a, \quad b_p = b, \quad \psi_p = \psi + \pi \quad (2.40)$$

For example, a feed linearly polarized in the \hat{y}_f direction will produce a secondary radiation beam linearly polarized in the \hat{y} direction. A RHCP feed produces an LHCP secondary beam. For dual reflectors this relation may be more complex depending upon the coordinate systems and offset direction used. It is best to determine this relation in each individual problem.

If the secondary pattern can be expressed as (Eqs. (2.23a) and (b) and (2.37a) and (b),

$$\vec{E}^s(r) = \frac{e^{-jKr}}{r} \left(\hat{\theta} E_{\theta}^s + \hat{\phi} E_{\phi}^s \right) \quad (2.41)$$

the reference polarization expression for $\vec{E}^s(r)$ is given by (2.42a),

$$ER(r) = \vec{E}^s \cdot (\hat{R}^*) \quad (2.42a)$$

and the cross polarization expression is given by (2.42b)

$$EC(r) = \vec{E}^s \cdot (\hat{C}^*) \quad (2.42b)$$

The directivity associated with the reference polarization is defined by

$$DR(\theta, \phi) = \frac{4\pi}{P_{\text{rad}}} (\vec{E}^s \cdot \hat{R}^*)^2 \quad r^2/Z \quad (2.43a)$$

Similarly the directivity for the cross polarization is defined by

$$DC(\theta, \phi) = \frac{4\pi}{P_{\text{rad}}} (\vec{E}^s \cdot \hat{C}^*)^2 \quad r^2/Z \quad (2.43b)$$

where P_{rad} is the power radiated by the feed source (section 2.3).

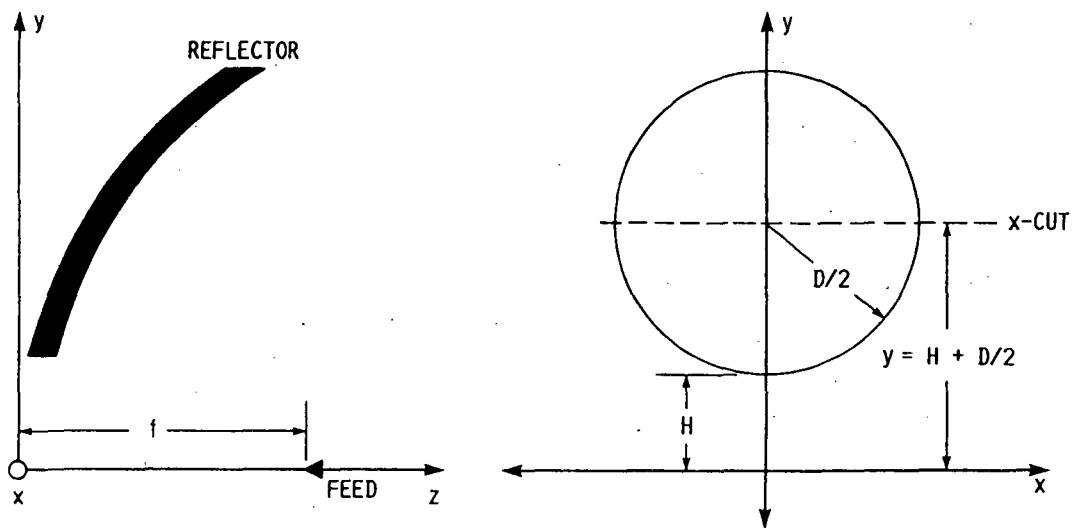
2.9 Numerical Results and Discussion

This section presents some numerical results to establish numerical accuracy of the aperture integration method (GO and GO + GTD) and the physical optics method. Far-field radiation patterns are presented for the following offset parabolic reflector configuration.

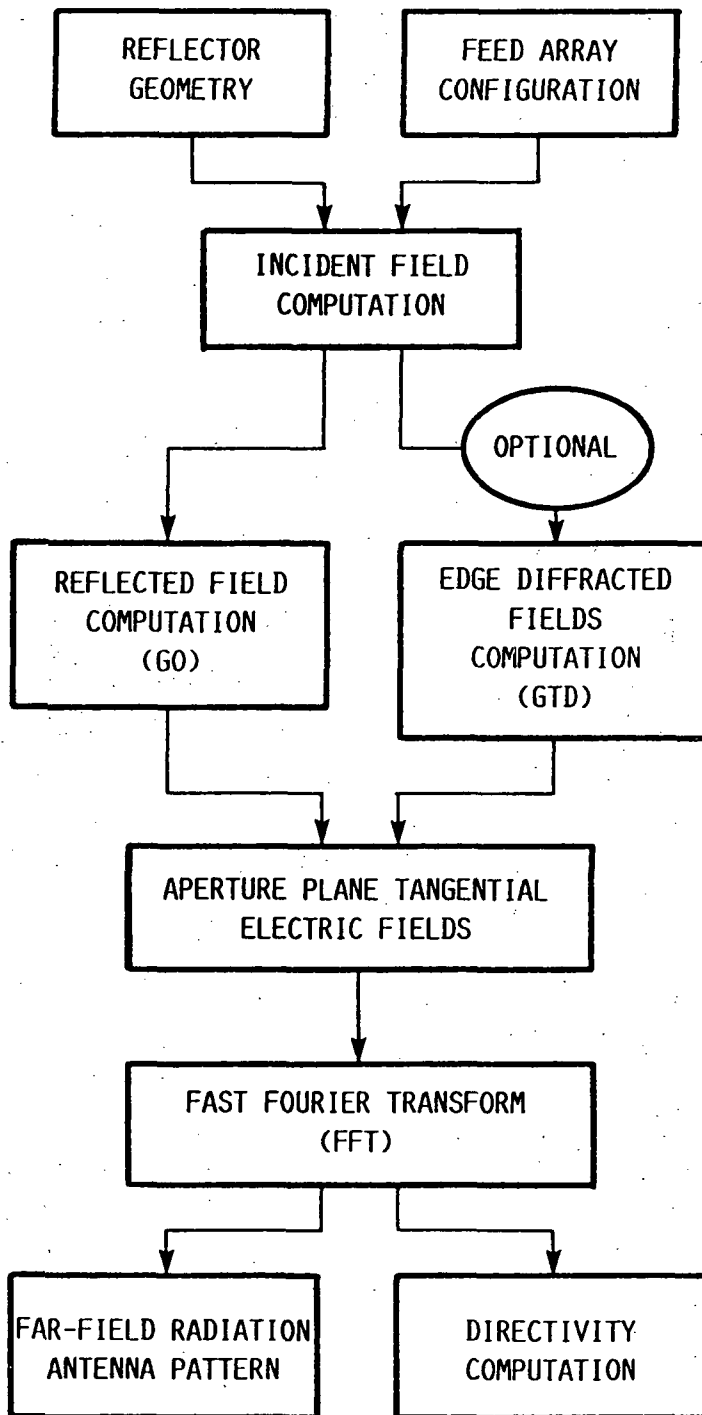
Reflector geometry: D = 257.89 λ diameter
 (refer to Fig. 8) f = 637.48 λ focal length
 H = 135.51 λ offset height

Other parameters: Frequency = 30 GHz
 Aperture points = 200x200
 \hat{y} -polarized feed
 -18 dB edge taper

A block diagram of a computer implementation (Refs. 22 to 23) for the aperture integration method (GO and GO + GTD) and the physical optics method are presented in Figs. 9(a) and (b) respectively. The

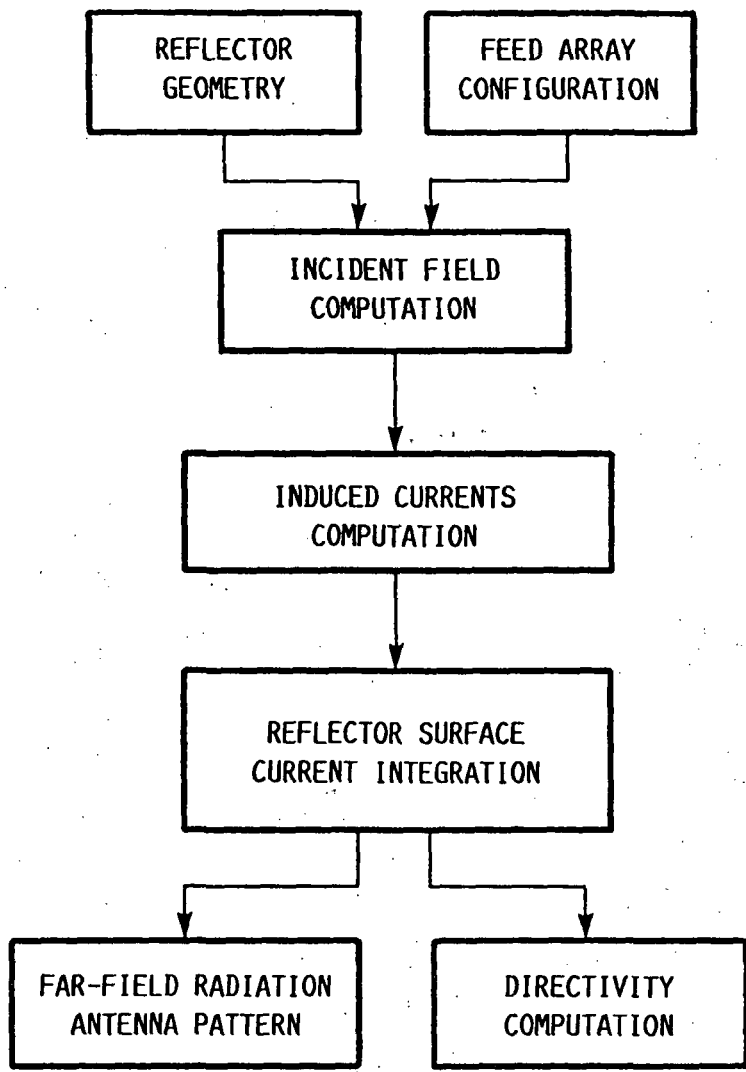


8 Offset parabolic reflector geometry



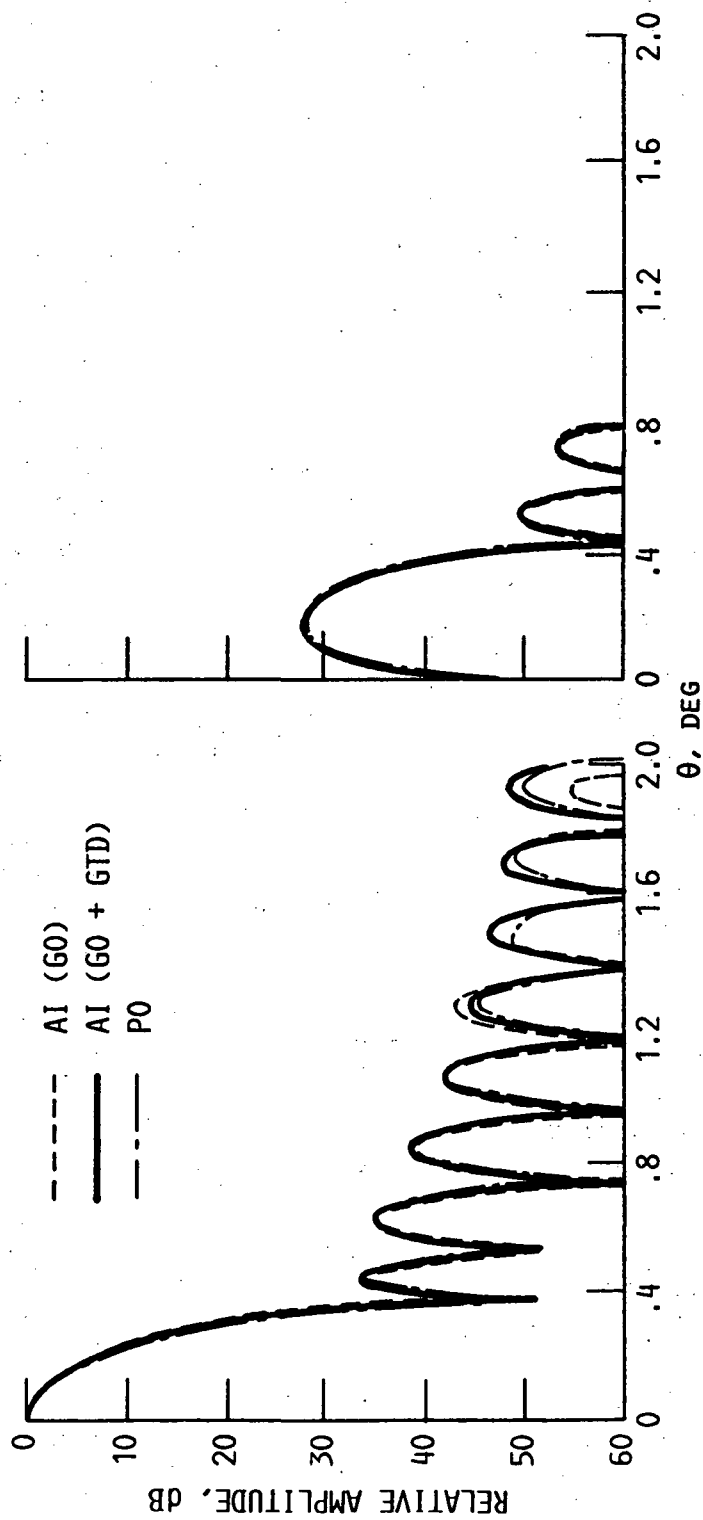
(a) Aperture integration algorithm.

- 9 Block diagram of a computer implementation for calculating the secondary radiation pattern of a reflector antenna



(b) Physical optics algorithm.

Fig. 9. - Concl.



(a) Reference polarization (Boresight case).

(b) Cross polarization (Boresight case).

10 Secondary radiation pattern (E-plane cut)

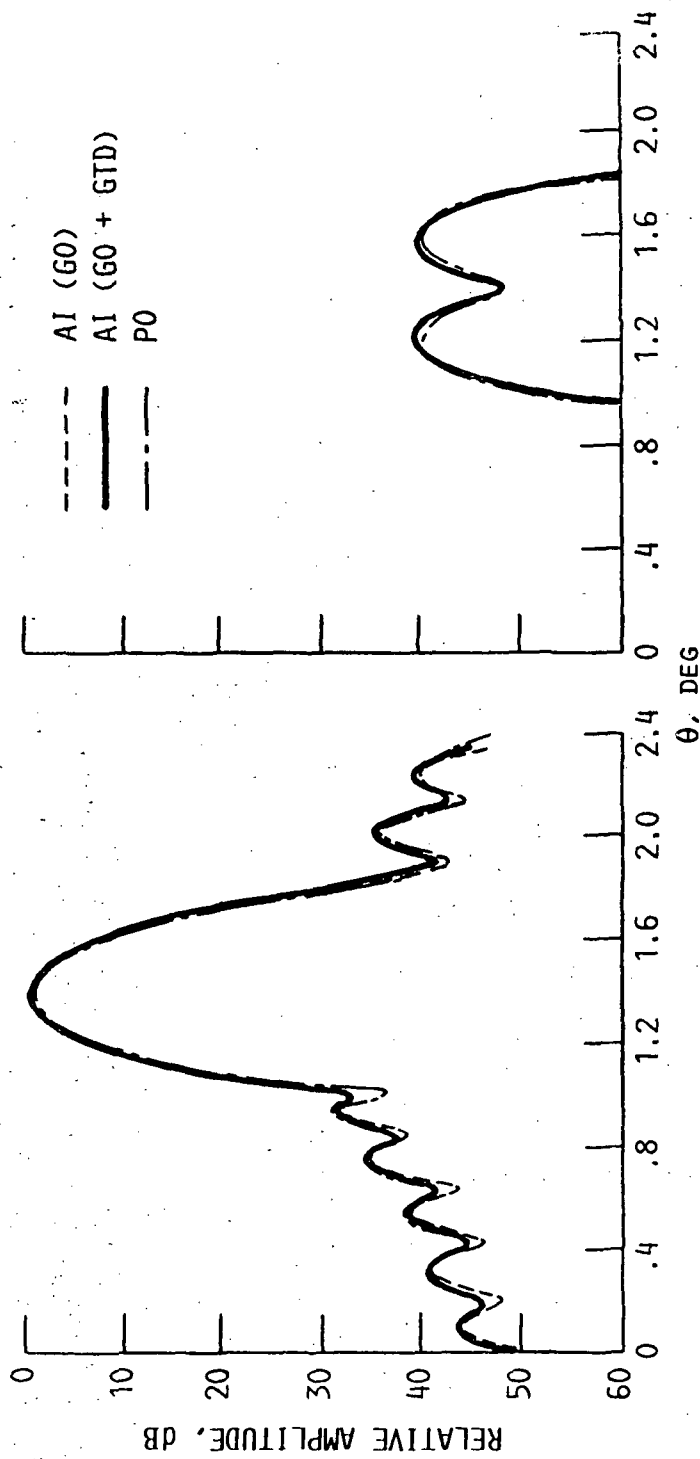


Fig. 10. - Concl.

block diagrams describes all the computational routines that are required by both methods.

Figures 10(a) and (b) show far-field radiation patterns (reference and cross polarizations) for the boresight case and Figs. 10(c) and (d) show a 6-beamwidth scanning case. As expected radiation patterns calculated by each method are in good agreement. The gain, half-power beamwidth (HPBW) and first sidelobe level for the boresight case are shown in Table 3.

TABLE 3. - SUMMARY OF ANTENNA PERFORMANCE

Method	AI (GO)	AI (GO + GTD)	PO
Gain (dB)	56.88	56.89	56.85
HPBW (deg)	0.279	0.281	0.283
SLL (dB)	-33.89	-35.2	-33.3

Note that the gain and HPBW obtained in all the methods are almost identical. The differences comes in the sidelobe level. The addition of the edge diffracted rays into the AI method improves the sidelobe level prediction, although for such electrically large reflector it does not seem to change the gain or the HPBW.

Table 4 shows the computation times for the methods on an IBM 370 computer.

TABLE 4. - SUMMARY OF COMPUTER EXECUTION TIMES

Method	AI (GO)	AI (GO + GTD)	PO
IBM 370 C.P.U. (sec)	80	150	100

The AI (GO) method was the fastest as expected. The FFT algorithm makes this method numerically efficient. If the edge diffracted rays option is used then the AI become the slowest, but the most accurate. The PO is a trade-off between sidelobe accuracy and computational time.

CHAPTER 3

REFLECTOR ANTENNA SURFACE ERROR REPRESENTATION

3.1 Introduction

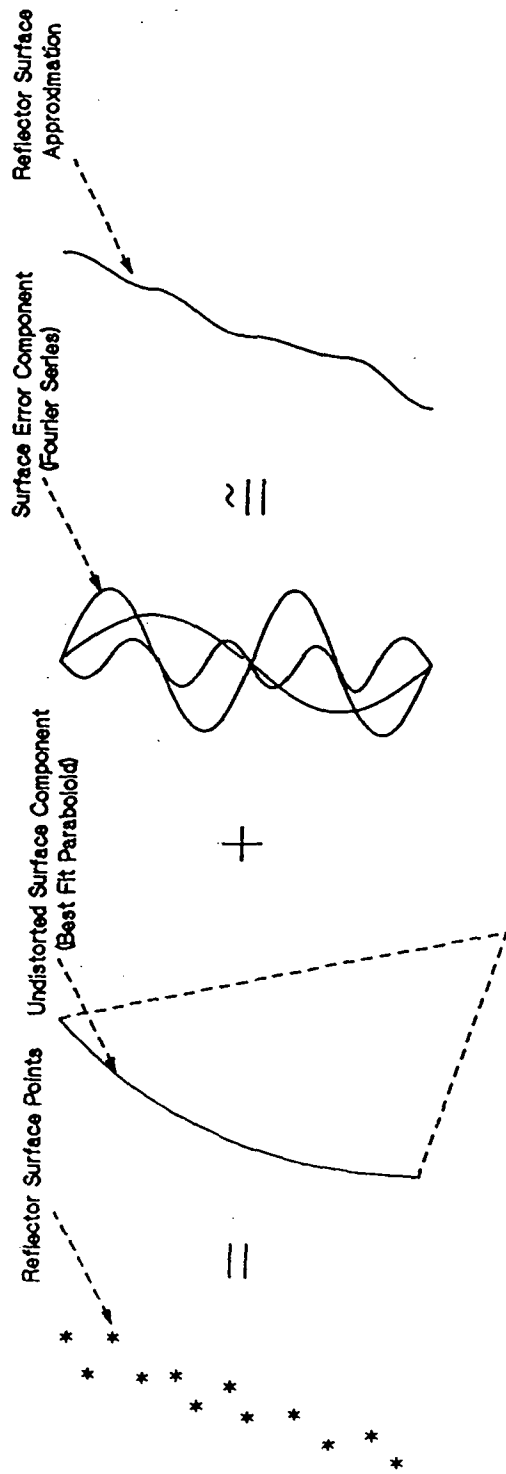
Reflector antennas in a space environment are subject to continuous variation in temperature distribution, and are thus distorted from its true geometrical shape (typically parabolic, hyperbolic, elliptical, etc.). The distorted reflector surface has in general a very complicated shape and hence can not be represented with an exact analytical expression. The analysis of a distorted reflector antenna defined by a set of discrete surface points require the use of numerical techniques. Many numerical techniques for analyzing the performance of reflector antennas defined by a set of points have been extensively reported in the open literature (Refs. 4, 32, 47 to 53). The most popular of these techniques represents the reflector surface either globally or locally by using polynomial splines (Refs. 54 and 55). The polynomial splines and other techniques require the surface points to be orderly labeled. This is an undesired characteristic because it can result in a nonunique approximation for the desired reflector surface. The order of the spline polynomial necessary to best fit the reflector surface points is in general unknown a priori, and therefore it involves a trial and error procedure for checking the accuracy of the interpolation.

The distorted reflector surface points can be best approximated by two analytical components, an undistorted surface component and a surface error component. The undistorted surface component is a best fit paraboloid polynomial for the given set of points and the surface error component is the deviation of the actual surface points from the best fit paraboloid. This residual error component is then described with a sinusoidal Fourier series expansion. This approximation technique is insensitive to the labeling of the reflector surface points and can describe the surface errors very accurately. Similar to a time signal the spatial spectrum of the surface error component is unique to the reflector under consideration. Therefore spatial spectra can be utilized as a performance index for comparing distortion profile in reflector antennas.

3.2 Description of the Problem

The best analytical representation of the distorted reflector antenna surface points that uniquely identifies surface errors can be obtained as follows: the reflector surface points are separated into two components, a best fit paraboloid component and a sinusoidal Fourier series expansion of the residual. Figures 11 illustrates a conceptual layout of the problem under consideration.

In analyzing large reflector antenna performance it is necessary to accurately characterize the reflector surface points. Any derivation from its ideal geometry causes the antenna performance to degrade. The surface error component provides an independent performance index against which distorted reflector antennas can be compared. The surface error component by definition is a sinusoidal



11 Distorted reflector surface points separated into an undistorted surface component and a surface error component

Fourier series expansion of the difference between the actual reflector surface points and the best fit paraboloid geometry. Informations such as root mean square value (RMS), peak surface error and two-dimensional distortion profile can be calculated from the surface error component. The Fourier coefficients in the series expansion represents the spatial spectrum that uniquely identifies the distorted reflector under study. The best fit parabolic surface represents the reflector antenna surface in an average sense. When the surface error is zero the best fit paraboloid surface reduces to the ideal or the design surface geometry.

3.3 Undistorted Surface Component

A generalized two dimensional second order polynomial (paraboloid of revolution) is given by Eq. (3.1).

$$S(x,y,z) = a_1 x^2 + a_2 y^2 + a_3 z^2 + a_4 xy + a_5 yz + a_6 zx + a_7 x + a_8 y + z + a_{10} \quad (3.1)$$

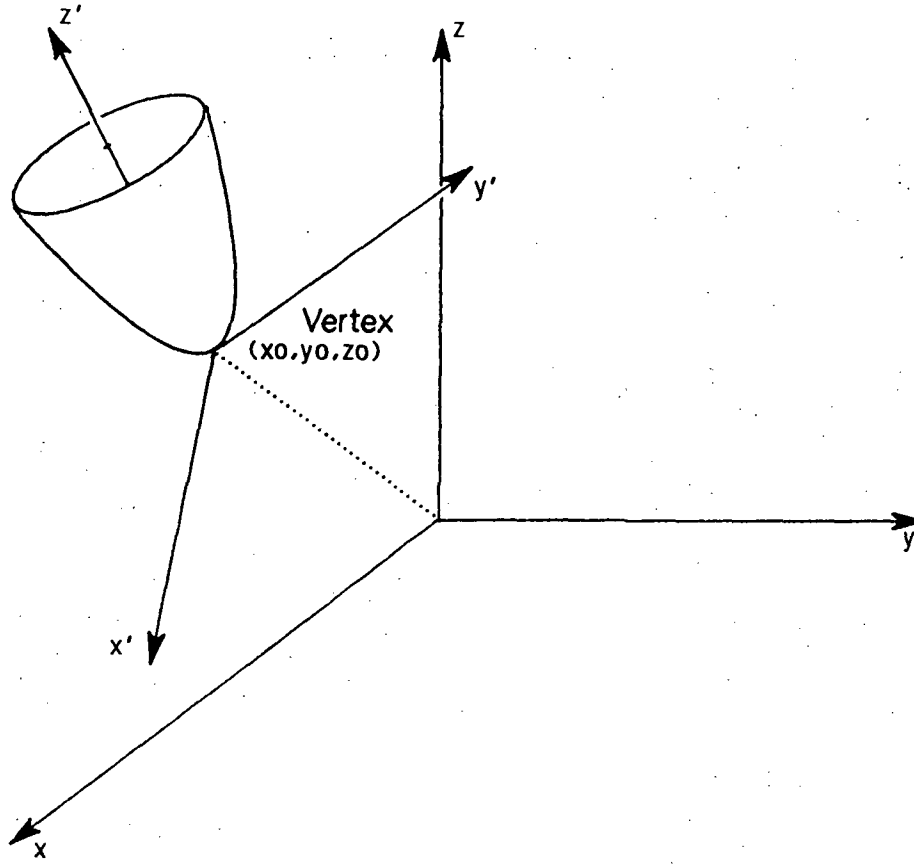
This polynomial form can be transformed into a different coordinate system in which Eq. (3.1) will have the following form,

$$S'(x',y',z') = x'^2 + y'^2 - FL z' \quad (3.2)$$

Where FL is a constant. Figure 12 shows a generalized parabola of revolution (Eq. (3.1)), the (x,y,z) coordinate system and the (x',y',z') coordinate system. These two coordinate system are related by set a of Eulerian rotations (Ref. 56) and a translation. Let the distorted reflector surface be represented by

$$DS(x_i, y_i, z_i) = 0, i=1, N \quad (3.3)$$

Using the method of least squares (Ref. 57) the distorted reflector surface points from an approximating parabolic polynomial given by Eq. (3.1) can be determined in the manner described below.



12 Illustration of a generalized paraboloid of revolution

The minimization index is defined as

$$I = \sum_{i=1}^N (DS(x_i, y_i, z_i) - S(x_i, y_i, z_i))^2 \quad (3.4)$$

where

$DS(x_i, y_i, z_i)$ nth order surface polynomial representing the distorted reflector surface points.

$S(x_i, y_i, z_i)$ the approximating parabolic polynomial in Eq. (3.1)

N total number surface points

Substituting Eq. (3.1) and (3.3) into (3.4) yields the following result,

$$I = \sum_{i=1}^N (a_1 x_i^2 + a_2 y_i^2 + a_3 z_i^2 + a_4 x_i y_i + a_5 y_i z_i + a_6 z_i x_i + a_7 x_i + a_8 y_i + z_i + a_{10})^2 \quad (3.5)$$

For minimum I it is required that,

$$\frac{\partial I}{\partial a_1} = \frac{\partial I}{\partial a_2} = \frac{\partial I}{\partial a_3} = \dots = \frac{\partial I}{\partial a_{10}} = 0 \quad (3.6)$$

Equation (3.6) results in the following set of equation,

$$\frac{\partial I}{\partial a_1} = \sum_{i=1}^N 2 (S(x_i, y_i, z_i)) x_i^2 = 0 \quad (3.7a)$$

$$\frac{\partial I}{\partial a_2} = \sum_{i=1}^N 2 (S(x_i, y_i, z_i)) y_i^2 = 0 \quad (3.7b)$$

$$\frac{\partial I}{\partial a_3} = \sum_{i=1}^N 2 (S(x_i, y_i, z_i)) z_i^2 = 0 \quad (3.7c)$$

$$\frac{\partial I}{\partial a_4} = \sum_{i=1}^N 2 (S(x_i, y_i, z_i)) x_i y_i = 0 \quad (3.7d)$$

$$\frac{\partial I}{\partial a_5} = \sum_{i=1}^N 2 (S(x_i, y_i, z_i)) y_i z_i = 0 \quad (3.7e)$$

$$\frac{\partial I}{\partial a_6} = \sum_{i=1}^N 2 (S(x_i, y_i, z_i)) x_i z_i = 0 \quad (3.7f)$$

$$\frac{\partial I}{\partial a_7} = \sum_{i=1}^N 2 (S(x_i, y_i, z_i)) x_i = 0 \quad (3.7g)$$

$$\frac{\partial I}{\partial a_8} = \sum_{i=1}^N 2 (S(x_i, y_i, z_i)) y_i = 0 \quad (3.7h)$$

$$\frac{\partial I}{\partial a_{10}} = \sum_{i=1}^N 2 (S(x_i, y_i, z_i)) 1 = 0 \quad (3.7i)$$

Equations (3.7a) to (i) can be arranged in a matrix form given by,

$$\bar{R} (\bar{X}) = \bar{E} \quad (3.8)$$

where \bar{R} is a 9x9 real symmetric matrix with the following coefficients,

$$\bar{R} = \sum_{i=1}^N \begin{bmatrix} x_i & y_i x_i & z_i x_i & y_i x_i & y_i z_i x_i & z_i x_i & x_i & y_i x_i & x_i \\ x_i y_i & y_i & z_i y_i & z_i y_i & x_i z_i y_i & x_i y_i z_i & x_i y_i & y_i & y_i \\ x_i z_i & y_i z_i & z_i & x_i y_i z_i & y_i z_i & x_i z_i & x_i z_i & y_i z_i & z_i \\ x_i y_i & y_i z_i & z_i x_i y_i & x_i y_i & x_i y_i z_i & x_i y_i z_i & x_i y_i & x_i y_i & x_i y_i \\ x_i y_i z_i & y_i z_i & y_i z_i & x_i y_i z_i & y_i z_i & x_i y_i z_i & x_i y_i z_i & y_i z_i & y_i z_i \\ x_i z_i & x_i y_i z_i & x_i z_i & x_i y_i z_i & x_i y_i z_i & x_i z_i & x_i z_i & x_i y_i z_i & x_i z_i \\ x_i & x_i y_i & x_i z_i & x_i y_i & x_i y_i z_i & x_i z_i & x_i & y_i z_i & x_i \\ x_i y_i & y_i & y_i z_i & x_i y_i & y_i z_i & x_i y_i z_i & x_i y_i & y_i & y_i \\ x_i & y_i & z_i & x_i y_i & y_i z_i & x_i z_i & x_i & y_i & 1 \end{bmatrix} \quad (3.9)$$

E is a column vector with the following elements,

$$E = \sum_{i=1}^N \begin{bmatrix} z_i x_i \\ z_i y_i \\ z_i \\ x_i y_i z_i \\ y_i z_i \\ x_i z_i \\ x_i z_i \\ y_i z_i \\ z_i \end{bmatrix} \quad (3.10)$$

and X column vector with the following elements,

$$X = \begin{bmatrix} a_1 \\ a_2 \\ a_3 \\ a_4 \\ a_5 \\ a_6 \\ a_7 \\ a_8 \\ a_{10} \end{bmatrix} \quad (3.11)$$

The solution to Eq. (3.8) provides the optimum coefficients for a best-fit paraboloid defined by Eq. (3.1) in the least square sense.

Differential geometry (Refs. 58 and 59) forms the basis for obtaining the translational and rotational relationship between the (x,y,z) coordinate system and the (x',y',z') coordinate system. In order to find the translation between both systems it is necessary to

find the vertex of the paraboloid defined by Eq. (3.1). Let's define the following variables,

$$P = a_3 \quad (3.12a)$$

$$Q = a_5 y + a_6 x + 1 \quad (3.12b)$$

$$R = a_1 x^2 + a_2 y^2 + a_4 xy + a_7 x + a_8 y + a_{10} \quad (3.12c)$$

and rewrite Eq. (3.1) as a function of the new variables P, Q and R.

This yield the following,

$$S(x,y,z) = Pz^2 + Qz + R \quad (3.13)$$

the roots of the Eq. (3.13) describes a generalized paraboloid in the form $z = f(x,y)$,

$$z = \frac{-Q - \sqrt{(Q^2 - 4PR)}}{2P} \quad (3.14)$$

the positive root is discarded because yields a solution in the negative z-direction. Differential geometry formulae can be used on Eq. (3.14) for obtaining the vertex of the paraboloid. The vertex is located at a point (x_0, y_0, z_0) at which the two principal curvatures have equal magnitudes. The principal curvatures of a surface of revolution are defined as follows:

$$K_1 = K_m + \sqrt{(K_m^2 - K_g)} \quad (3.15a)$$

$$K_2 = K_m - \sqrt{(K_m^2 - K_g)} \quad (3.15b)$$

where

$$K_m = \frac{Eg - 2fF + eG}{2(EG - F^2)} \quad (\text{mean curvature}) \quad (3.15c)$$

$$K_g = \frac{eg - f^2}{(EF - F^2)} \quad (\text{Gaussian curvature}) \quad (3.15d)$$

In Eq. (3.15c) to (d) the variables (e,g,f) and (E,G,F) are the first and the second fundamental coefficients associated with a surface of revolution. These coefficients are defined as follows,

$$E = 1 + f_x^2 \quad (3.16a)$$

$$F = f_x f_y \quad (3.16b)$$

$$G = 1 + f_y^2 \quad (3.16c)$$

$$e = \Delta f_{xx} \quad (3.16d)$$

$$f = \Delta f_{xy} \quad (3.16e)$$

$$g = \Delta f_{yy} \quad (3.16f)$$

$$\Delta = -\left(\sqrt{(1 + f_x^2 + f_y^2)}\right)^{-1} \quad (3.16g)$$

$$f_x = \frac{d f(x,y)}{d x} \quad (3.16h)$$

$$f_{xx} = \frac{d^2 f(x,y)}{d x^2} \quad (3.16i)$$

$$f_y = \frac{d f(x,y)}{d y} \quad (3.16j)$$

$$f_{yy} = \frac{d^2 f(x,y)}{d y^2} \quad (3.16k)$$

$$f_{xy} = \frac{d^2 f(x,y)}{d x d y} \quad (3.16l)$$

with these definitions, the required derivatives are obtained from Eq. (3.14) with following results,

$$f_x = -\frac{1}{2P} \frac{d Q}{d x} - \frac{1}{2P} \frac{d \sqrt{(Q^2 - 4PR)}}{dx} \quad (3.17a)$$

$$f_{xx} = -\frac{1}{2P} \frac{d^2 Q}{dx^2} - \frac{1}{2P} \frac{d^2 \sqrt{(Q^2 - 4PR)}}{dx^2} \quad (3.17b)$$

$$f_y = -\frac{1}{2P} \frac{dQ}{dy} - \frac{1}{2P} \frac{d\sqrt{(Q^2 - 4PR)}}{dy} \quad (3.17c)$$

$$f_{yy} = -\frac{1}{2P} \frac{d^2 Q}{dy^2} - \frac{1}{2P} \frac{d^2 \sqrt{(Q^2 - 4PR)}}{dy^2} \quad (3.17d)$$

$$f_{xy} = -\frac{1}{2P} \frac{d^2 Q}{dx dy} - \frac{1}{2P} \frac{d^2 \sqrt{(Q^2 - 4PR)}}{dx dy} \quad (3.17e)$$

where

$$\begin{aligned} (Q^2 - 4PR) = & x^2 (a_6^2 - 4 a_3 a_1) + y^2 (a_5^2 - 4 a_3 a_5) \\ & + xy (2 a_5 a_6 - 4 a_3 a_4) + x (2 a_6 a_9 - 4 a_3 a_7) \\ & + y (2 a_5 a_9 - 4 a_3 a_8) + (a_9^2 - 4 a_3 a_{10}) \end{aligned} \quad (3.18)$$

Using the following substitutions

$$m_1 = (a_6^2 - 4 a_3 a_1) \quad (3.19a)$$

$$m_2 = (a_5^2 - 4 a_3 a_2) \quad (3.19b)$$

$$m_3 = (2 a_5 a_6 - 4 a_3 a_4) \quad (3.19c)$$

$$m_4 = (2 a_6 a_9 - 4 a_3 a_7) \quad (3.19d)$$

$$m_5 = (2 a_5 a_9 - 4 a_3 a_8) \quad (3.19e)$$

$$m_6 = (a_9^2 - 4 a_3 a_{10}) \quad (3.19f)$$

the required derivatives in Eq. (3.17a) to (e) are obtained as follows,

$$T_x = \frac{d(Q^2 - 4PR)}{dx} = m_1 x + y m_3 + m_4 \quad (3.20a)$$

$$T_{xx} = \frac{d^2(Q^2 - 4PR)}{dx^2} = m_1 \quad (3.20b)$$

$$T_y = \frac{d^2(Q - 4PR)}{d y} = m_2 y + x m_3 + m_5 \quad (3.20c)$$

$$T_{yy} = \frac{d^2(Q^2 - 4PR)}{d y^2} = m_2 \quad (3.20d)$$

$$T_{xy} = \frac{d^2(Q^2 - 4PR)}{d x d y} = m_3 \quad (3.20e)$$

By letting $V = \sqrt{(Q^2 - 4PR)}$, one obtains the following result.

$$\frac{d V}{d x} = 0.5 V^{-1/2} T_x \quad (3.21a)$$

$$\frac{d^2 V}{d x^2} = 0.5 V^{-1/2} T_{xx} + -0.25 T_x^2 V^{-3/2} \quad (3.21b)$$

$$\frac{d V}{d y} = 0.5 V^{-1/2} T_y \quad (3.21c)$$

$$\frac{d^2 V}{d y^2} = 0.5 V^{-1/2} T_{yy} + -0.25 T_y^2 V^{-3/2} \quad (3.21d)$$

$$\frac{d^2 V}{d x d y} = 0.5 V^{-1/2} T_{xy} + -0.25 T_x T_y V^{-3/2} \quad (3.21e)$$

$$\frac{d Q}{d x} = a_6 \quad (3.21f)$$

$$\frac{d^2 Q}{d x^2} = 0 \quad (3.21g)$$

$$\frac{d Q}{d y} = a_5 \quad (3.21h)$$

$$\frac{d^2 Q}{d y^2} = 0 \quad (3.21i)$$

$$\frac{d^2 Q}{d x d y} = 0 \quad (3.21j)$$

Equations (3.21a) to (j) evaluates the set of derivatives required in Eq. (3.14) for calculating the vertex. The location of the vertex is

found numerically. Reflector surface points are searched for a unique point at which the two principal curvatures are equal ($K_1 = K_2$).

The rotational characteristics between the (x,y,z) coordinate system and (x',y',z') coordinate system can be obtained by first finding the inward unit normal at the vertex point. This will be the z' axis direction. The other two axes directions relative to the (x,y,z) coordinate system are found from the normal direction. The unit normal at the vertex is given by,

$$\hat{n} = \frac{f_x \hat{x} + f_y \hat{y} + f_z \hat{z}}{\sqrt{(f_x^2 + f_y^2 + f_z^2)}} = \hat{z}, \quad (3.22)$$

where f_x and f_y are defined in (3.16h) and 3.16j) respectively, and $f_z = \frac{d f(x,y,x)}{d z}$. The projection of this unit normal \hat{n} on the x - y plane is given by,

$$\hat{n}_{xy} = \frac{f_x \hat{x} + f_y \hat{y}}{\sqrt{(f_x^2 + f_y^2)}} \quad (3.23)$$

The Eulerian rotations can be calculated by using the following expressions,

$$\cos (G1) = \hat{n}_{xy} \cdot (-\hat{y}) \quad (3.24a)$$

$$\cos (G2) = \hat{n} \cdot \hat{z} \quad (3.24b)$$

$$G3 = 0$$

The surface points defined in the (x,y,z) coordinate system are transformed into the (x',y',z') coordinate system using the following matrix equation:

$$\begin{bmatrix} x'_i \\ y'_i \\ z'_i \end{bmatrix} = \begin{bmatrix} e_{11} & e_{12} & e_{13} \\ e_{21} & e_{22} & e_{23} \\ e_{31} & e_{32} & e_{33} \end{bmatrix} \begin{bmatrix} x_i - x_0 \\ y_i - y_0 \\ z_i - z_0 \end{bmatrix} \quad (i=1, N) \quad (3.25)$$

where

$$e_{11} = \cos \theta \quad (3.26a)$$

$$e_{12} = \sin \phi \quad (3.26b)$$

$$e_{13} = 0 \quad (3.26c)$$

$$e_{21} = -\cos \theta \sin \phi \quad (3.26d)$$

$$e_{22} = \cos \theta \cos \phi \quad (3.26e)$$

$$e_{23} = \sin \theta \quad (3.26f)$$

$$e_{31} = \sin \phi \sin \theta \quad (3.26g)$$

$$e_{32} = -\sin \theta \cos \phi \quad (3.26h)$$

$$e_{33} = \cos \theta \quad (3.26i)$$

With all reflector surface points transformed to the (x', y', z') coordinate system the best fit paraboloid of revolution have the desired form given by Eq. (3.2). The only parameter unknown in Eq. (3.2) is the constant FL.

Let's define the following least square index

$$I' = \sum_{i=1}^N (DS'(x'_i, y'_i, z'_i) - S'(x'_i, y'_i, z'_i))^2 \quad (3.27a)$$

where

$DS'(x', y', z')$ nth order surface polynomial representing the distorted reflector surface points.

$S'(x', y', z')$ paraboloid of revolution defined by Eq. (3.2)

substituting Eq. (3.2) into (3.27a) we obtain,

$$I' = \sum_{i=1}^N \left(\frac{(x'_i)^2 + (y'_i)^2}{FL} - z'_i \right)^2 \quad (3.27b)$$

Differentiating with respect to $1/FL$ one obtains,

$$\frac{d I'}{d 1/FL} = 0 \quad (3.28)$$

$$0 = \sum_{i=1}^N 2 \left[\frac{(x'_i)^2 + (y'_i)^2}{FL} - z'_i \right] \left((x'_i)^2 + (y'_i)^2 \right) \quad (3.29)$$

Solving for $1/FL$ yields

$$1/FL = \frac{\sum_{i=1}^N z'_i \left((x'_i)^2 + (y'_i)^2 \right)}{\sum_{i=1}^N \left((x'_i)^2 + (y'_i)^2 \right)} \quad (3.30)$$

Thus the equation for the paraboloid of revolution in the (x', y', z') coordinate system is given by

$$x'^2 + y'^2 = (1/FL)z' \quad (3.31)$$

3.4 Surface Error Component

The surface deviations of the distorted reflector surface points with respect to the best fit paraboloid is defined as the surface error component. The surface error component can be expressed as,

$$zz'_i = Dz'_i - z'_i, \quad i = 1, N \quad (3.32)$$

where

(x'_i, y'_i, Dz'_i) reflector surface points

$z'_i = \frac{x'^2_i + y'^2_i}{4F}$ best fit paraboloid

A two-dimensional continuous function like the one above and defined in the domain, $-K < x < K$ and $-L < y < L$ can be approximated by a two-dimensional Fourier series (Ref. 60).

$$\begin{aligned}
 f(x,y) = & \frac{a_{00}}{4} + \frac{1}{2} \sum_{n=1}^{\infty} \left(a_{0n} \cos\left(\frac{n\pi y}{L}\right) + b_{0n} \sin\left(\frac{n\pi y}{L}\right) \right) + \frac{1}{2} \sum_{n=1}^{\infty} \\
 & \times \left(a_{m0} \cos\left(\frac{m\pi x}{K}\right) + c_{m0} \sin\left(\frac{m\pi x}{K}\right) \right) + \sum_{n=1}^{\infty} \sum_{m=1}^{\infty} \left(a_{mn} \cos\left(\frac{m\pi x}{K}\right) \cos\left(\frac{n\pi y}{L}\right) \right. \\
 & \left. + b_{mn} \cos\left(\frac{m\pi x}{K}\right) \sin\left(\frac{n\pi y}{L}\right) + c_{mn} \sin\left(\frac{m\pi x}{K}\right) \cos\left(\frac{n\pi y}{L}\right) + d_{mn} \sin\left(\frac{m\pi x}{K}\right) \sin\left(\frac{n\pi y}{L}\right) \right)
 \end{aligned} \tag{3.33}$$

where the Fourier coefficients a_{mn}, b_{mn}, c_{mn} and d_{mn} are given by,

$$a_{mn} = \int_{-L}^L \int_{-K}^K f(x,y) \cos\left(\frac{m\pi x}{K}\right) \cos\left(\frac{n\pi y}{L}\right) dx dy \tag{3.34a}$$

$$b_{mn} = \int_{-L}^L \int_{-K}^K f(x,y) \cos\left(\frac{m\pi x}{K}\right) \sin\left(\frac{n\pi y}{L}\right) dx dy \tag{3.34b}$$

$$c_{mn} = \int_{-L}^L \int_{-K}^K f(x,y) \sin\left(\frac{m\pi x}{K}\right) \cos\left(\frac{n\pi y}{L}\right) dx dy \tag{3.34c}$$

$$d_{mn} = \int_{-L}^L \int_{-K}^K f(x,y) \sin\left(\frac{m\pi x}{K}\right) \sin\left(\frac{n\pi y}{L}\right) dx dy \tag{3.34d}$$

If the function $z = f(x,y)$ have the following symmetry conditions,

$$f(-x,y) = -f(x,y) \quad \text{and} \quad f(x,-y) = -f(x,y) \tag{3.35}$$

Then Eq. (3.33) can be simplified to,

$$f(x,y) = \sum_{m=1}^{\infty} \sum_{n=1}^{\infty} d_{mn} \sin\left(\frac{m\pi x}{K}\right) \sin\left(\frac{n\pi y}{L}\right) \tag{3.36}$$

a two-dimensional sinusoidal Fourier series.

In general the surface error component zz'_i is defined over a region $x_{\min} < x' < x_{\max}$ and $y_{\min} < y' < y_{\max}$ (Fig. 13). Equation (3.36) requires zz'_i to satisfy the symmetry conditions given by Eq. (3.35). A coordinate system (x'', y'', z'') is used for rearranging the reflector surface points in a format such that the symmetry conditions are satisfied. First the surface error points in Eq. (3.2) are translated to the first quadrant of the (x'', y'', z'') coordinate system. The other three quadrants are filled with data points corresponding to the symmetry conditions in Eq. (3.35). This process is illustrated in Fig. 14. The Fourier coefficients of the zz''_i surface error component can be obtained as follows,

$$d_{mn} = \frac{4}{K \cdot L} \Delta_x \Delta_y \sum_{i=1}^{M_x} \sum_{j=1}^{M_y} zz''_i(x''_i, y''_i) \sin\left(\frac{m\pi}{K} x''_i\right) \sin\left(\frac{n\pi}{L} y''_i\right) \quad (3.37)$$

where

$$M_x = \frac{L}{\Delta_x} + 1 \quad (3.38a)$$

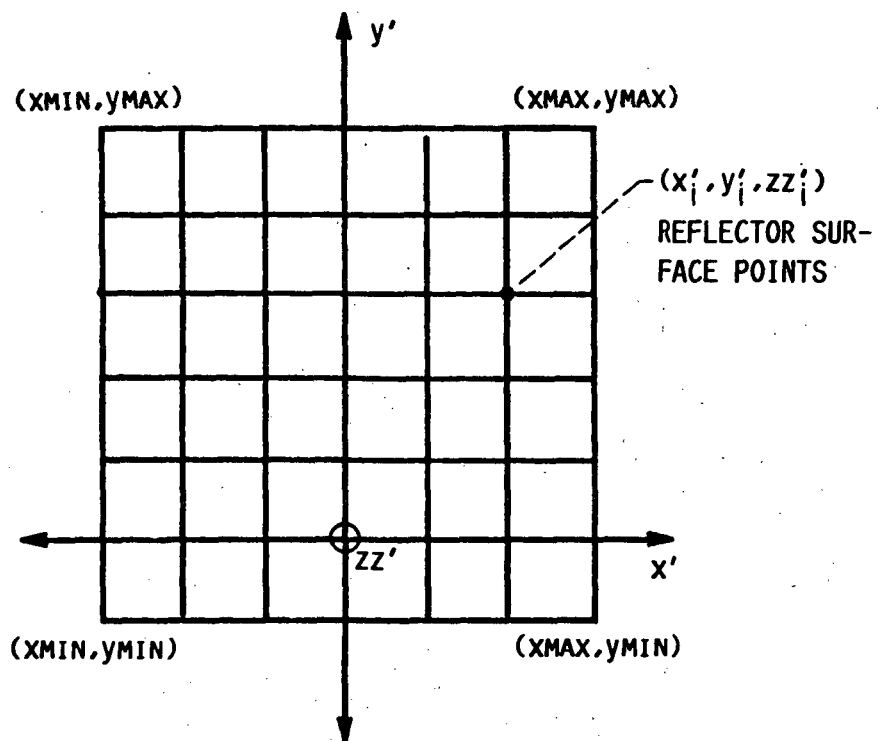
$$M_y = \frac{K}{\Delta_y} + 1 \quad (3.38b)$$

$$\Delta_x, \Delta_y \quad \text{sampling spacings in } x \text{ and } y \text{ dimensions respectively} \quad (3.38c)$$

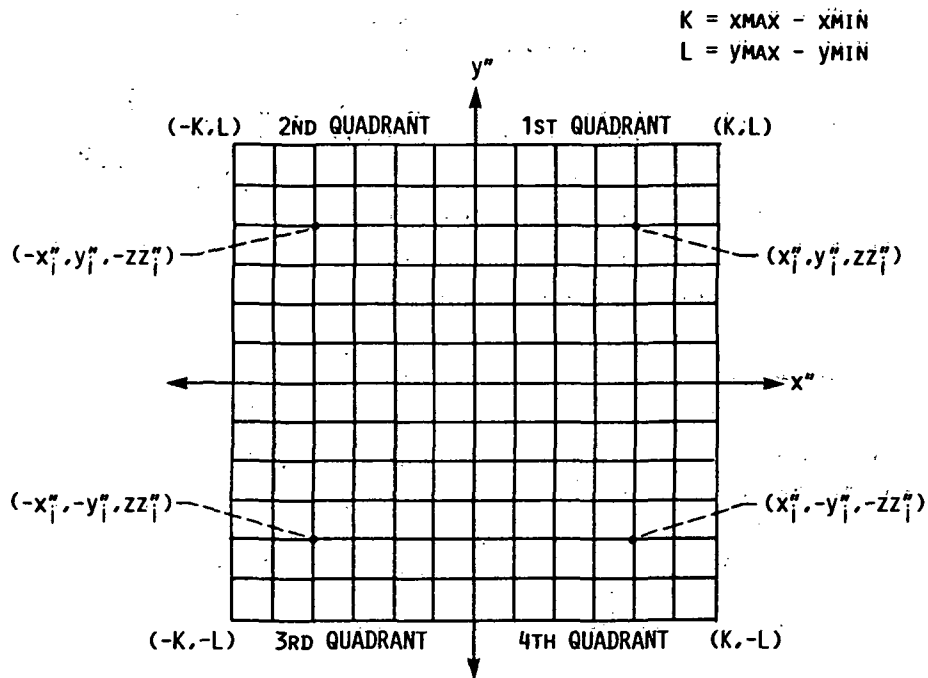
$$x''_i = x'_i - x_{\min} \text{ translation in } x \text{ dimension} \quad (3.38d)$$

$$y''_i = y'_i - y_{\min} \text{ translation in } y \text{ dimension} \quad (3.38e)$$

Let us define the Fourier matrix \bar{D} ,



13 Reflector surface points defined over a rectangular grid



14 Illustration of reflector data points augmentation and translation.

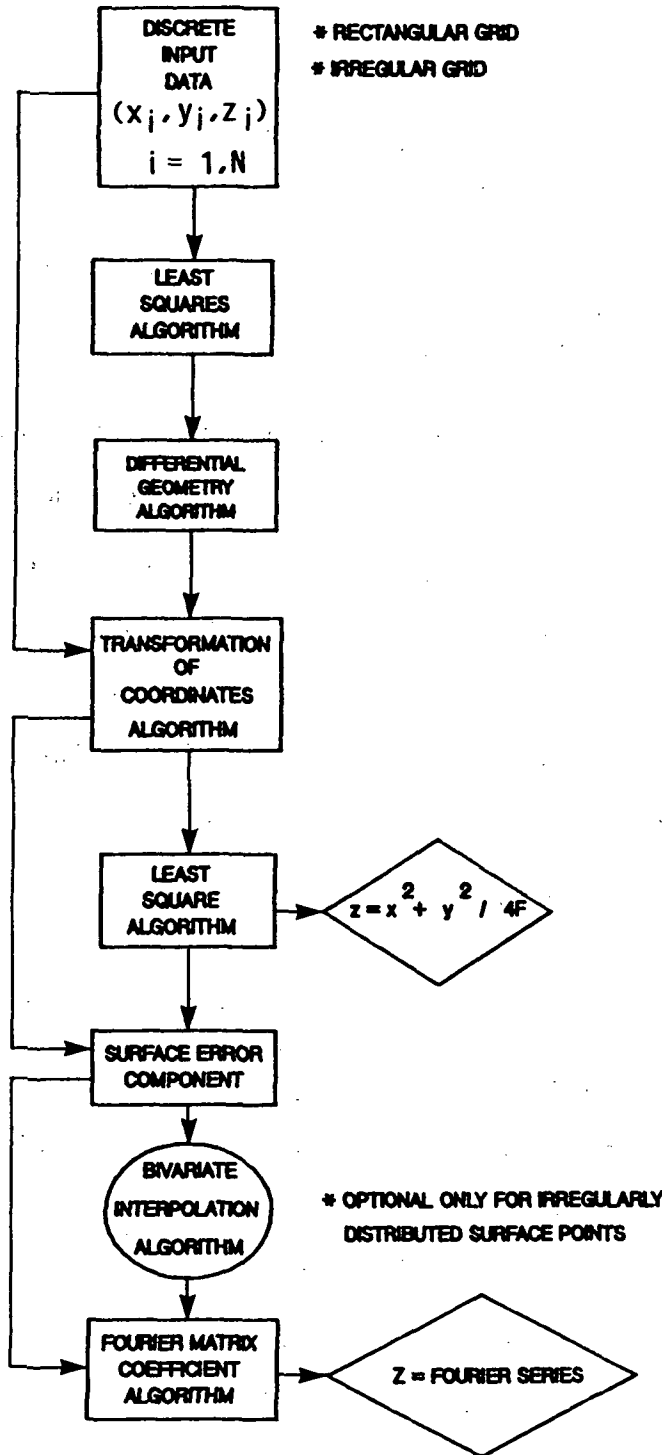
$$\bar{D} = \begin{bmatrix} d_{11} & d_{12} & d_{13} & \dots & d_{1n} \\ d_{21} & d_{22} & & \dots & d_{2n} \\ \dots & & & & \\ \dots & & & & \\ \dots & & & & \\ d_{n1} & \dots & \dots & \dots & d_{nn} \end{bmatrix} \quad (3.39)$$

Where d_{mn} are the Fourier coefficients defined by Eq. (3.37). The elements of the matrix \bar{D} defines the spatial spectra of the surface error for a given reflector antenna surface. The order n of this matrix is estimated by including only the coefficients with amplitude greater than $\lambda/200$ or it can be arbitrarily chosen. Another parameter of interest is the root mean square (RMS) value of the surface error component, which is defined as,

$$\text{RMS} = (d_{11}^2 + d_{12}^2 + \dots + d_{1n}^2 + d_{21}^2 + d_{22}^2 + \dots + d_{2n}^2 + \dots + d_{n1}^2 + d_{n2}^2 + \dots + d_{nn}^2)^{1/2} \quad (3.40)$$

3.5 Numerical Results and Discussion

Figure 15 represents a block diagram of a computer simulation of the above stated problem. The reflector surface points are usually obtained from a holographic, photogrametric or any other surface detection technique. The computer algorithm was tested with known distortion profiles and TRASYS-SYNDA-NASTRAN (Ref. 4) simulated thermal distortions superimposed into a reflector antenna geometry.



- 15 Computer implementation for obtaining an analytical representation for a reflector surface defined by a set of points

The distortion profiles considered for the simulation are described in Table 5 and the reflector geometry illustrated in Fig. 16. Case A in Table 5 describes a small ($\lambda/20$ or less) distortion profile and case B illustrates a large (of the order of several wavelengths) distortion profile. The frequency used for the simulation was 10 GHz. A set of equally spaced data points (100x100) were needed to generate the distorted reflector surface.

TABLE 5. - DISTORTION PROFILE PARAMETERS

	Fourier Coefficients (In wavelength)								
	d_{11}	d_{12}	d_{13}	d_{21}	d_{22}	d_{23}	d_{31}	d_{32}	d_{33}
Case A	+0.0500	+0.0700	-0.0300	+0.1500	-0.0040	+0.0900	-0.0033	-0.0083	-0.0310
Case B	+0.0300	+0.3000	-2.000	-3.000	+0.4000	+3.000	-1.000	+5.000	-0.3000

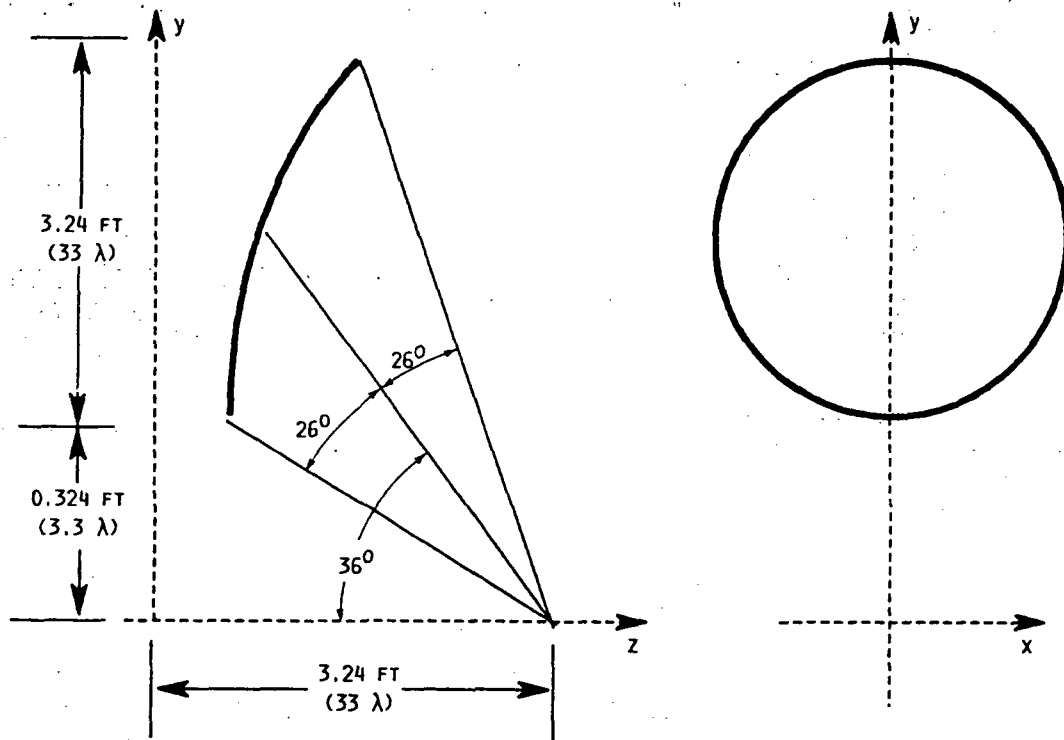
The estimated surface errors and best fit parabolic surface geometry are described in Table 6.

TABLE 6. - ESTIMATED DISTORTION PROFILE PARAMETERS

	Fourier Coefficients (In wavelength)								
	d_{11}	d_{12}	d_{13}	d_{21}	d_{22}	d_{23}	d_{31}	d_{32}	d_{33}
Case A	+0.0497	+0.0710	-0.0305	+0.1501	-0.0039	+0.0913	-0.0032	-0.0082	-0.0312
Case B	+0.0318	+0.2999	-1.998	-2.999	+0.4108	+2.988	-0.9999	+5.100	-0.2991

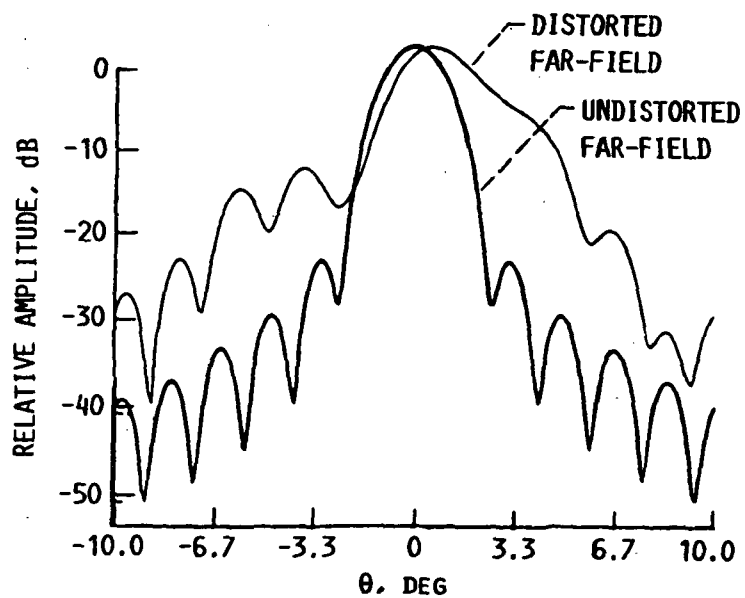
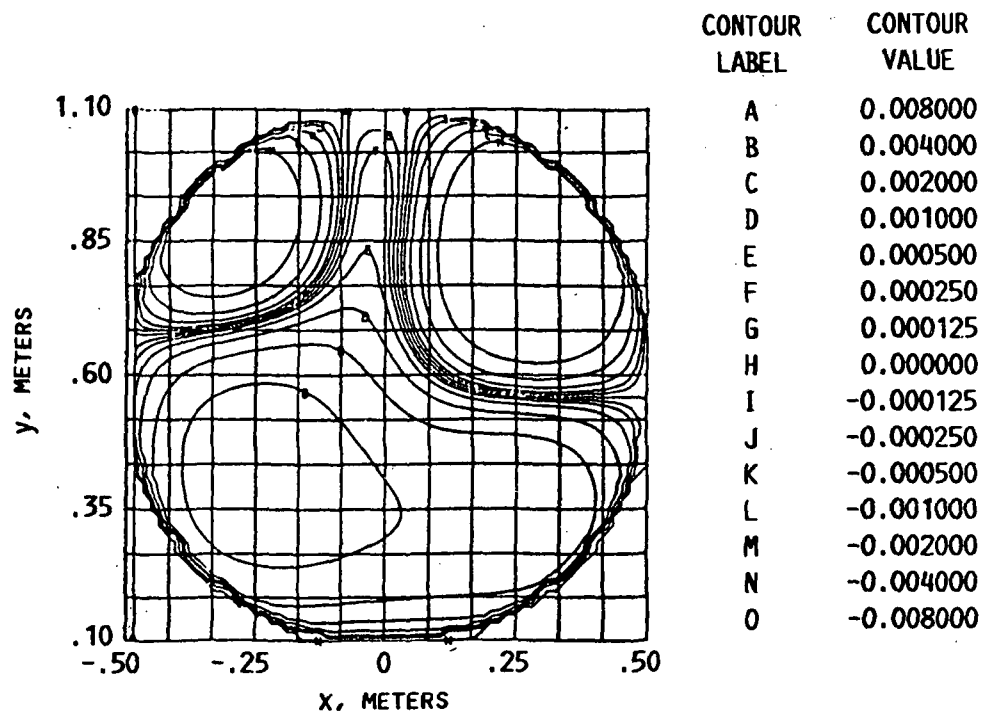
Estimated focal length:
Case A 3.290109 ft
Case B 3.313091 ft

Figures 17(a) and (b) show the estimated surface profile corresponding to case A and case B and their respective far field radiation patterns. The results presented in Table 6 are in good agreements with the input distortion by Fourier coefficients on



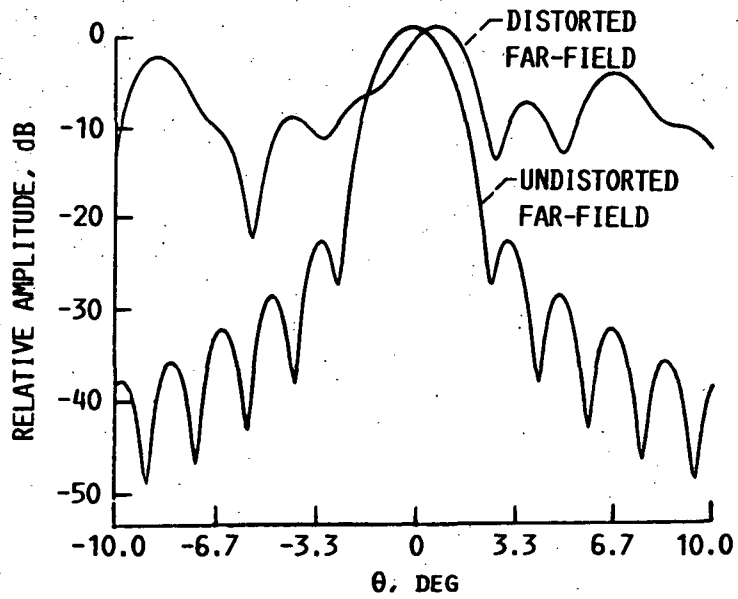
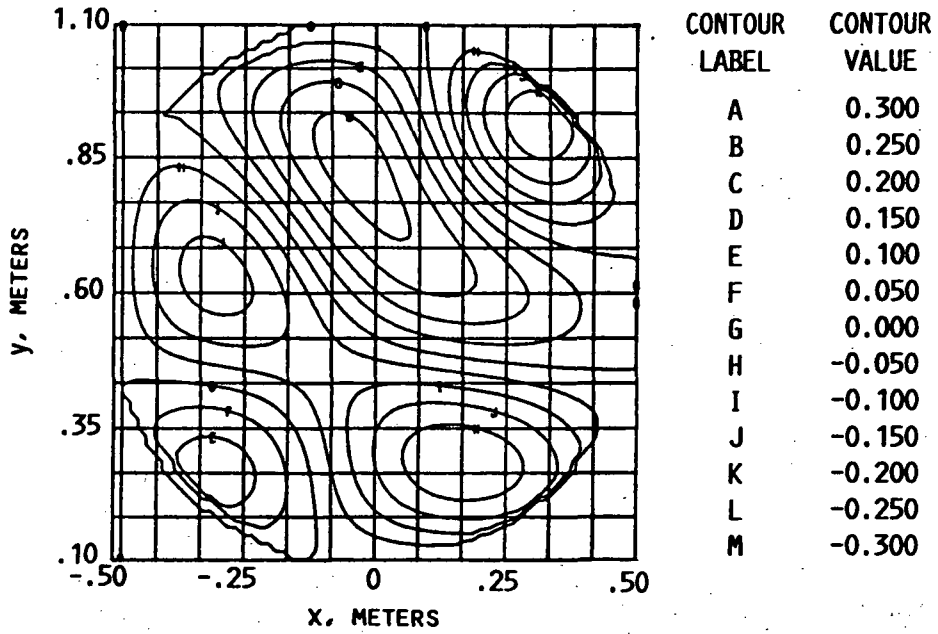
16 Offset parabolic reflector geometry

ORIGINAL PAGE IS
OF POOR QUALITY



(a) Case A (small distortion profile).

17 E-plane radiation pattern and their estimated distortion profile

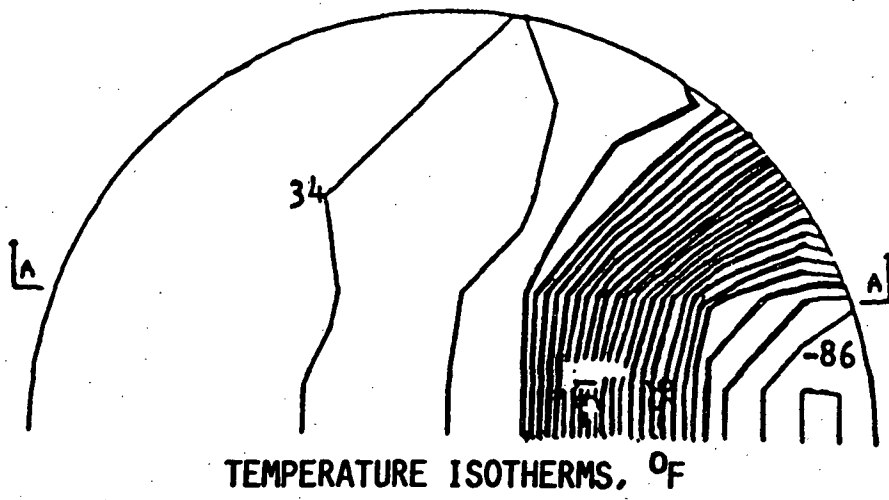


(b) Case B (large distortion profile).

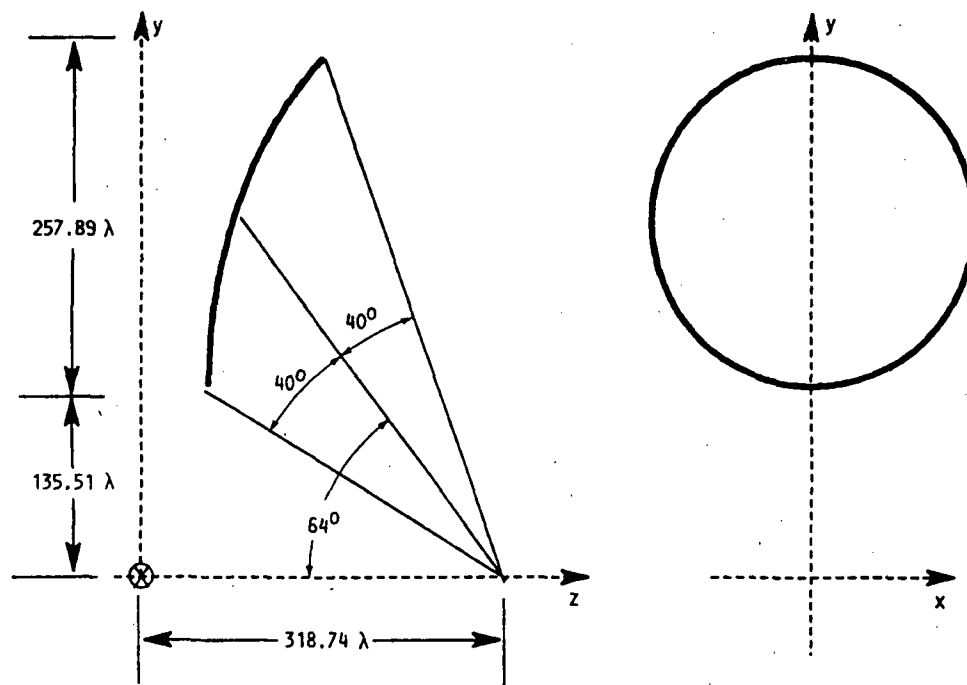
Fig. 7. - Concl.

Table 5. It was found that the Fourier matrix had higher order coefficients with non zero values but they were one order of magnitude less than the lowest amplitude of the Fourier coefficient presented on Table 6.

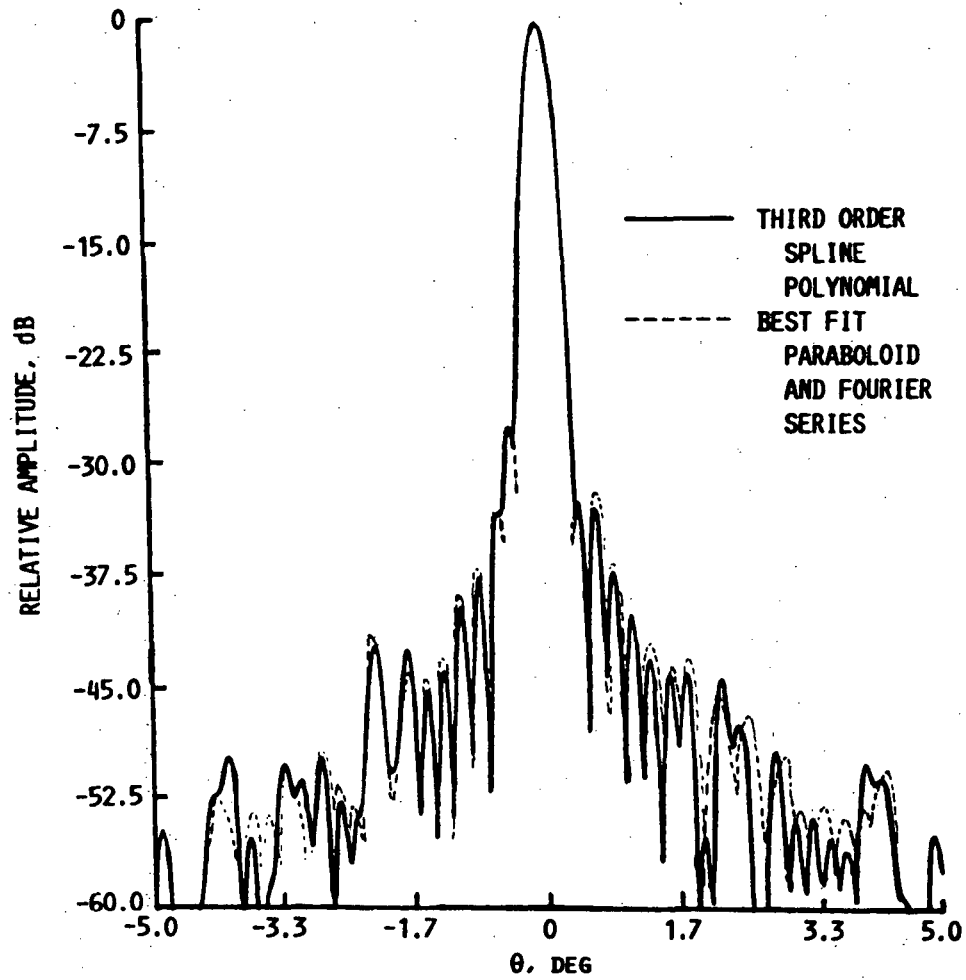
The technique was compared with results obtained by using a spline polynomial technique for approximating the distorted reflector surface points (Ref. 4). In this case the distorted reflector surface points were obtained by simulating thermal deformation with a TRASYS-SINDA-NASTRAN computer programs. In brief, TRASYS and SINDA are used to characterize the on-orbit thermal environment, NASTRAN calculates the thermally induced mechanical distortions. Figure 18 shows the temperature distribution on the reflector antenna surface for the case under consideration. The reflector geometry input to the thermal programs is presented in Fig. 19. The frequency considered was 28.75 GHz and a 100x100 surface points were used for the analysis. The far field radiation pattern corresponding to the thermal simulation case is presented in Fig. 20. The continuous line pattern corresponds to the polynomial spline algorithm (Ref. 4) and the dotted line pattern corresponds to the best fit paraboloid and Fourier series expansion approximation. There is no major differences between beam direction or sidelobe levels, indicating a good agreement between the two techniques. The best fit paraboloid and Fourier series algorithm was very slow, about 3 hr of c.p.u. time in an IBM 370 computer. The spline polynomial algorithm takes about 1/2 hr on CRAY xmp computer. The long computation can be justified as a trade off to



18 Temperature distribution on the reflector surface



19 Offset parabolic reflector geometry



20 E-plane radiation pattern

obtain vital information about the distorted surface characteristics. These are the amplitude spectra of the surface error, the distorted surface profile, the RMS value and largest deviation on the reflector antenna surface. These are not directly available by any of the other existing techniques.

3.6 Concluding Remarks

One advantage of the developed technique is that it can be easily implemented in any existing reflector antenna secondary pattern computational methods. It can easily be extended to nonparabolic reflectors surfaces (spherical, planar, hyperbolic, elliptical, etc) by modifying the least square polynomial approximation. In applications involving the fabrication and design of precision reflector antennas the technique can be used as a computer aided tool. Information such as the average focal length, a root mean square of the surface error (RMS), surface error profile and the amplitude spectra for the reflector antenna under consideration are easily accessible from the algorithm. One draw back of the algorithm is that it is slow. This can be improved by using faster computer such as a CRAY and optimizing the computer codes for faster computing time.

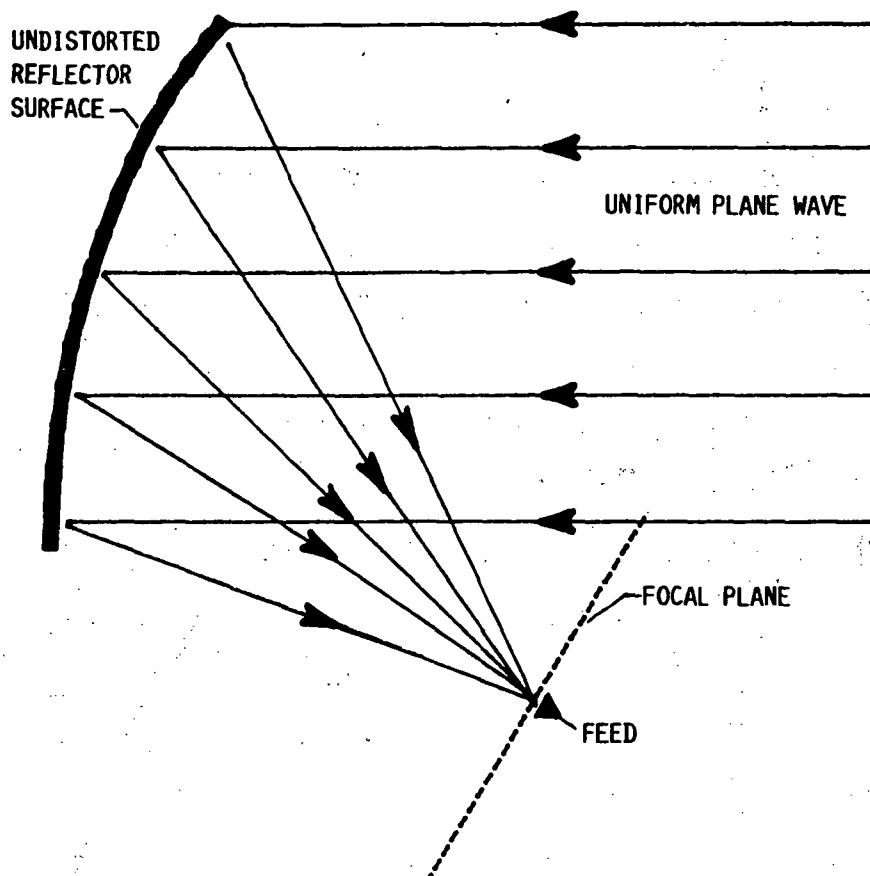
CHAPTER 4

COMPENSATION METHOD I: TRANSMITTING APPROACH

4.1 Introduction

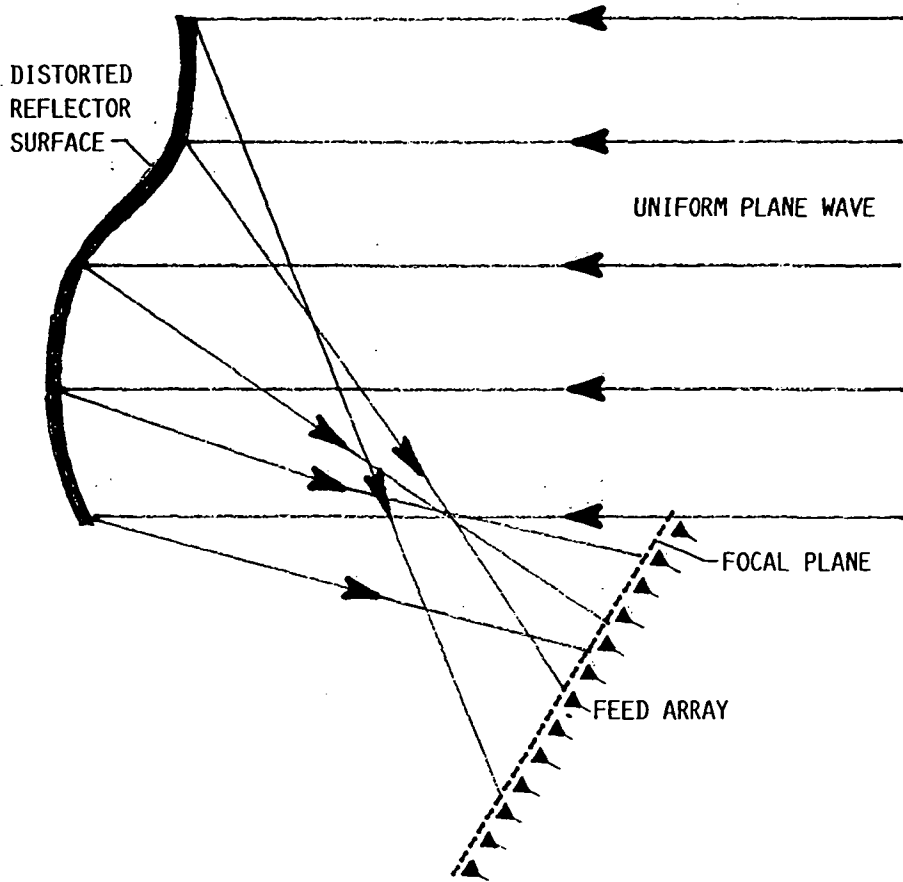
The performance characteristics (gain, sidelobe level, etc.) of space communication reflector antenna systems degrades as the reflector surface distorts due mainly to thermal (Ref. 4) effects caused by solar radiation. The compensating technique described here will maintain the desired boresight directivity (antenna performance) independently of thermal effects on the reflector surface. A feed array can be designed to compensate for thermally induced surface distortions.

For a better understanding of reflector surface error compensation, it is convenient to think of the antenna in the receiving mode. Figure 21(a) shows a uniform plane wave incident on a perfect parabolic reflector. In the geometrical optics sense, all rays will converge to a single point at the focus of the parabola, where they can be collected by a single feed element. Figure 21(b) shows a uniform plane wave incident on a distorted parabolic reflector. In this case, the rays will not converge to a single point, but will spread over the focal plane. Reflector surface error compensation will be achieved, if a feed array can capture all the energy spread over the focal plane and sum it constructively in the feed network. Improvement in the antenna performance due to compensation in the receive mode will



(a) Rays converging at focus of an undistorted parabolic reflector surface.

21 Plane wave incident on a reflector antenna



(b) Rays spread over the focal plane of a distorted reflector surface.

Fig. 21. - Concl.

produce improvement in the antenna performance in the transmitting mode by reciprocity.

The concept of conjugate field match (CFM) is utilized to determine the complex excitation coefficients of the feed array. Specifically the compensating feed array excitation coefficients are determined from the complex conjugate of the focal plane electric field (Ref. 33) distribution due to a uniform plane wave incident on the distorted reflector surface from the desired beam direction. In the transmitting approach (Ref. 61) the focal plane electric field distribution is determined by computing the far zone electric field in the desired beam direction due to a dipole source at a specified location in the focal plane. This computation procedure is performed for all specified feed array element locations in the focal plane and their conjugate values are used as the compensating feed array excitations.

4.2 Determination Of The Compensating Feed Array Geometry

It is assumed that the distorted reflector surface (usually described by a discrete set of points) is known a priori. The distorted reflector surface points can be approximated with two analytical surface components (see chapter 3): an undistorted surface component and a surface error component. The undistorted surface component is mathematically expressed with a best fit paraboloid polynomial and the surface error component is described as a sinusoidal Fourier series expansion of the residual. The surface error component with the largest spatial frequency and amplitude product

determines the feed array area required (Ref. 62) to capture all the energy spread in the focal plane (Fig. 21(b)).

The geometry of the best fit paraboloid (undistorted surface component) is illustrated in Fig. 22. This geometry is completely specified by the following angles:

θ_{off} : off-set angle of the reflector

θ_{max} : half-angular extent of the reflector surface

The minimum area consisting of D by D (Fig. 22) in the focal plane needed for capturing about 80 percent of the energy spread (Ref. 62) is approximately given by

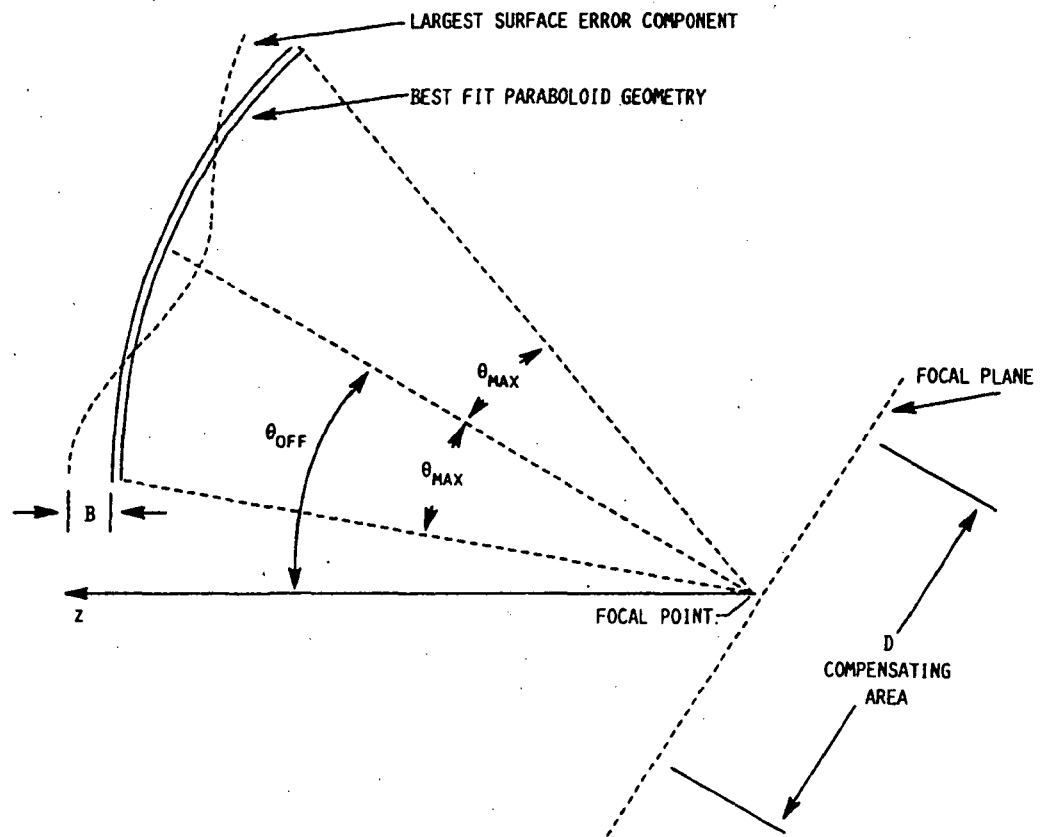
$$D = \frac{e\pi T B}{\sin \theta_{\text{max}}} (1 + \cos \theta_{\text{off}}) \quad (4.1)$$

where $e = 2.71828\dots$,

B : amplitude of the largest surface error component

T : number of periods of the largest surface error component over the extent of the reflector surface.

The required number of elements that can fit into the compensating area D (Eq. (4.1)) varies according to the desired array configuration and on the element aperture area. Typically horns, microstrips and dipole antennas are considered as radiating elements in either a hexagonal or rectangular array geometries. The gain and sidelobe level requirements of the subject reflector antenna will usually determine the number of radiating elements on the feed array (Refs. 63 and 64). A rule of thumb criteria for the element spacing for a given feed array configuration is to have minimum spacing in



22 Best fit parabolic geometry

order to reduce the spillover when illuminating the reflector. This is a good criteria for cases in which the feed array is located in the near field zone of the distorted reflector. For cases in which the feed array is located in the far field zone, the spacing should be determined such that there are no grating lobes generated within the reflector surface.

4.3 Computation of the Compensating Feed Array Excitation Coefficients

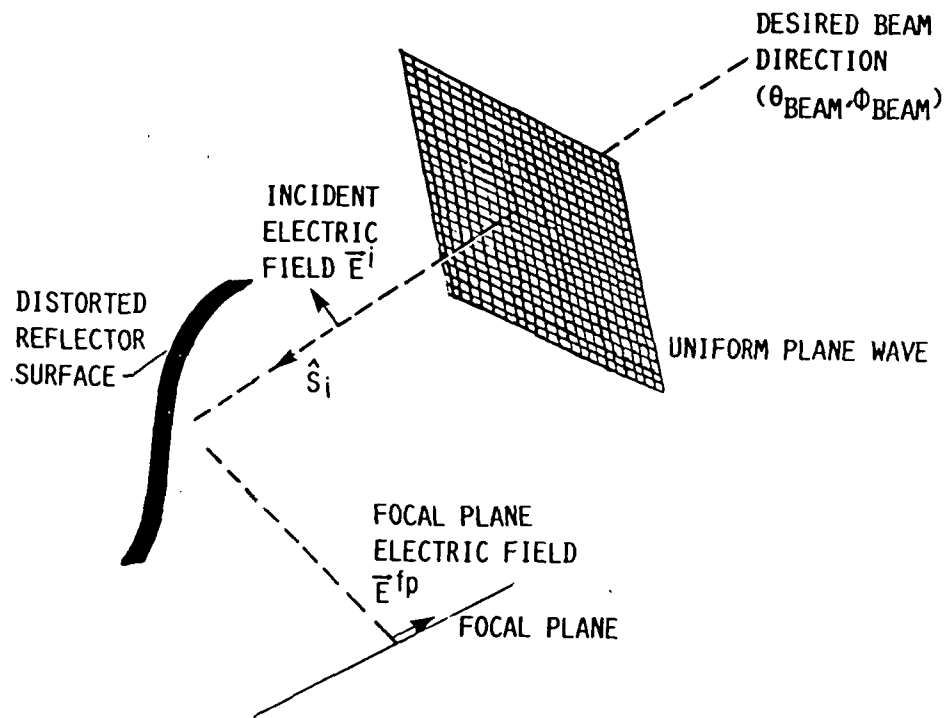
The focal plane electric field distribution contains the necessary information for finding the required number of elements, their best location and their proper complex excitations. Conceptually this field distribution results from an incident uniform plane wave impinging (Fig. 23) on the distorted reflector surface from the desired beam direction. The complex element excitation are obtained by taking the complex conjugate of the focal plane electric field distribution. This concept is known as conjugate field matching principle (CFM).

Let's assume that the feed array contains N elements located in the focal plane. The complex excitation coefficients, represented by a column vector I ,

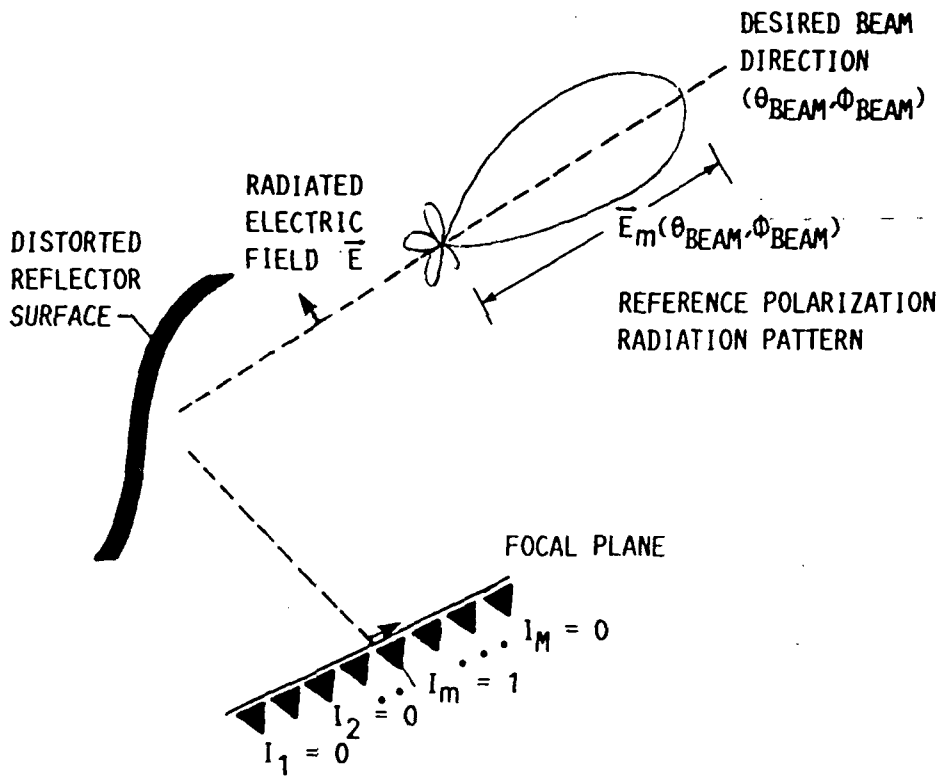
$$I = [I_1, I_2, I_3, \dots, I_N]^T \quad (4.2)$$

are to be determined.

Let us first calculate the far field radiation pattern of the distorted reflector antenna due to the m th element in the feed array (Fig. 24), namely due to the following array excitations,



23 Uniform plane wave illuminating the distorted reflector antenna



24 Reference polarization radiation pattern due to a radiating element located in the focal plane

$$I_m = 1, \quad \text{and all other } I_i = 0 \quad (4.3)$$

The corresponding far zone electric field can be written as,

$$\vec{E}_m(\vec{r}) = \frac{e^{-jKr}}{r} (\hat{R}E_m(\theta, \phi) + \hat{C}F_m(\theta, \phi)) \quad (4.4)$$

where $(r = \infty, \theta = \theta_{\text{BEAM}}, \phi = \phi_{\text{BEAM}})$ is the spherical coordinate of the desired observation point in the far field zone, (\hat{R}, \hat{C}) are unitary complex vectors describing the reference and the cross polarization of the reflector antenna (Ref. 46) respectively.

Let the column vector,

$$\vec{E}(\theta_{\text{BEAM}}, \phi_{\text{BEAM}}) = (E_1, E_2, E_3, \dots, E_N)^T \quad (4.5)$$

represent the reference polarization electric field in the observation direction $(\theta_{\text{BEAM}}, \phi_{\text{BEAM}})$ due to each of the individual elements in the feed array. The far fields in Eq. (4.5) can be easily obtained by using either a physical optics or an aperture integration technique (see chapter 2). Typically the physical optics method is chosen due to its computational ease. This method requires that the induced current distribution on the distorted reflector surface be integrated in order to obtain the radiated electric field at the desired observation direction $(\theta_{\text{BEAM}}, \phi_{\text{BEAM}})$.

Appendix D shows that by applying Lorentz reciprocity principle (Ref. 9) the focal plane electric field distribution of a distorted reflector antenna can be indirectly obtained from the transmitting electric fields due to dipole sources located in the focal plane (Refs. 61 and 62). In the receiving solution the focal plane

electric field distribution is directly obtained by integrating the induced current distribution due to an incident uniform plane wave on the distorted reflector.

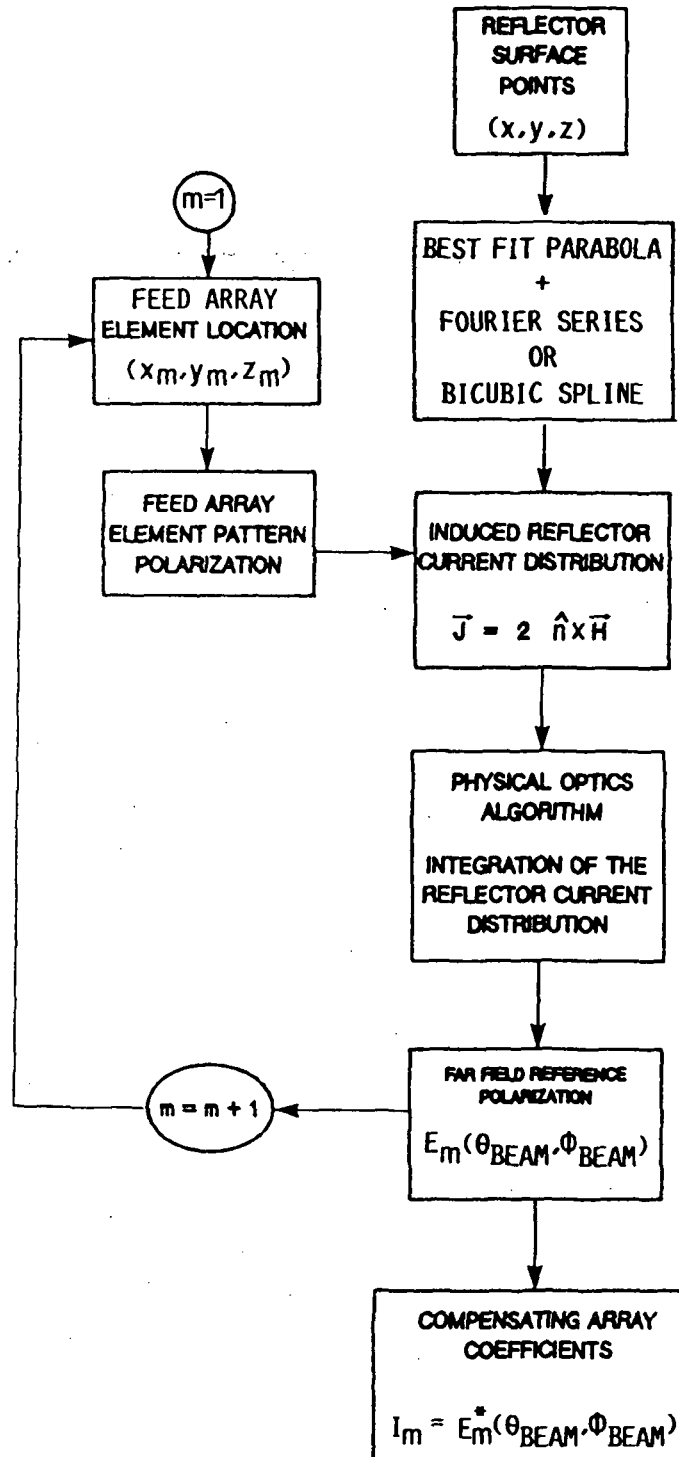
In the transmitting approach, the compensating feed array excitation coefficients are determined by using the reciprocity principle. The resulting complex excitation coefficients are given by Eq. (4.6).

$$I = E^*(\theta_{\text{BEAM}}, \phi_{\text{BEAM}}) \quad (4.6)$$

where $(\theta_{\text{BEAM}}, \phi_{\text{BEAM}})$ is the desired beam direction. This approach for determining the compensating array excitation coefficients is called indirect conjugate field matching (ICFM). This method has been widely used for more than 10 years (Refs. 11, 33 and 66 to 77) for applications requiring compensation of degraded antenna performance due to off-focus feeds.

4.4 Numerical Results and Discussion

A block diagram of a numerical implementation for the transmitting approach for calculating the compensating feed array excitations is presented in Fig. 25. Notice that for each of the feed element location (x_m, y_m, z_m) in the focal plane a far zone electric field is computed (Eq. (4.4)) in the desired beam direction $(\theta_{\text{BEAM}}, \phi_{\text{BEAM}})$ by using a physical optics algorithm.

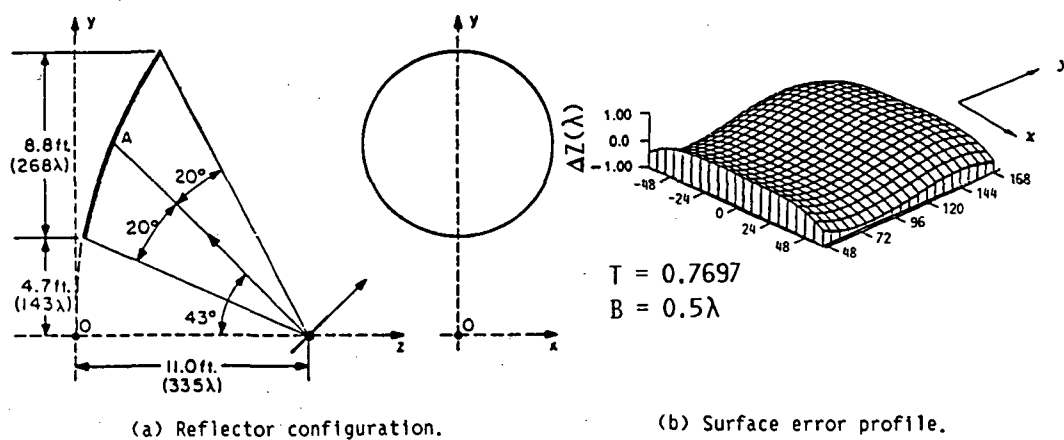


25 A computer implementation of the ICFM

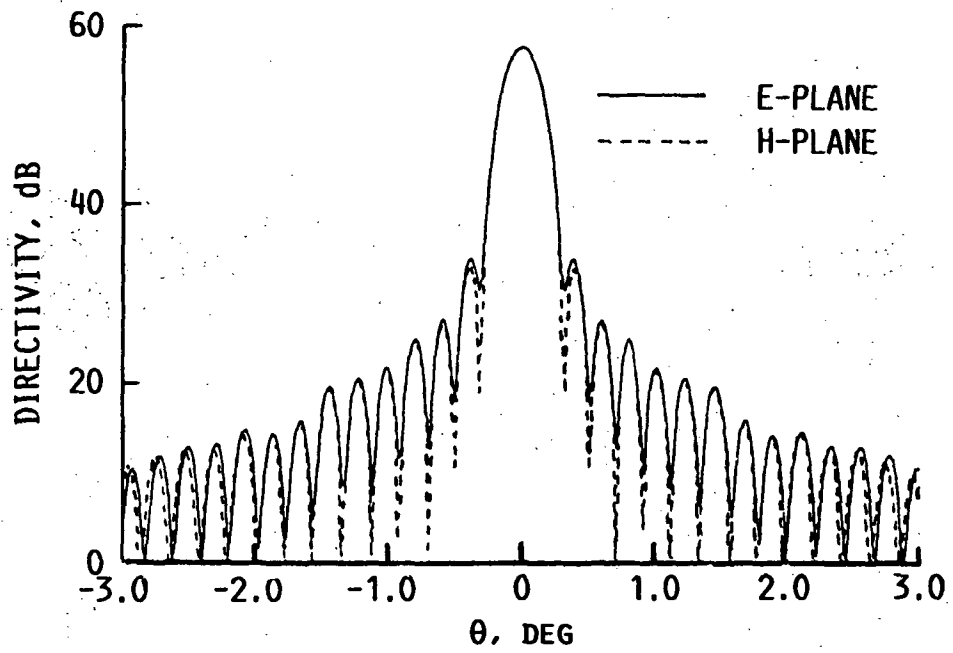
As an example of a surface error compensation using a feed array, consider the undistorted reflector and a given surface error profile presented in Figs. 26(a) and (b) respectively. The operating frequency is 30 GHz and the feed element type are considered to be square horns with a $(1.6\lambda \times 1.6\lambda)$ aperture dimension. The undistorted E and H-plane far field reflector antenna patterns with the single feed horn located at the focal point are shown in Fig. 27. The undistorted antenna boresight directivity is 58 dB. With the given surface error profile (Fig. 26(b)) superimposed on the undistorted reflector geometry (Fig. 26(a)) the resulting E and H-plane far field reflector antenna patterns with a single feed horn located on the focal point are shown in Fig. 28. The antenna boresight directivity is seen to be reduced to 38 dB (20 dB loss). It is required to compensate for the loss in directivity due to the surface distortions with a feed array. The first step is to design a compensating array configuration that will capture most of the energy spread in the focal plane. By applying Eq. (4.1) to the reflector geometry and considering the distortion profile shown in Figs. 26(a) and (b), we obtain the following compensating area,

$$D = \frac{(e)(\pi)(0.7697)(0.5)\lambda}{\sin(20^\circ)} (1 + \cos(43^\circ)) = 17.3\lambda$$

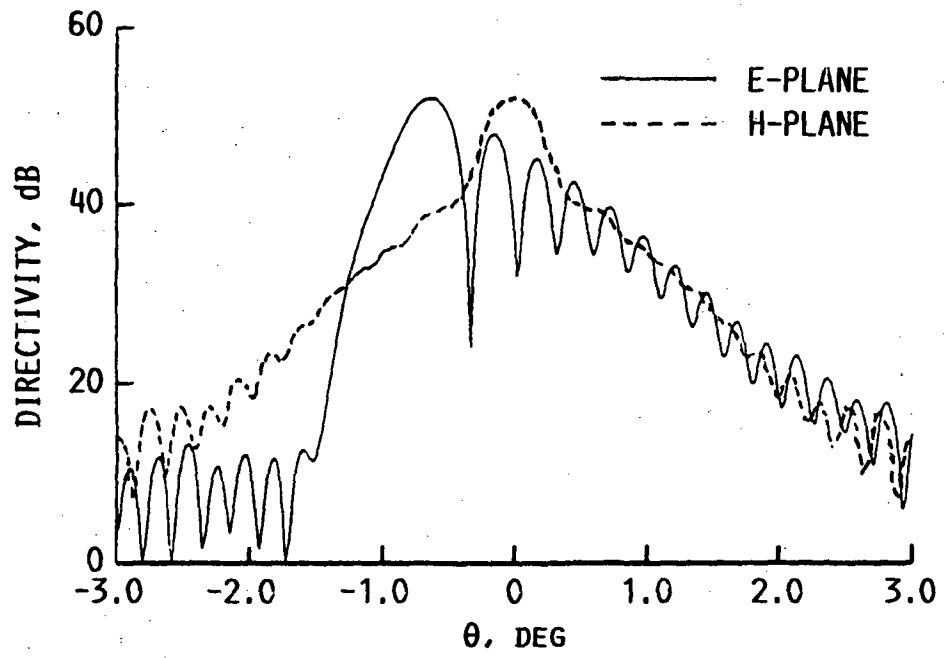
The radiating elements are square horns with a $(1.6\lambda \times 1.6\lambda)$ aperture dimension. The number of elements necessary for a rectangular array geometry are estimated to be 121 elements (a 11×11 array) at about 1.6λ spacing. The corresponding compensated E and H-plane reflector antenna pattern are shown in Fig. 29. The compensated



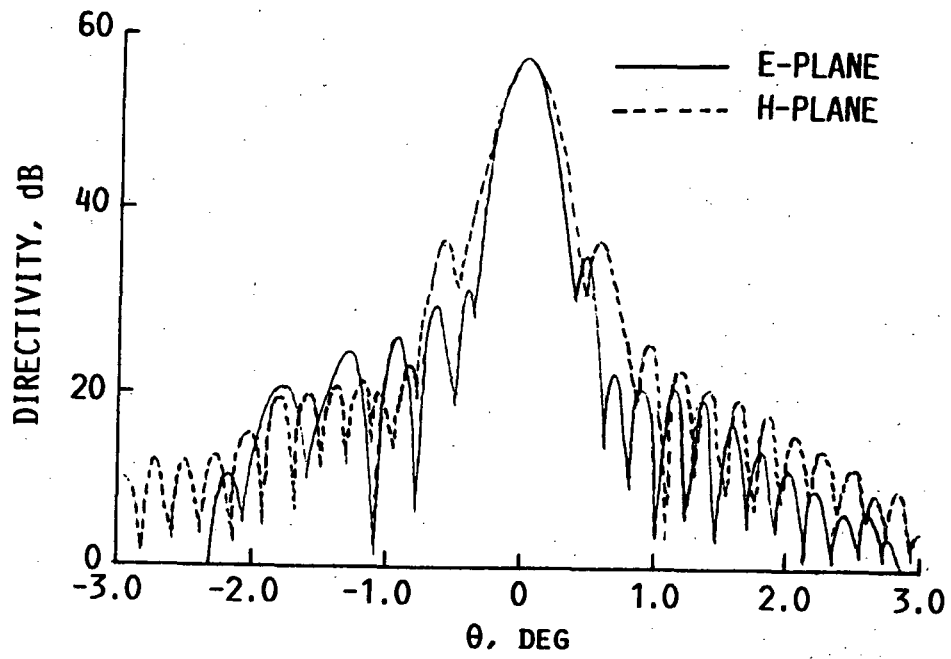
26 Distorted offset reflector antenna geometry



27 Undistorted reflector antenna radiation pattern



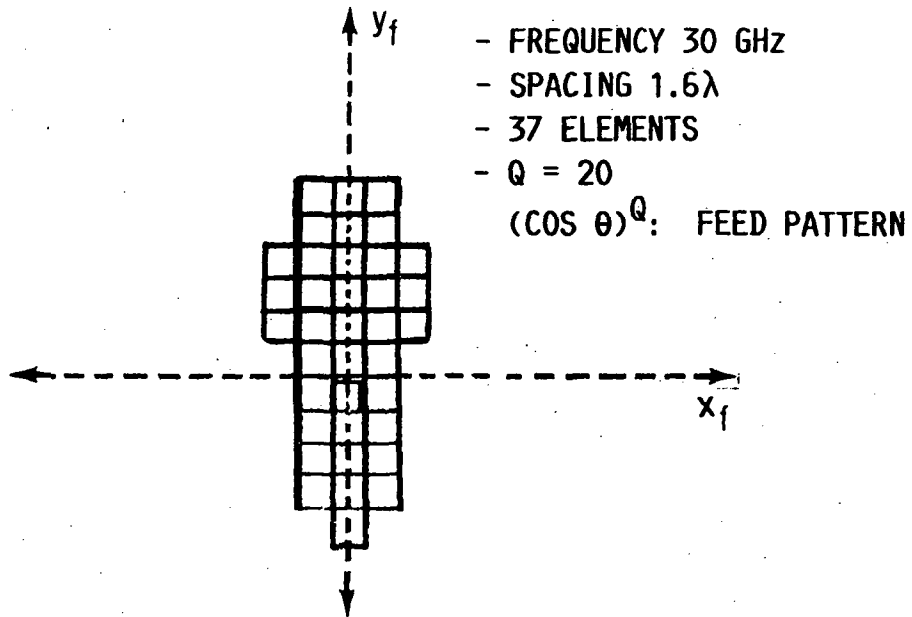
28 Distorted reflector antenna radiation pattern



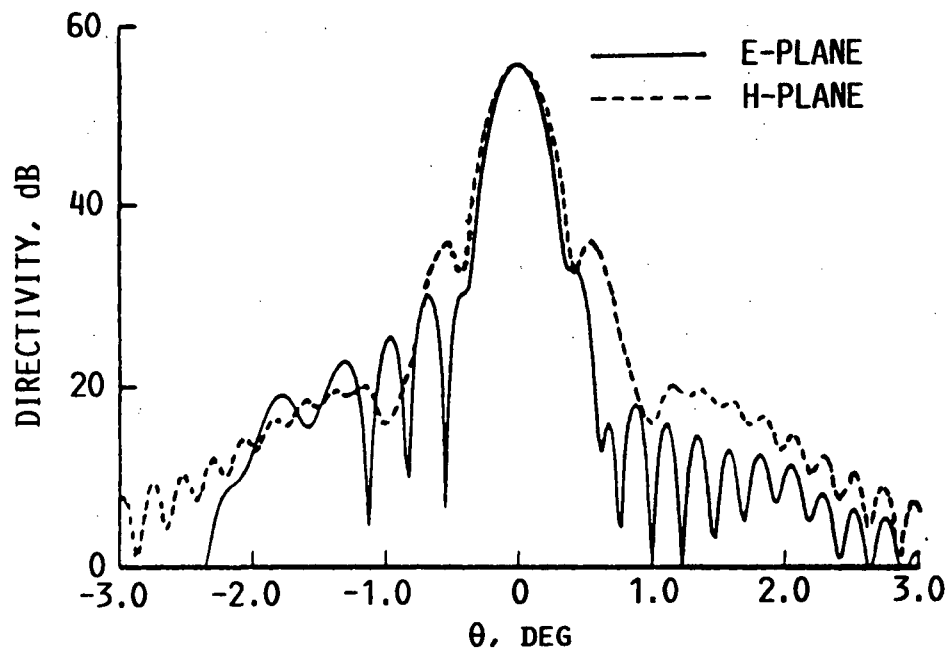
29 Compensated reflector antenna radiation pattern (11 x 11 rectangular feed array)

boresight directivity is within 0.969 dB of the undistorted boresight directivity; clearly showing a good design for the feed array size and element excitation coefficients. For comparison purposes let us consider another feed array geometry shown in Fig. 30. Note that the majority of the array elements are located along the vertical dimension of the array and very few elements are allocated horizontally. This feed array design has been made by taking advantage of the a priori knowledge of the distortion profile. Since there is no distortion variation in the horizontal dimension of the reflector it is expected that elements located horizontally in the feed array will contribute very little to performance compensation. The corresponding compensated E and H-plane antenna patterns are shown in Fig. 31. The compensated directivity for this case is within 1.7 dB of the undistorted boresight directivity. No major differences in the compensated E or H-plane pattern shape or boresight directivity is observed when compared to those obtained by using a 11×11 rectangular array configuration. The reason for this results is due mainly to the one-dimensional variation of the surface error profile (Fig. 26(b)). Therefore the excess of radiating elements in the 11×11 array distributed horizontally in the feed array did not add any extra compensation to the antenna pattern shape and directivity.

In general the surface error profiles due to thermal effects are estimated to have two dimensional variations (Ref. 4). This implies a large number of radiating elements to be required for a rectangular feed array configuration. Consequently the distortion



30 37 element feed array geometry



31 Compensated reflector antenna radiation pattern (37 element feed array)

error profile is a factor that needs to be taken into consideration when designing the compensating array. This technique clearly shows an improvement to the degraded reflector antenna directivity. The only draw back is lack of sidelobe control in the compensated antenna performance. For applications involving space reflector antenna where the main concern lies in maintaining the boresight directivity independently of thermal effect the transmitting approach certainly lend itself to an adaptive implementation.

CHAPTER 5

COMPENSATING METHOD II: RECEIVING APPROACH

5.1 Introduction

Array-fed reflector configurations are very desirable for space communication multiple and contour beam antenna systems. The radiation performance of these reflector antennas is degraded because of surface distortions induced by thermal effects from solar radiation. Distortions caused by thermal gradients are inherently a large scale phenomenon. By using computer programs such as TRASYS-SYNDA and NASTRAN (Ref. 4) to simulate thermal distortions, antenna performance degradations can be calculated. For example, boresight directivity loss of 3 to 8 dB, sidelobe level increase of 10 dB, and pointing loss of 0.1° to 2° , have been predicted by TRASYS-SYNDA and NASTRAN simulation. The chapter describes a technique to compensate such a degradation, so that the antenna performance is virtually independent of thermal effects on the reflector surface.

The compensating technique is briefly outlined below. Normally in a multiple beam antenna system, each beam is excited by a single element in the feed array (one-to-one excitation) such an excitation is not good enough if the reflector surface distortion is present. In the latter case, we will use a cluster of N elements (7 to 35 or even more feeds) to excite a single beam (N -to-one excitation). By adjusting the complex excitation coefficients of the cluster feed, the antenna

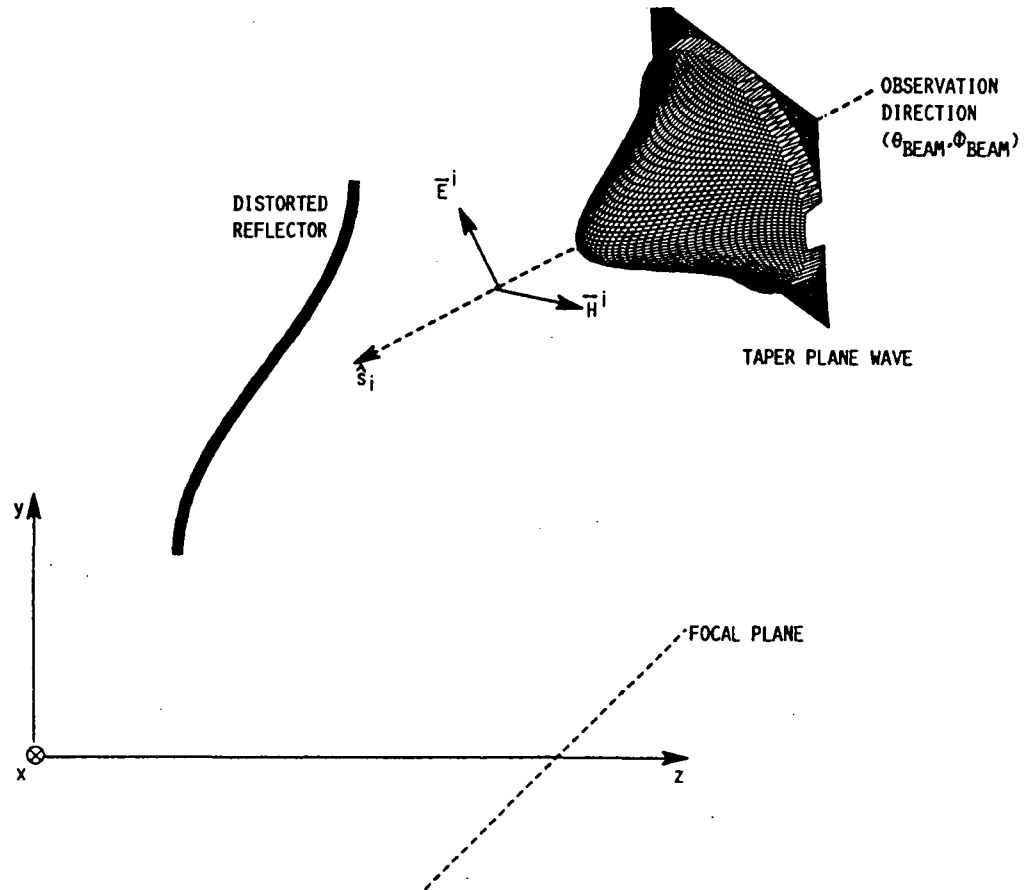
degradation due to reflector surface distortion can be partially restored. The degree of restoration depends on the number of feeds in the cluster, and the precision of realizing the desired excitation.

Obviously, the N-to-one excitation scheme is more complex than the conventional one-to-one scheme. The former requires both the excitation amplitude and phase control of all elements in the feed array. With the advent of monolithic microwave integrated circuits (MMIC), such a control becomes realizable without excessive effort (Ref. 78). It should be mentioned that in addition to electromagnetic compensation techniques studied here, other efforts have been carried out to reduce the impact of thermal distortion. Most of them are of mechanical nature (Refs. 79 and 80).

5.2 Problem Description

Given the desired boresight directivity, far field sidelobe envelope and distorted reflector surface points (x,y,z) , the compensation problem is to determine the minimum number of feed array elements, their best location and their excitations that will give rise to the desired antenna performance despite of the surface distortion.

The approach here is based on the receiving antenna mode, as outlined below. Let the distorted antenna be illuminated by an incident "plane wave" from a prescribed direction and with a prescribed polarization. That direction and polarization are those of the main beam when the antenna is in a transmitting mode. The "plane wave" has a planar phase front as in the ordinary plane wave case, but with a tapered amplitude, in contrast to the constant amplitude in the ordinary plane wave case (Fig. 32).



32 Distorted reflector antenna being illuminated by a tapered plane wave

Using this concept, the resulting fields in the focal plane of the reflector antenna can be calculated by integrating the induced current distribution on the distorted reflector surface. The focal plane electric field distribution contains the necessary information for determining the required number of feed array elements, their best location and complex excitations necessary to compensate for the surface errors. The set of excitation coefficients of the compensating feed array is obtained as a complex conjugate of the received focal plane electric field distribution. With this set of excitation coefficients the feed array illuminates the distorted reflector surface with a wavefront designed to compensate for reflector surface distortions. This method of obtaining the compensating array excitations is called direct conjugate field matching (DCFM). Next, the difference of the present DCFM from the other compensating technique will be explained.

In the past, conjugate field matching principle was used for obtaining the compensating element excitation coefficients in applications where degraded reflector antenna performance arises from off-focus feeds (Refs. 11,76,77, and 82). Recently the same technique was applied to the compensation of large scale surface distortions (Refs. 61,65, to 68) with a feed array. It is named indirect conjugate field matching (ICFM) because the transmitting mode and reciprocity theorem were used in determining the feed array excitations. The difference between DCFM and ICFM lies in the following facts:

- (i) DCFM is based on the receiving antenna mode. Hence the tapered plane wave can be conveniently added in the formulation. Since the aperture field and the far field of an antenna are related by a Fourier transform, there is an explicit relation between the plane wave taper and the antenna sidelobe level.
- (ii) The compensating excitation coefficients in ICFM are invariably determined under the condition that the reflector antenna is in a transmitting mode. The aperture field taper is not an explicit design parameter, and therefore cannot be conveniently controlled.

As a consequence, we note that ICFM often leads to antenna patterns with high sidelobe envelopes (see Chapter 4). Such a problem can be alleviated by the present DCFM.

5.3 Computation of the Focal Plane Fields

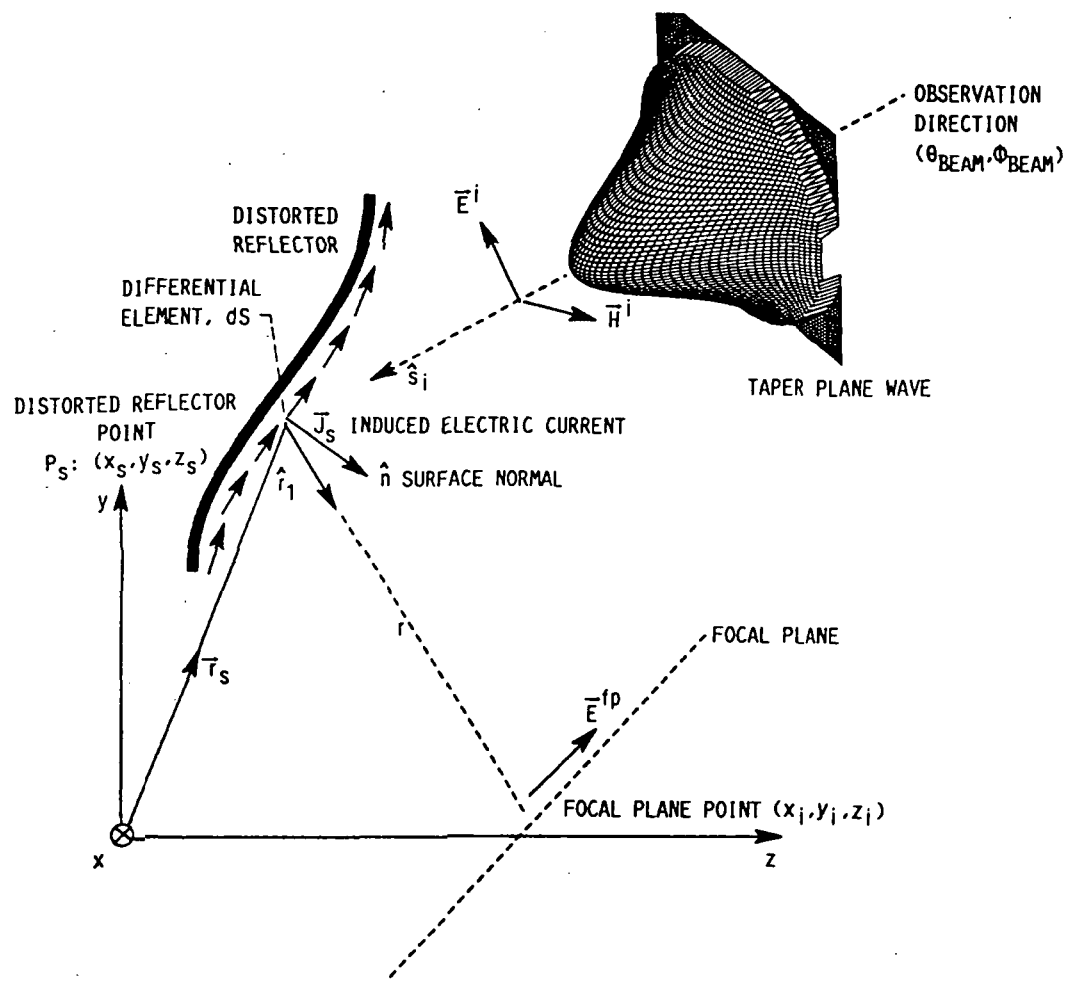
Consider a linearly polarized (\hat{y}) tapered plane wave incident on the distorted reflector surface from an (Fig. 33) observation direction (θ, ϕ) .

$$\vec{E}^i(x_i, y_i, z_i) = E(p) e^{+j\vec{K}\vec{r}} \cdot \hat{K} \hat{u} \quad (5.1)$$

Where,

$$E(p) = c + (1 - c)[1 - (p/a)^2] \quad (5.2a)$$

$$p = \sqrt{[x_s]^2 + [y_s - y_c]^2} \quad (5.2b)$$



33 Geometry for calculating the focal plane electric field distribution

$$c = 10^{ET/20}; \text{ ET: is the edge taper of the incident plane wave} \quad (5.2c)$$

y_c, a : reference lengths (Fig. 34)

(x_s, y_s, z_s) : distorted reflector point

$$\vec{r} = x_s \hat{x} + y_s \hat{y} + z_s \hat{z} \quad (5.2d)$$

$$K = 2\pi/\lambda: \text{ wavenumber} \quad (5.2e)$$

λ : operating wavelength

$$\hat{K} = \sin \theta \cos \phi \hat{x} + \sin \theta \sin \phi \hat{y} + \cos \theta \hat{z} \quad (5.2f)$$

(θ, ϕ) : spherical angles describing the observation direction.

$$\hat{u} = u_x \hat{x} + u_y \hat{y} + u_z \hat{z}: \text{ polarization vector} \quad (5.2g)$$

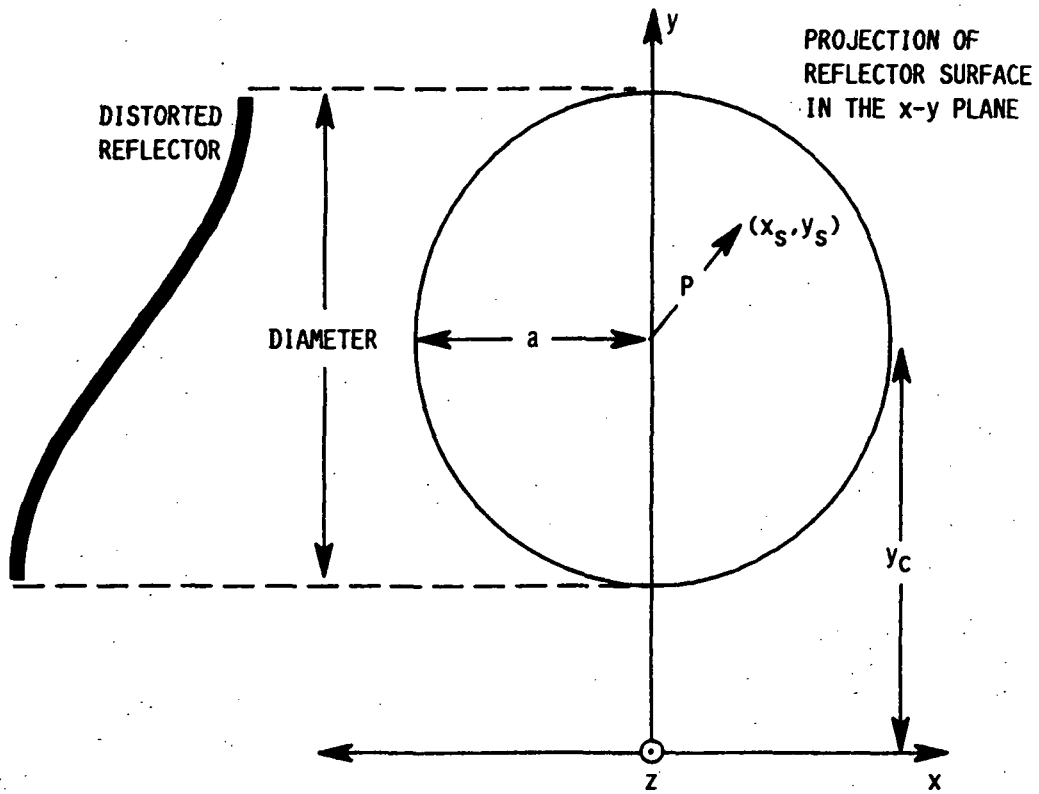
$$u_x = \frac{(-\sin^2 \theta \cos \phi \sin \phi)}{d} \quad (5.2h)$$

$$u_y = \frac{(\cos^2 \theta + \sin^2 \theta \cos^2 \phi)}{d} \quad (5.2i)$$

$$u_z = \frac{(-\cos \theta \sin \theta \sin \phi)}{d} \quad (5.2j)$$

$$d = \{(\sin^2 \theta \cos \phi \sin \phi)^2 + (\cos^2 \theta + \sin^2 \theta \cos^2 \phi)^2 + (\cos \theta \sin \theta \sin \phi^2)\}^{1/2} \quad (5.2k)$$

One needs to calculate the electric field at a point (x_i, y_i, z_i) in the focal plane of the distorted reflector antenna.



34 Geometry for calculating the amplitude tapered of the incident plane wave

The incident electromagnetic field \vec{E}^i, \vec{H}^i induces an electric surface current distribution \vec{J}_s on the distorted reflector surface, which is assumed to be a perfect conductor. The induced electric current distribution (Ref. 5) is given by

$$\vec{J}_s = 2 \hat{n} \times \vec{H}^i \quad (5.3)$$

where

$$\hat{n} = \frac{\frac{df}{dx} \hat{x} + \frac{df}{dy} \hat{y} + \hat{z}}{\sqrt{\left(\frac{df}{dx}\right)^2 + \left(\frac{df}{dy}\right)^2 + 1}} : \text{ surface normal} \quad (5.4)$$

$z_s = f(x_s, y_s)$: distorted reflector surface

By assuming also that the incident field is a transverse electromagnetic wave (TEM) one can make use of the following auxiliary relationship,

$$\vec{H}^i = \frac{\hat{s}_i \times \vec{E}^i}{Z} \quad (5.5)$$

where

$Z = 120 \pi$: free space wave impedance

$$\hat{s}_i = -\sin \theta \cos \phi \hat{x} - \sin \theta \sin \phi \hat{y} - \cos \theta \hat{z} \quad (5.6)$$

Substituting (5.6) into (5.1), yields

$$\vec{J}_s = 2 \{ \hat{n} \times [\hat{s}_i \times \vec{E}^i] \} \quad (5.7)$$

The scattered \vec{E} and \vec{H} fields from the distorted reflector surface in terms of the electric current surface distribution \vec{J}_s is given (Ref. 6) by

$$\vec{E} = \frac{-j}{4\pi\omega\epsilon} \iint \{K^2 \vec{J}_S \psi + (\vec{J}_S \cdot \vec{\nabla}) \vec{\nabla} \psi\} dS \quad (5.8a)$$

$$\vec{H} = \frac{1}{4\pi} \iint (\vec{J}_S \times \vec{\nabla} \psi) dS \quad (5.8b)$$

Where

$\omega = 2\pi f$: and f is the operating frequency, in Hz

$\epsilon = 8.854 \times 10^{-12}$: permittivity of free space (farads/meter)

$$\psi = \frac{e^{-jKr}}{r} \quad (5.9a)$$

$$r = \sqrt{\{(x_i - x_s)^2 + (y_i - y_s)^2 + (z_i - z_s)^2\}} \quad (5.9b)$$

The time dependent factor has been taken as $e^{j\omega t}$ and is omitted through out the analysis.

In the integrands of Eqs. (5.8a) and (b), the operator $\vec{\nabla}$ acts locally on the the coordinates of the source element. By expanding integrand of Eqs. (5.8a) and (b) we obtained the following expressions,

$$\vec{\nabla}(\psi) = \left(jK + \frac{1}{r}\right) \left(\frac{e^{-jKr}}{r}\right) \hat{r}_1 \quad (5.10a)$$

$$(\vec{J}_S \cdot \vec{\nabla}) \vec{\nabla}(\psi) = \left[\{ \vec{J}_S \cdot \hat{r}_1 \} \hat{r}_1 + \frac{3}{r} \left(jK + \frac{1}{r}\right) \{ \vec{J}_S \cdot \hat{r}_1 \} \hat{r}_1 - \frac{\vec{J}_S}{r} \left(jK + \frac{1}{r}\right) \right] \frac{e^{-jKr}}{r} \quad (5.10b)$$

where
$$\hat{r}_1 = \frac{(x_i - x_s) \hat{x} + (y_i - y_s) \hat{y} + (z_i - z_s) \hat{z}}{r} \quad (5.10c)$$

Substituting (5.10a) and (b) into Eqs. (5.8a) and (b) gives the corresponding focal plane fields \vec{E}^{fp} and \vec{H}^{fp}

$$\vec{E}^{fp}(x_i, y_i, z_i) = \frac{-j}{4\pi\omega\epsilon} \iiint \left[k^2 \vec{J}_s - k^2 (\vec{J}_s \cdot \hat{r}_1) \hat{r}_1 + \frac{3}{r} \left(jk + \frac{1}{r} \right) (\vec{J}_s \cdot \hat{r}_1) \hat{r}_1 - \frac{\vec{J}_s}{r} \left(jk + \frac{1}{r} \right) \right] \frac{e^{-jk r}}{r} dS \quad (5.11a)$$

$$\vec{H}^{fp}(x_i, y_i, z_i) = \frac{1}{4\pi} \iiint \left[(\vec{J}_s \cdot \hat{r}_1) \left(jk + \frac{1}{r} \right) \right] \frac{e^{-jk r}}{r} dS \quad (5.11b)$$

5.4 Determination of the Compensating Feed Array Geometry and Element Complex Excitation Coefficients

This section will address the determination of the complex excitation coefficients of the compensating feed array. But before the analysis is presented a broad guideline will be established for obtaining the best compensating array configuration. Several procedures for designing an array-fed reflector antennas have been reported in the literature (Refs. 23,33,61,63,64,68). The most popular approach utilizes the focal plane field distribution as a guideline for obtaining the array boundaries.

To provide reflector distortion compensation, a feed array must be designed such that it will capture the energy spread in the focal plane (receiving mode) and sum it constructively in the feed network. Improvements in antenna performance due to compensation in the receive mode will produce improvements in antenna performance in the transmit mode by reciprocity. To determine the necessary compensating feed array area for capturing the energy spread in the focal plane fields

it is necessary to truncate the focal plane fields to within a predetermined relative value. This is necessary because in general this fields cover a large focal plane area. Another aspect that should be considered in estimating the compensating feed array area lies in the electronics of the devices of the feed network. For example the limiting factors in the amplifiers of the feed network are mostly due to finite dynamic range, noise level and finite number bit quantization levels. These limiting factors determine the minimum amplitude level that can be resolved by the feed network. The minimum amplitude level is used to locate the compensating feed array boundaries by filtering out focal plane fields lower than the minimum amplitude. This process geometrically maps the boundaries of the compensating feed array. With boundaries of the compensating array estimated by truncating the focal plane fields, the next step is to choose a feed array element. The element type is usually determined by the desired reflector gain and sidelobe level (Ref. 63). The number of elements in the feed array can be estimated from the truncated focal plane area divided by the aperture area of the individual element. The element spacing should be keep to a minimum to minimize the spill-over losses. Once the compensating feed array configuration is determined, the relative amplitude and phase of each array element must be determined.

Let us consider a distorted parabolic reflector antenna with a feed array of N elements. The complex excitation coefficients, represented by a column vector \bar{I} ,

$$\bar{I} = [I_1, I_2, I_3, \dots, I_N]^T \quad (5.12)$$

are to be determined. Let us first calculate the focal plane electric field distribution (5.11a) at each (x_i, y_i, z_i) feed array element location. The focal plane electric field distribution is denoted by,

$$\vec{E}^{fp}(x_i, y_i, z_i) = EX_i^{fp} \hat{x} + EY_i^{fp} \hat{y} + EZ_i^{fp} \hat{z} \quad i=1, N \quad (5.13)$$

Let's define the unit vector \hat{p}_f to be the focal plane reference polarization. The distorted reflector geometry and the vector \hat{p}_f are presented in Fig. 35. The unit vector \hat{s}_c is given by Eq. (5.14). This vector is directed from the focal point to the geometrical center of the distorted reflector.

$$\hat{s}_c = \frac{x_c \hat{x} + y_c \hat{y} + (z_c - F) \hat{z}}{\sqrt{(x_c^2 + y_c^2 + (z_c - F)^2)}} \quad (5.14)$$

where

(x_c, y_c, z_c) : coordinate of the geometrical center of the distorted reflector surface

F: focal point

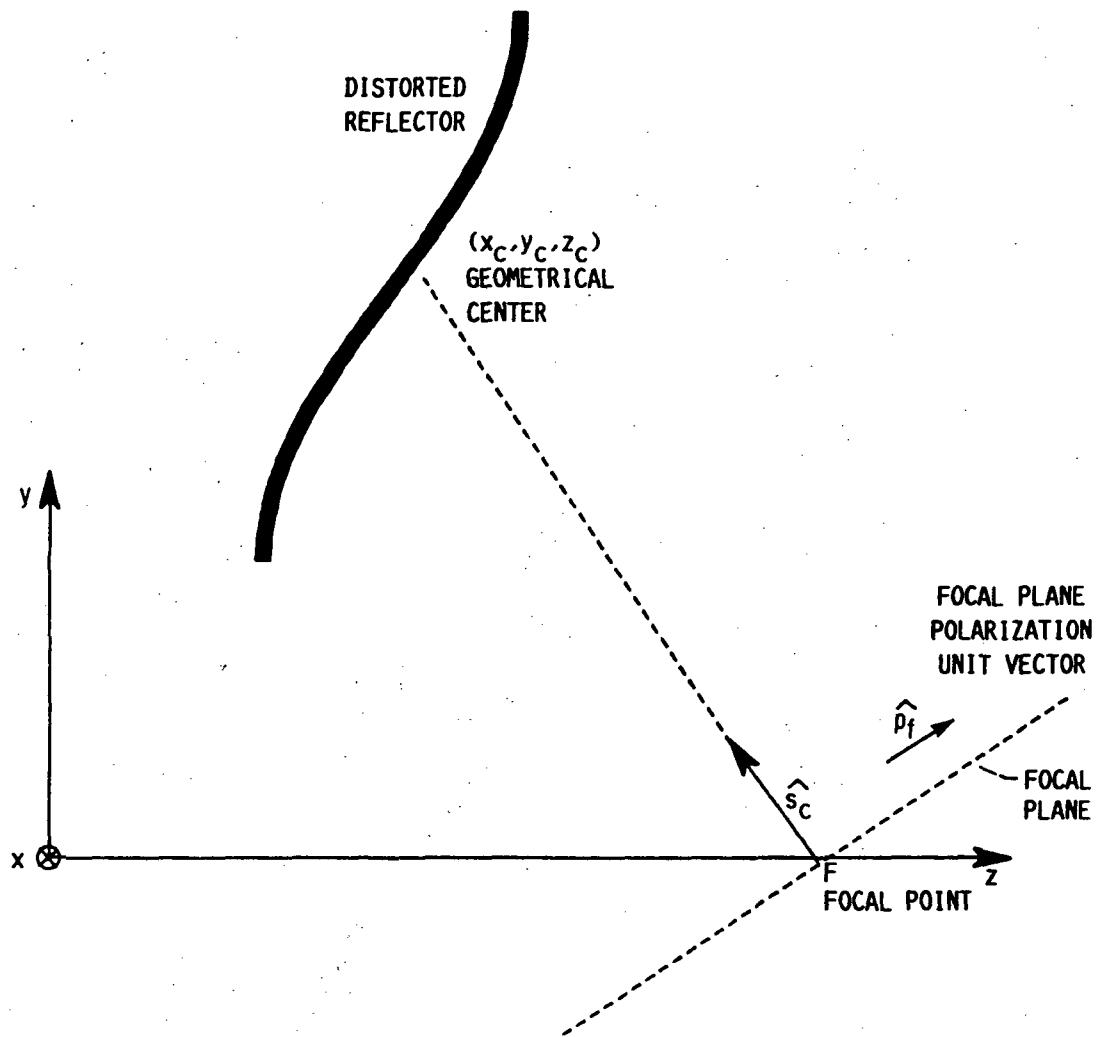
By considering only \hat{y} polarized feed elements, the corresponding reference polarization unit vector is given by,

$$\hat{p}_f = p_x \hat{y} + p_z \hat{z} \quad (5.15)$$

where

$$p_x = \frac{-x_c}{\sqrt{(x_c^2 + y_c^2 + (z_c - F)^2)}} \quad (5.16a)$$

$$p_z = \frac{(z_c - F)}{\sqrt{(x_c^2 + y_c^2 + (z_c - F)^2)}} \quad (5.16b)$$



35 Geometry for calculating the focal plane reference polarization unit vector

Considering only the focal plane electric field in the direction of the focal plane reference polarization vector \hat{p}_f ,

$$E_i = \vec{E}^{fp}(x_i, y_i, z_i) \cdot \hat{p}_f \quad (5.17)$$

Let the column vector

$$\mathbf{E} = [E_1, E_2, E_3, \dots, E_N]^T \quad (5.18)$$

represent the focal plane reference polarization of a distorted reflector at each element location in the feed array.

In the transmitting mode the distorted reflector antenna is being illuminated by the compensating feed array with excitation coefficients that are obtained as a complex conjugate of the reference polarization electric field (Eq. (5.18)) in the focal plane. The resulting compensating complex excitations in the feed array are given by

$$\begin{bmatrix} I_1 \\ I_2 \\ I_3 \\ \vdots \\ I_N \end{bmatrix} = \begin{bmatrix} E_1 \\ E_2 \\ E_3 \\ \vdots \\ E_N \end{bmatrix}^* \quad (5.19)$$

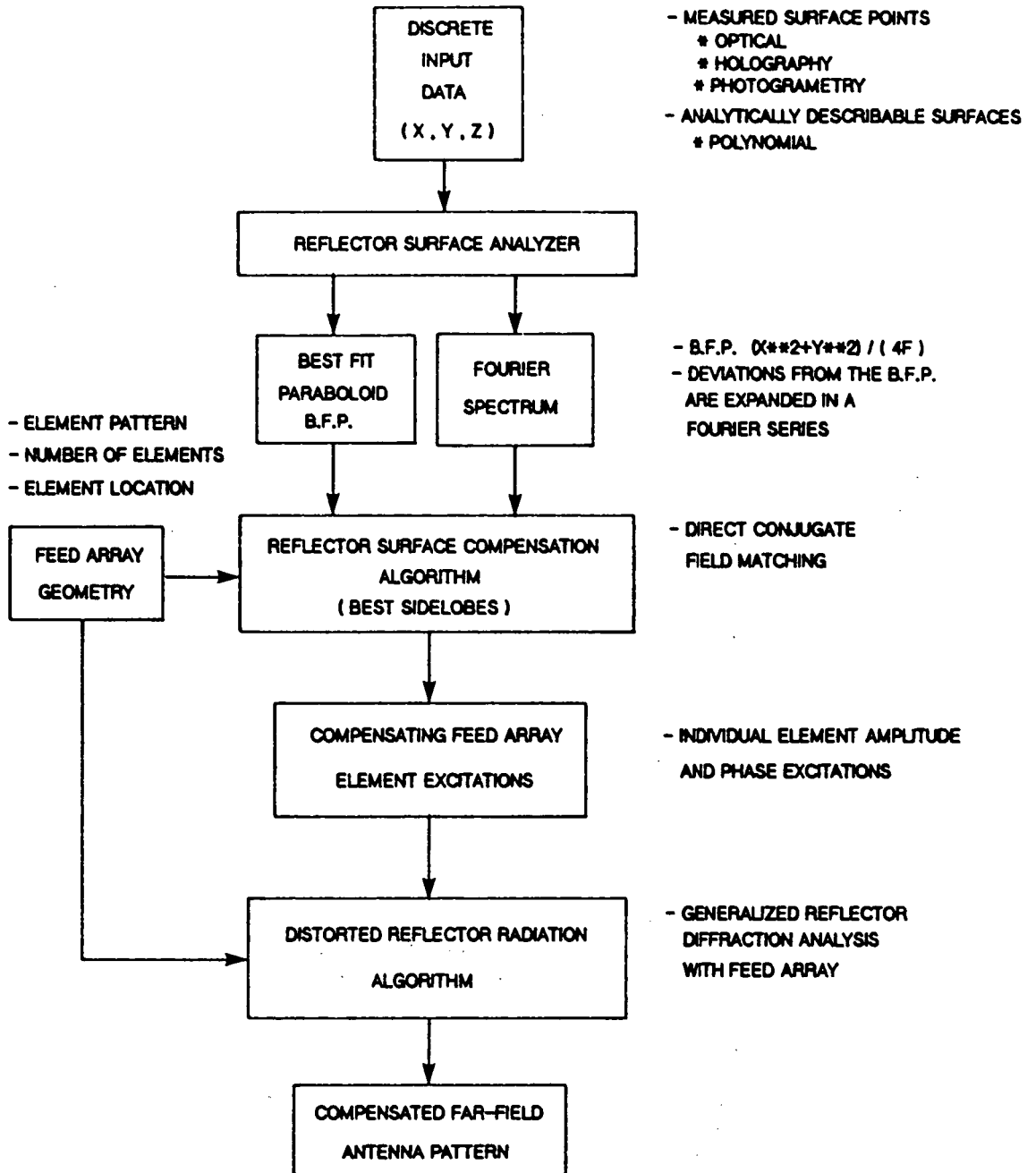
Equation (5.19) describes the direct conjugate field match (DCFM) approach or the receiving approach for compensating the large scale surface distortions. It is called direct because it computes the excitation coefficients directly by integrating the induced currents on the distorted reflector surface.

5.5 Numerical Implementation

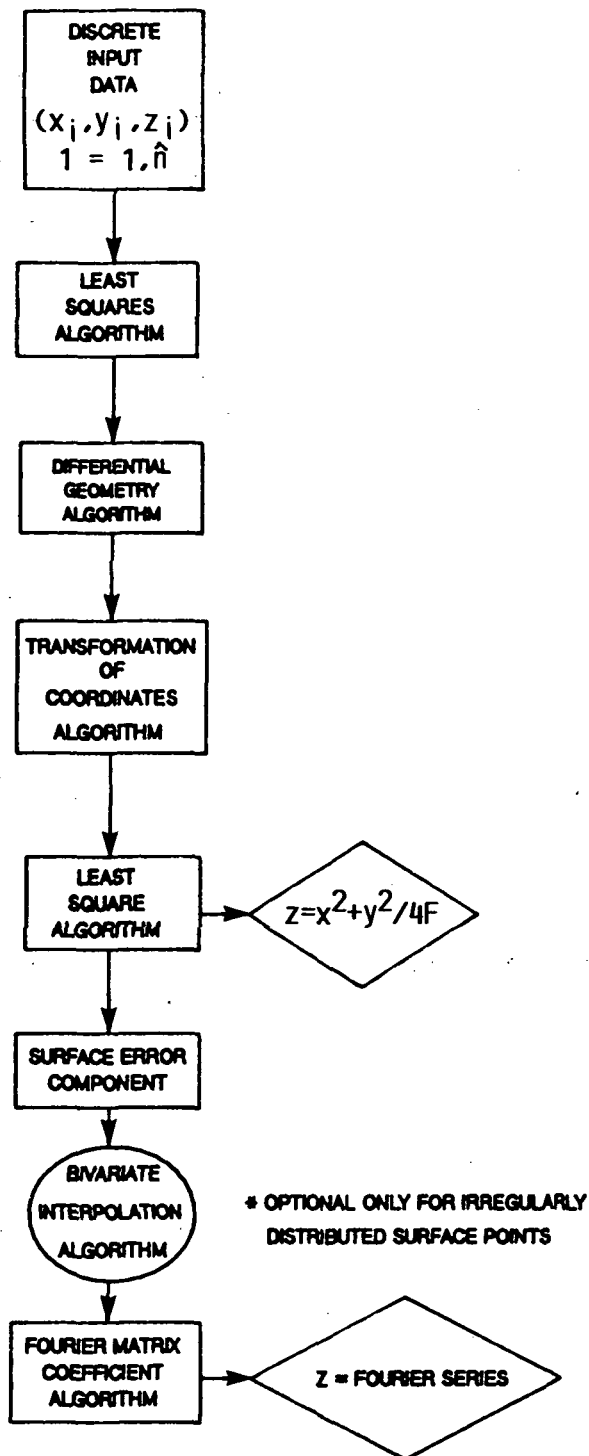
A block diagram of a numerical implementation of the receiving approach for compensating large scale surface distortions is presented in Fig. 36. It consists of three numerical algorithms; a surface analyzer, a compensation analyzer and a radiation pattern analyzer. These algorithms form a complete set of techniques for compensating and evaluating the large scale surface errors (thermal distortions type) in a distorted reflector antenna systems.

The first algorithm, reflector surface analyzer is illustrated in a block diagram in Fig. 37. It takes the distorted reflector surface points as the input and finds the best fit paraboloid polynomial (see chapter 3). The difference between the best fit paraboloid polynomial and the input points (residual) is expanded into a sinusoidal Fourier series. Essentially this algorithm converts the input discrete points into two analytical surface components.

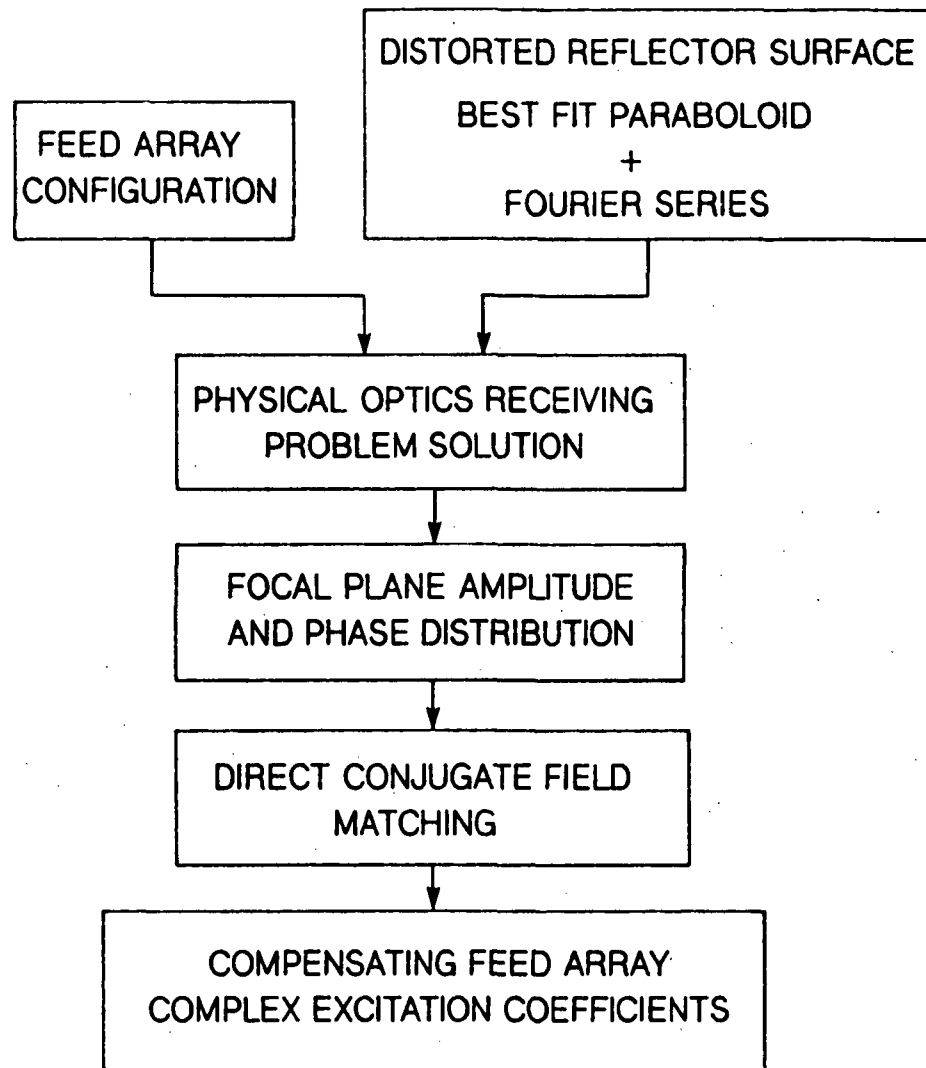
The second algorithm, the compensation analyzer is illustrated in a block diagram in Fig. 38. It determines the focal plane electric field distribution due to a tapered plane wave incident on the distorted reflector from an observation direction. The algorithm uses physical optics techniques for obtaining the focal region fields. The compensating feed array are obtained by assigning the complex conjugate values of the focal region field at the corresponding feed element locations. In summary this algorithm will compute the relative complex excitation coefficients of the feed array.



36 A computer implementation of surface error analysis and compensation algorithm (receiving approach)



37 A block diagram of the reflector surface analyzer algorithm



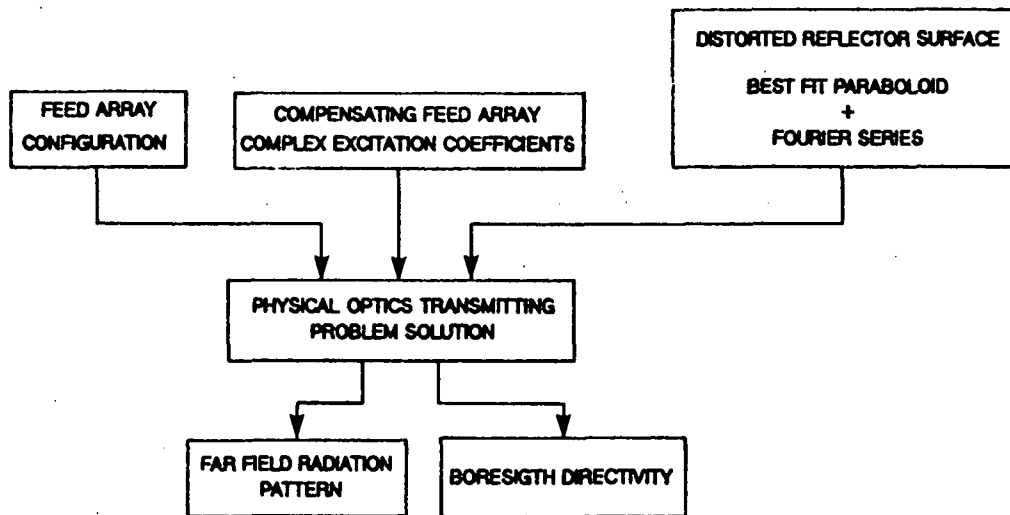
38 A block diagram of the reflector surface compensation algorithm

The third algorithm, distorted reflector radiation analysis is illustrated in a block diagram in Fig. 39. It determines the compensated boresight directivity and far field radiation pattern. The array-fed distorted reflector geometry and compensating array excitation coefficients are the input to this algorithm. The algorithm utilizes a physical optics approach (chapter 2) for obtaining the far field radiation pattern and boresight directivity.

The three algorithms are combined to produce the generalized compensation algorithm for large scale surface distortions. Basically two inputs are to be defined, the feed array geometry and the distorted reflector surface points. The feed array geometry usually contains the feed element type (typically microstrip, open waveguide, horn, etc.), array shape (typically rectangular, hexagonal, etc.), number of elements and relative location of each element. The distorted reflector surface points are usually obtained from optical, microwave holography, photogrammetry, or any other metrology technique. The distorted reflector surface points can be described in either an equally spaced grid or in a nonequally spaced grid.

5.6 Numerical Results and Discussion

To evaluate the usefulness of the receiving approach for compensating large scale surface distortions with a feed array, the distorted reflector surface will be simulated by superimposing a given distortion profile (Fig. 40) into an offset parabolic reflector (Fig. 41). First the effects of truncating the focal plane fields to a finite amplitude level on the compensated boresight directivity and sidelobe envelope will be investigated. Next the effects of tapering

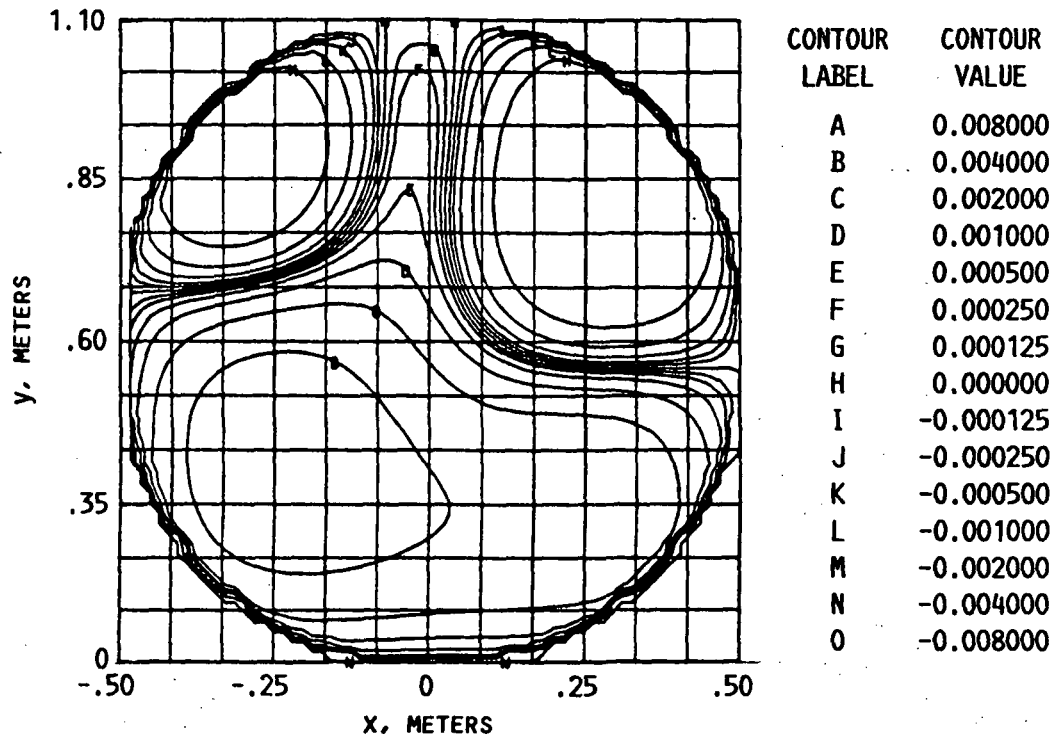


39 A block diagram of the distorted reflector secondary pattern algorithm

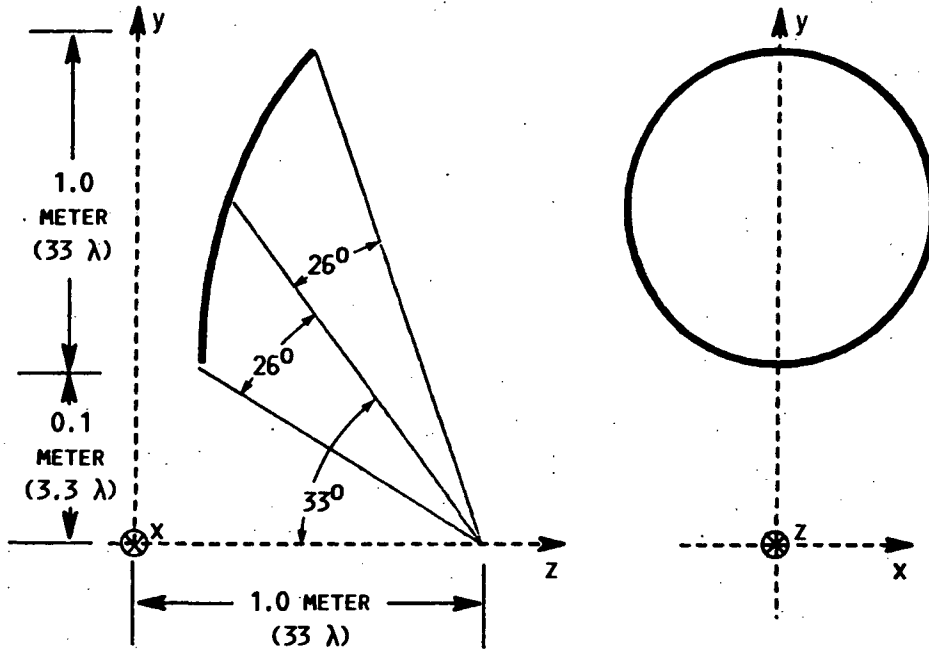
the incident plane wave amplitude on the compensated antenna performance will be studied. For comparison purposes the result of the conjugate field matching technique applied to a simulated distorted reflector will also be presented in this section.

The parameters describing the simulated surface error profile (Fig. 40) are outlined in Table 7. The surface error profile was chosen to resemble a typical large scale distortion profile caused by thermal effects. The undistorted and distorted E-plane radiation pattern obtained by using a single feed element are shown in Figs. 42 and 43 respectively. Table 8 presents a description of the feed parameters. The calculated undistorted and distorted boresight directivities are 39.1 dB and 30.30 dB respectively. The undistorted and distorted antenna performance provides the upper and lower limits in which the compensation technique can be applied.

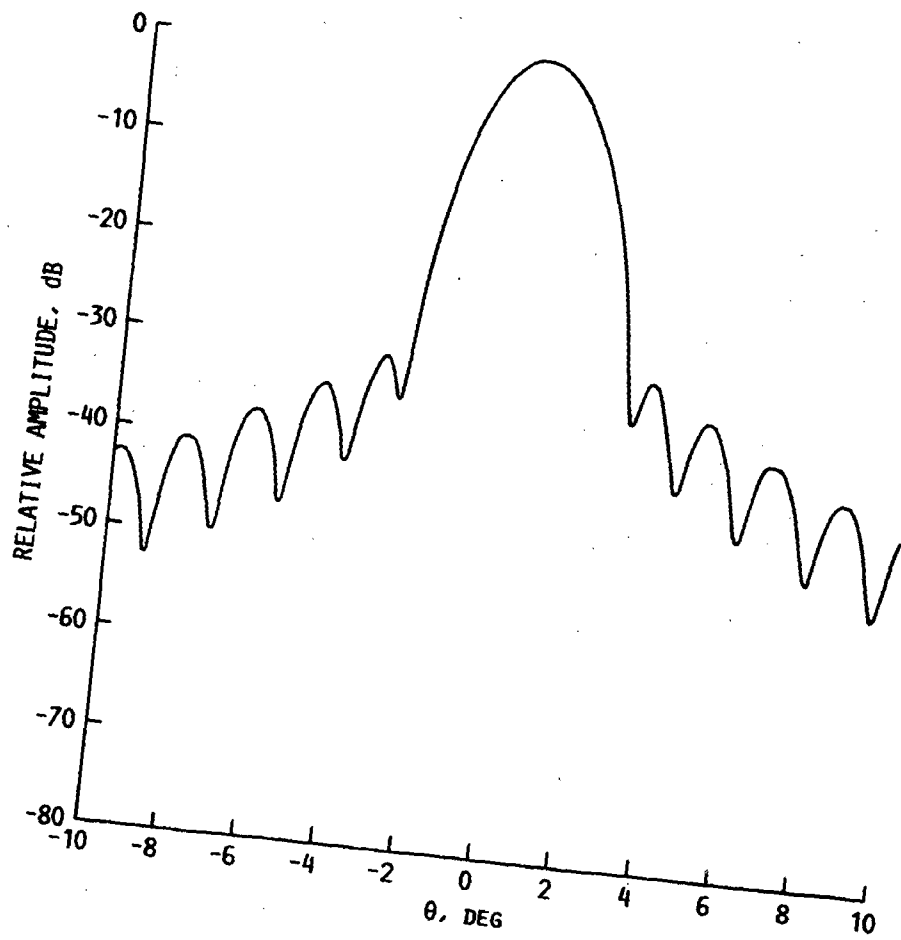
The effects of truncating the focal plane fields at a finite amplitude level are evaluated by first computing the focal plane electric field distribution due to a tapered plane wave (-17 dB) incident on the distorted reflector surface from the boresight direction. The -17 dB taper in the incident plane wave is the required amount of taper for achieving a first sidelobe level of -33 dB in the compensated pattern. This value is calculated from the aperture illumination edge taper consideration that will give rise to a far field sidelobe level of -33 dB. Figure 44 shows a three-dimensional plot of the focal plane electric field distribution resulting from illuminating the distorted reflector with taper plane wave (-17 dB) from the



40 Reflector surface error profile



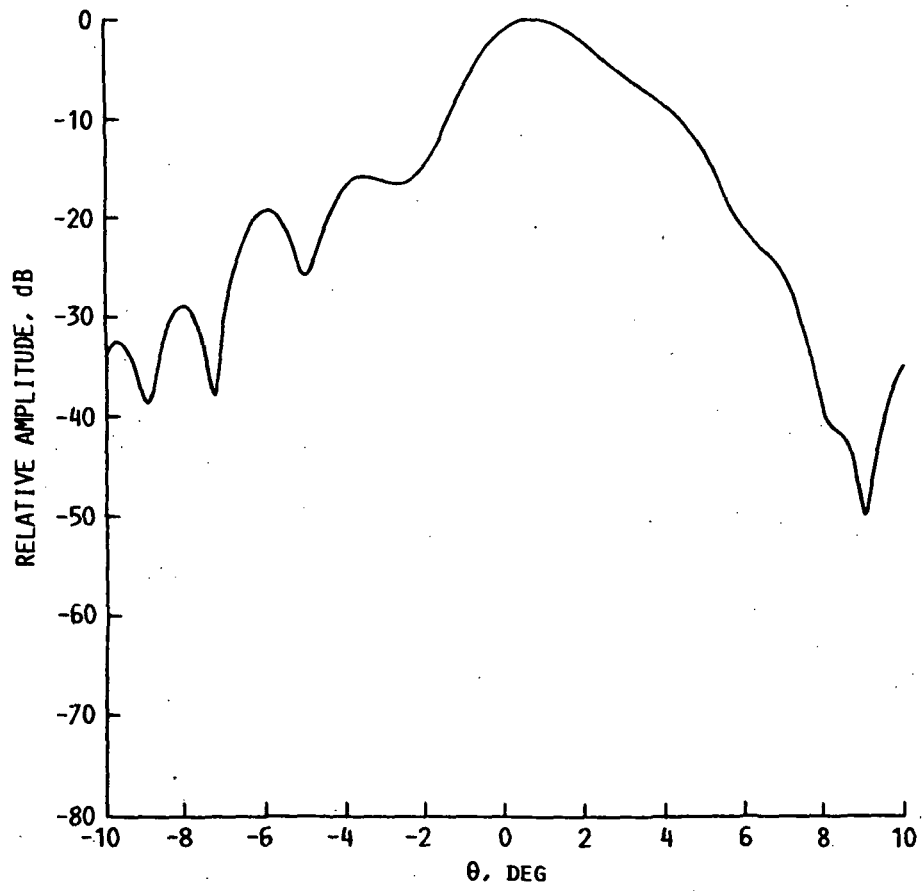
41 Undistorted offset parabolic reflector geometry



42 Undistorted E-plane radiation pattern

TABLE 7. - SURFACE ERROR PROFILE PARAMETERS

TWO-DIMENSIONAL FOURIER COEFFICIENTS IN WAVELENGTHS								
d_{11}	d_{12}	d_{13}	d_{21}	d_{22}	d_{23}	d_{31}	d_{32}	d_{33}
0.001500	0.002100	-0.000900	0.004500	-0.000124	0.002578	-0.000099	-0.000250	-0.000928
TYPICAL ELEMENT IN THE SERIES: $d_{mn} \sin[(y - 0.1)(m)(2\pi)] \sin[(x + 0.5)(n)(2\pi)]$								



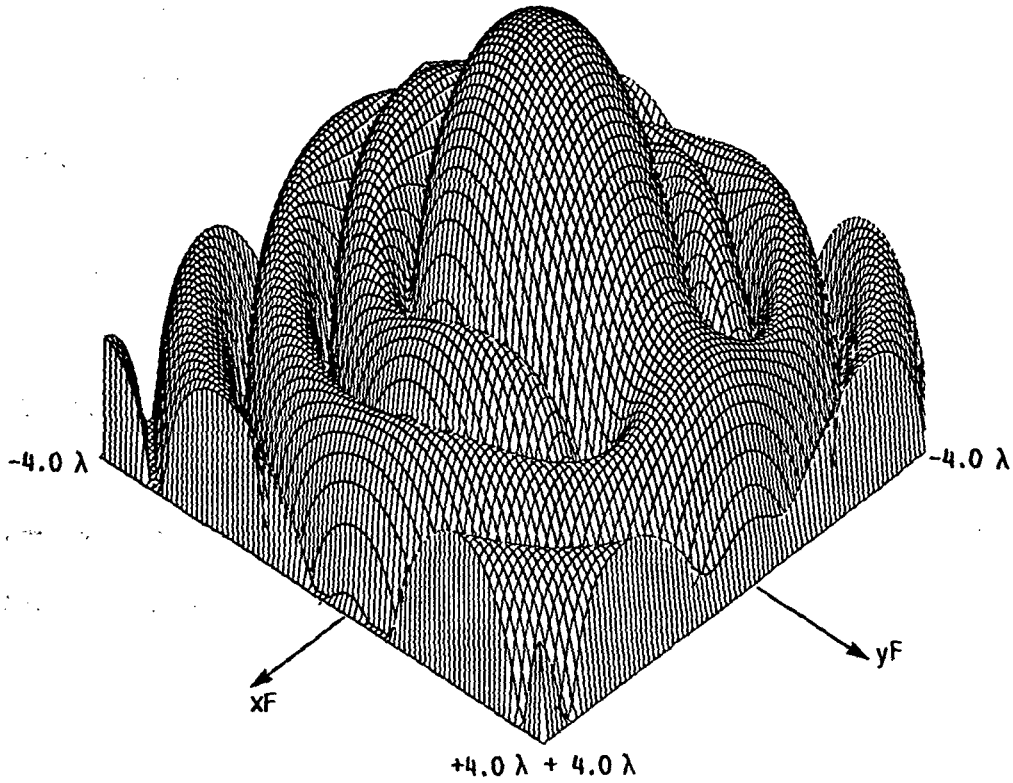
43 Distorted E-plane radiation pattern

TABLE 8. - SUMMARY OF FEED SOURCE PARAMETERS

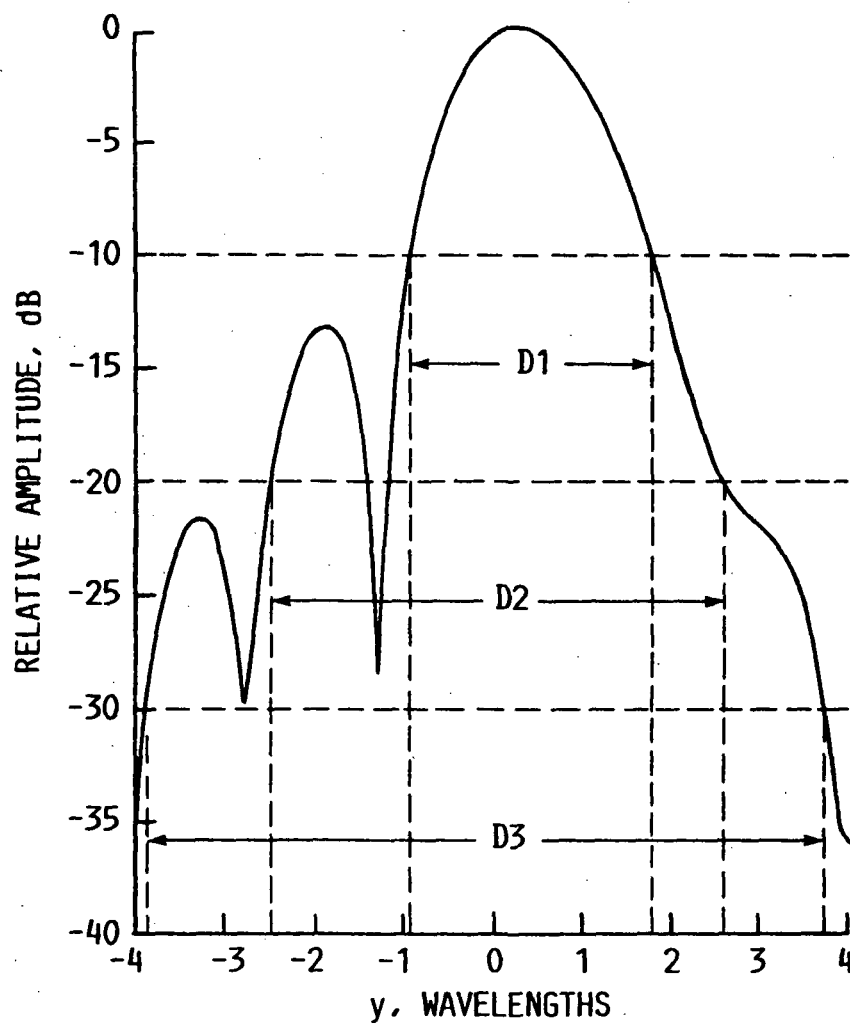
OPERATING FREQUENCY, GHz10
FEED POLARIZATION.	\hat{y} LINEAR
E-PLANE FEED PATTERN $\cos^{qE}(\theta)$	$qE = 17$
H-PLANE FEED PATTERN $\cos^{qH}(\theta)$	$qH = 17$
FEED LOCATION (FOCUS), METERS	(0,0,1.0)
EDGE TAPER, dB	-17

boresight direction. Three different focal fields cutoff (truncating) amplitude levels, -10, -20, and -30 dB will be evaluated. Figure 45 shows a center cut plot of the focal region fields and also shows the corresponding array areas (D1, D2, D3) for the given focal plane field cutoff levels. Figures 46(a) to (c) presents rectangular feed array geometries corresponding to the -10, -20 and -30 dB focal fields cutoff levels respectively. The element spacing and element pattern are the same for all cases. The parameters describing the array elements are presented in Table 9. The resulting compensated E-plane radiation pattern are shown in Figs. 47(a) to (c) respectively. The calculated compensated boresight directivity were 36.51, 34.7, and 32.3 dB respectively. Note the sidelobe envelope was best compensated for the -20, and -30 dB cases. The best compensated boresight directivity was 2.59 dB from the undistorted reflector with a single feed case.

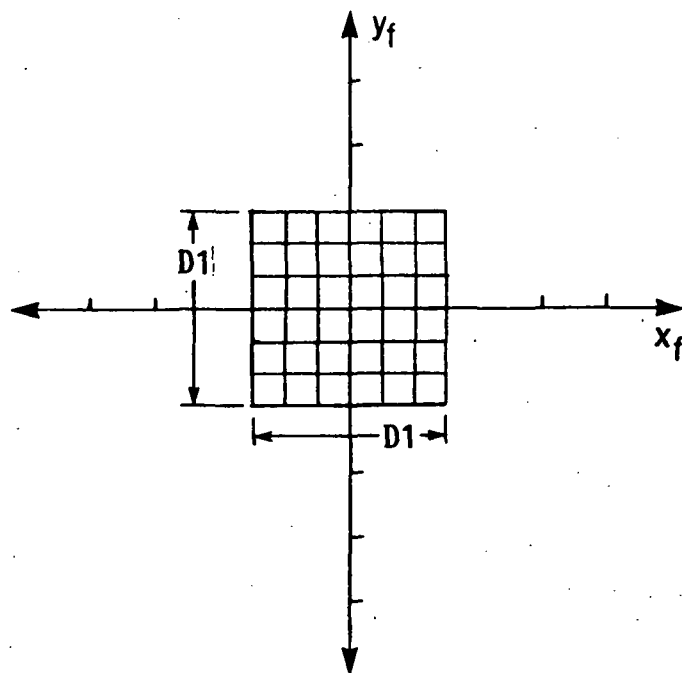
In evaluating the effects of tapering on the incident plane wave the compensating rectangular array configuration that corresponds to the -30 dB focal fields cutoff level (Fig. (46(c))) will be selected. The taper levels that will be examined are 0, -9, -17, and -26 dB. For each taper amplitude level a new set of feed array complex excitation coefficients are computed. Figures 48(a) to (d) presents the compensated E-plane radiation patterns for the 0, -9, -17, and -20 dB taper level case respectively. The calculated boresight compensated directivity were 38.87, 37.56, 36.51, and 32.12 dB respectively. Notice that the best compensated boresight directivity occurs for the 0 dB (Fig. 48(a)) taper, but this case also produced the worst compensated sidelobe level envelopes. The sidelobe envelope is best



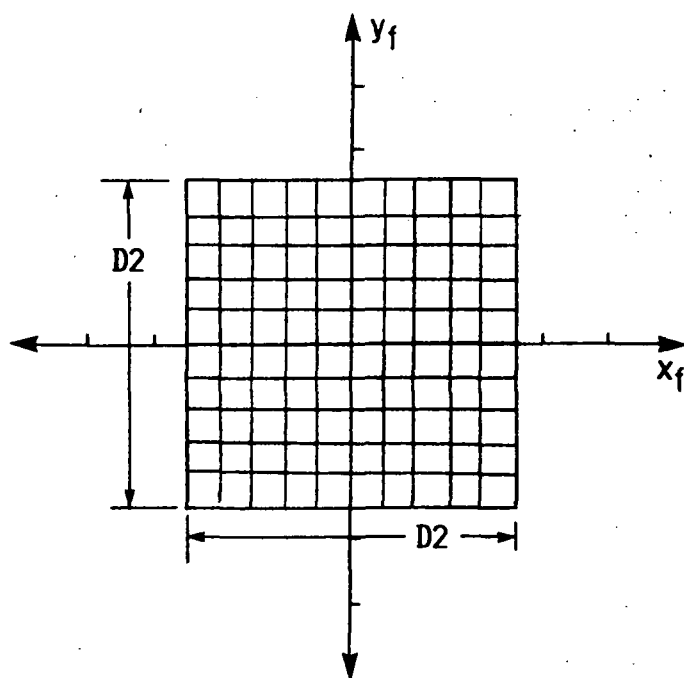
44 Three-Dimensional plot of the focal plane electric field distribution



45 Center cut plot of the focal plane electric field distribution

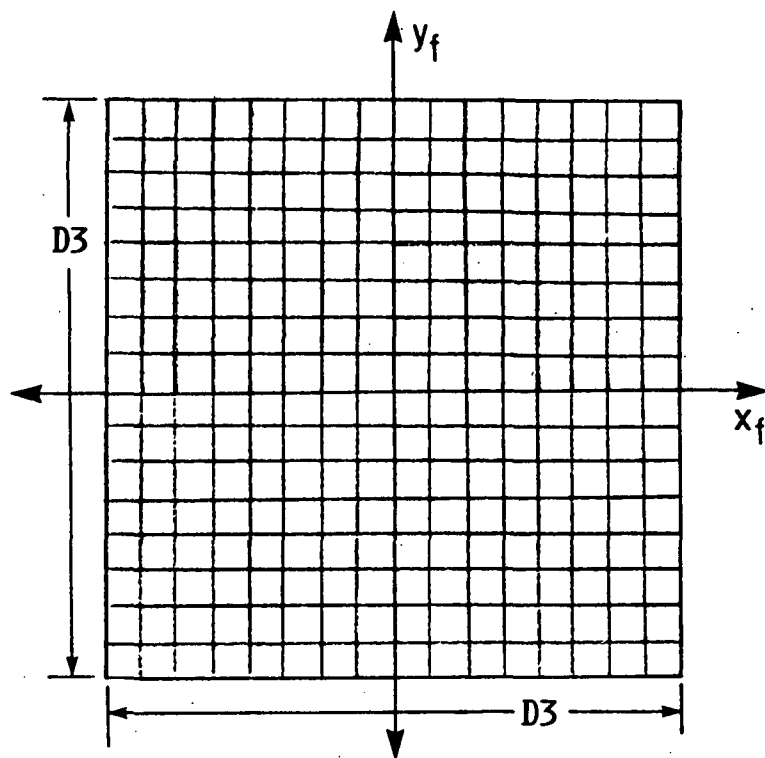


(a) -10 dB focal field cutoff level case.



(b) -20 dB focal field cutoff level case.

46 Feed array geometry

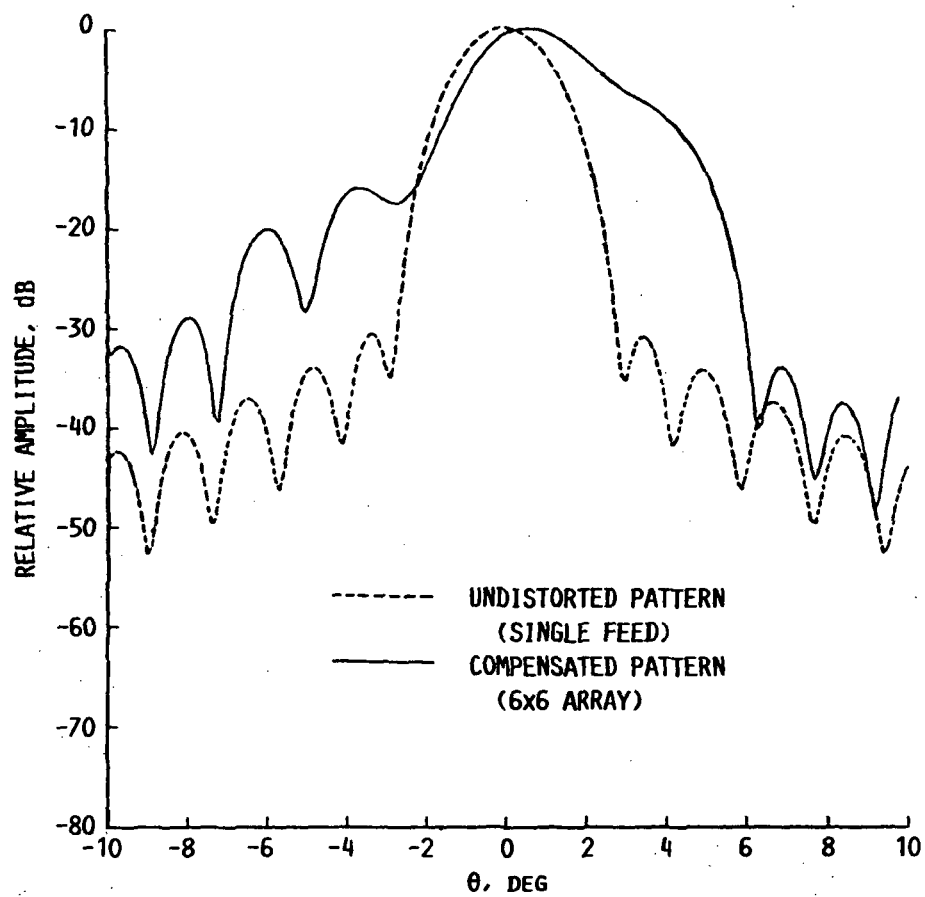


(c) -30 dB focal field cutoff level case.

Fig. 46. - Concl.

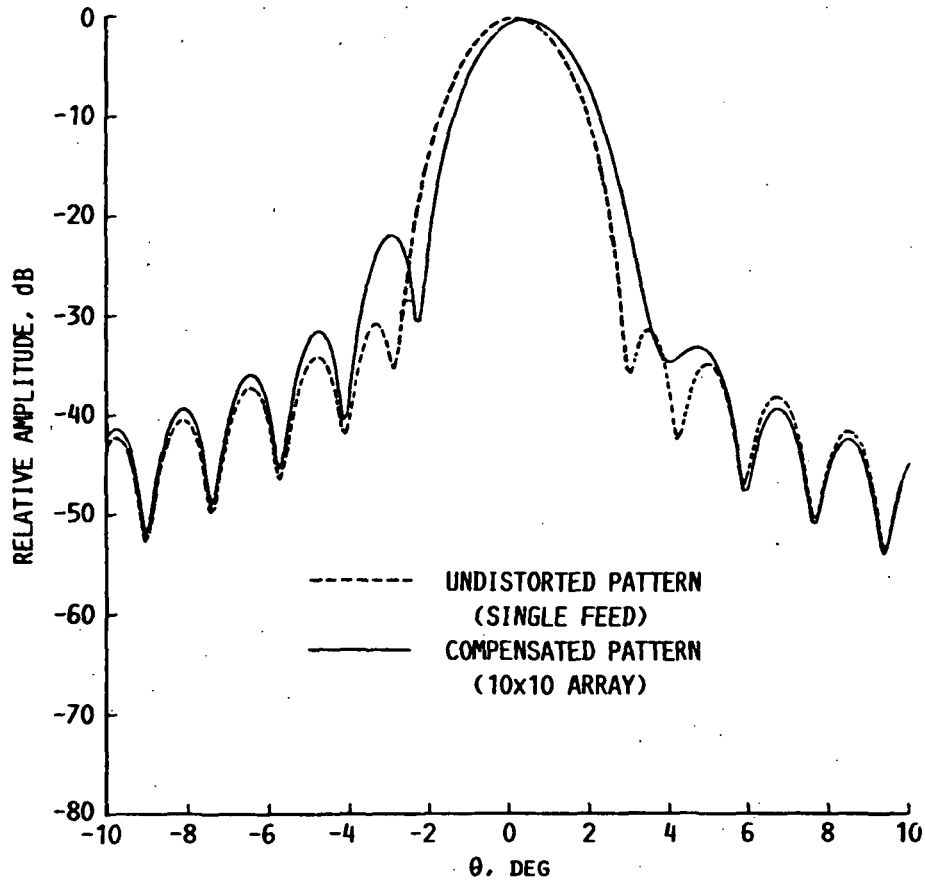
TABLE 9. - SUMMARY OF FEED ARRAY ELEMENT
PARAMETERS

OPERATING FREQUENCY, GHz	10
FEED POLARIZATION.	\hat{y} LINEAR
E-PLANE FEED PATTERN $\cos^{qE}(\theta)$	$qE = 1$
H-PLANE FEED PATTERN $\cos^{qH}(\theta)$	$qH = 1$



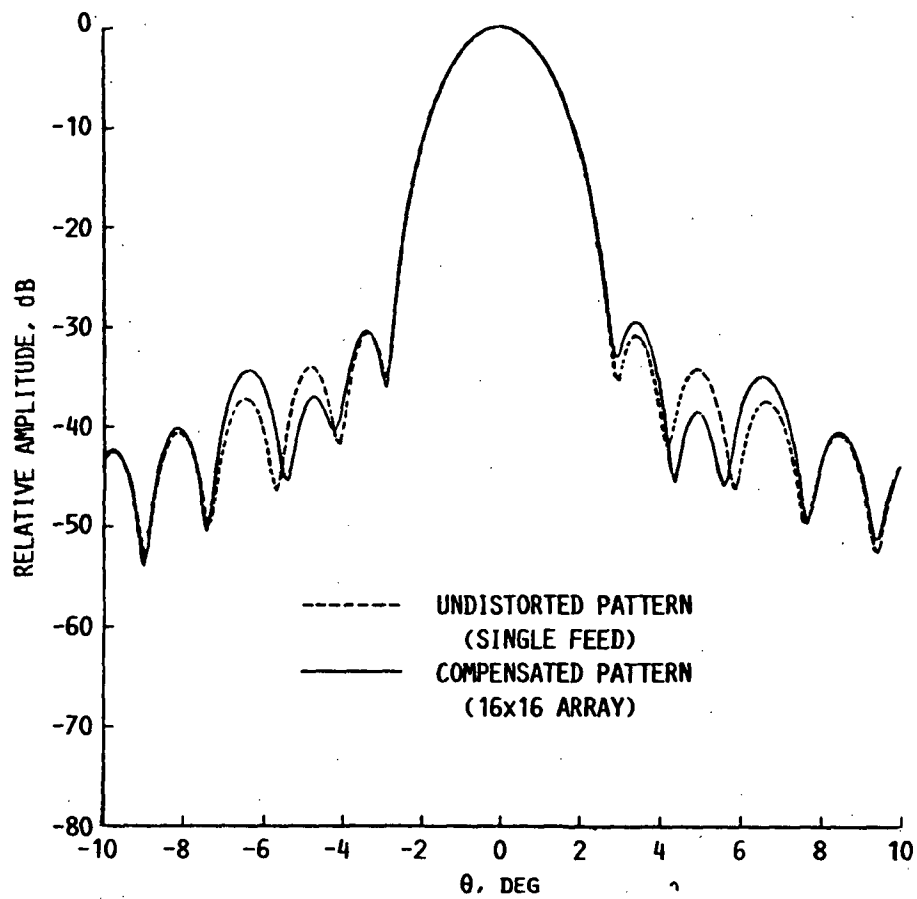
(a) -10 dB focal field cutoff level case.

47 Compensated E-plane radiation pattern



(b) -20 dB focal field cutoff level case.

Fig. 47. - Cont.

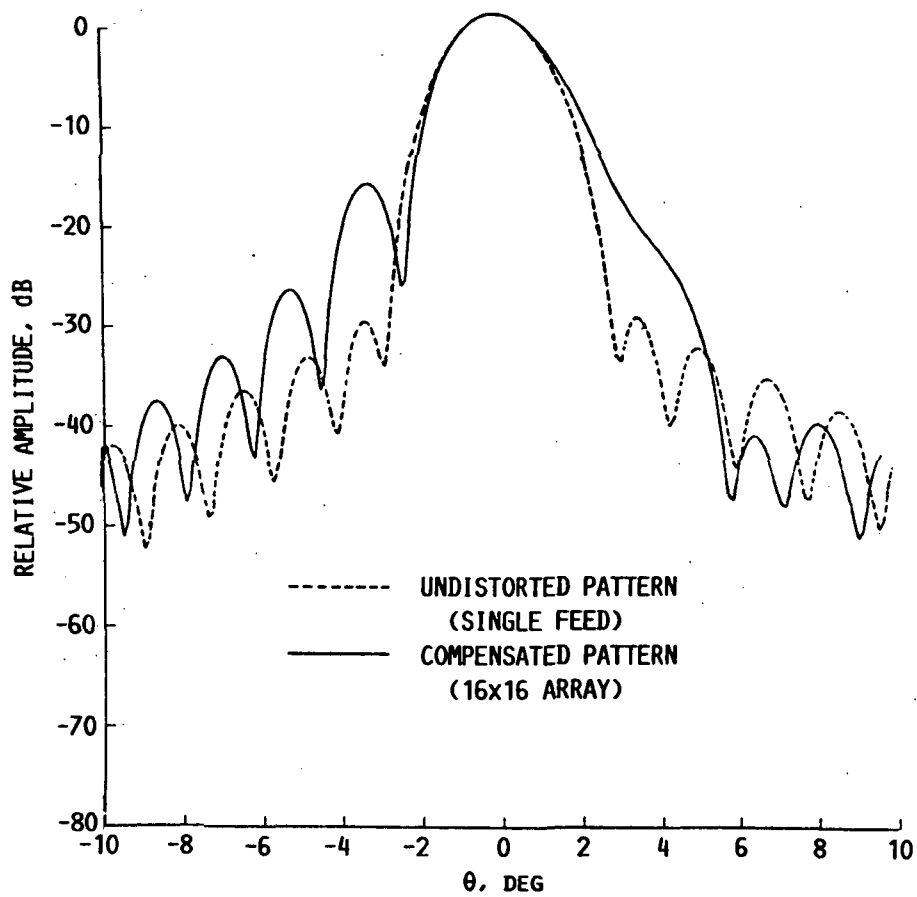


(c) -30 dB focal field cutoff level case.

Fig. 47. - Concl.

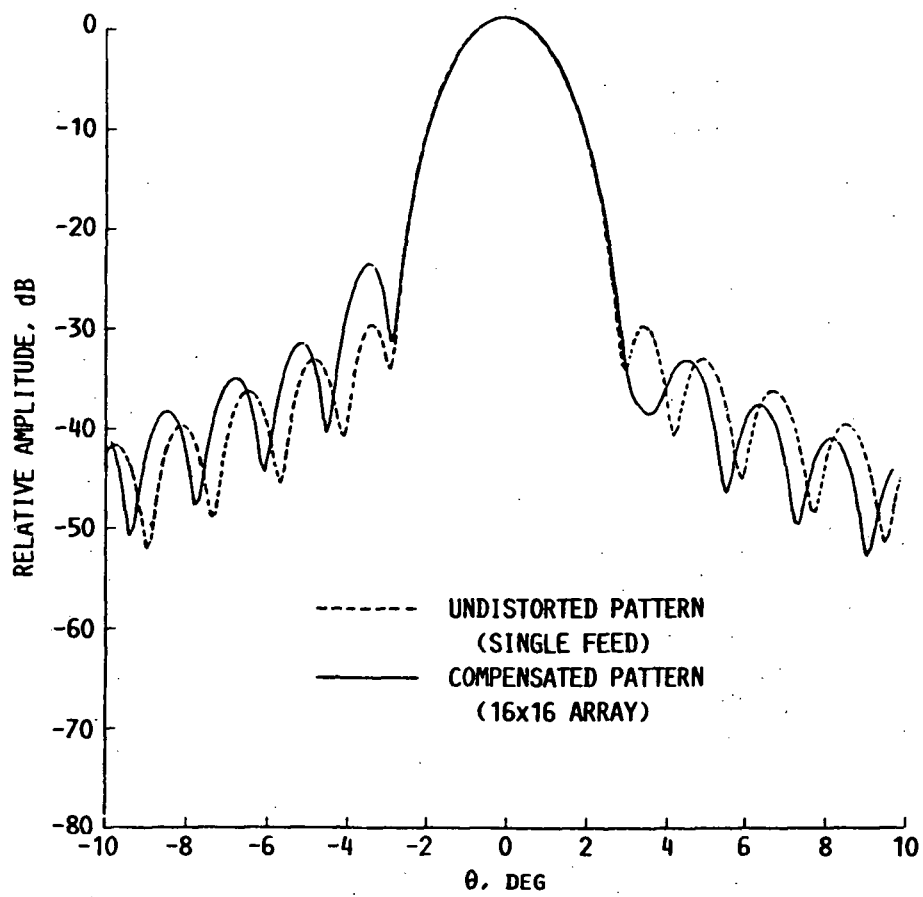
compensated for an amplitude taper of -17 dB (Fig. 48(c)). For the case of -9 dB taper a high sidelobe envelope was obtained and for the -26 dB taper good sidelobe level was achieved but with a lower compensated boresight directivity. This result indicates that tapering the incident plane wave provides a direct control on the compensated sidelobe structure and also achieves a good boresight compensated directivity (within 1 to 3 dB of the undistorted boresight directivity).

In the previous analysis the receiving approach for compensating large scale surface errors has been demonstrated. The next step is to compare the receiving compensating technique with results obtained by the other conjugate field matching approach (see chapter 4): Let us consider the undistorted offset parabolic geometry and a surface error profile shown in Figs. 49 and 50 respectively. The parameters describing the simulated surface error profile are presented in Table 10. Figures 51 and 52 show the undistorted and distorted E-plane radiation patterns obtained with a feed element at the focal point. Table 11 presents the parameters describing the feed element. The antenna boresight directivity has been reduced to 38 dB with the distortion. Let us consider the compensating array geometry in Fig. 53. The compensated E-plane radiation pattern using the receiving approach is shown in Fig. 54. The taper level of the incident plane wave is -15 dB. The compensated E-plane radiation pattern using the transmitting approach (see chapter 4) is shown in Fig. 55. The transmitting approach assumes a uniform plane wave



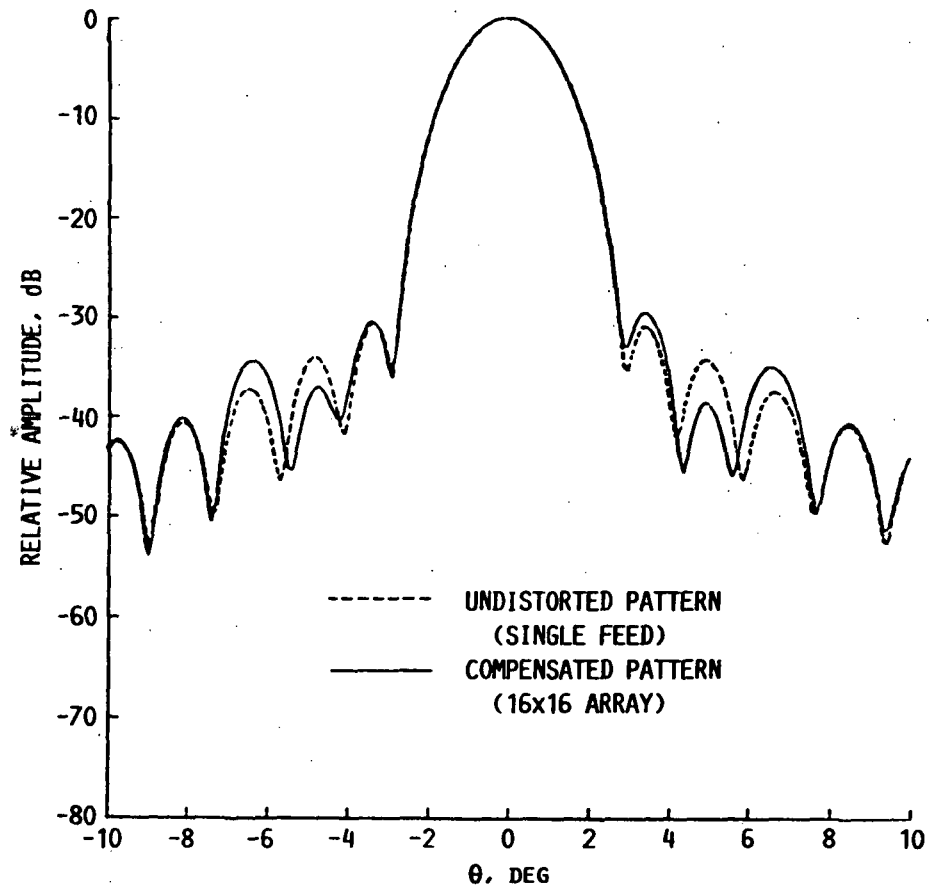
(a) 0 dB amplitude taper case.

48 Compensated E-plane radiation pattern



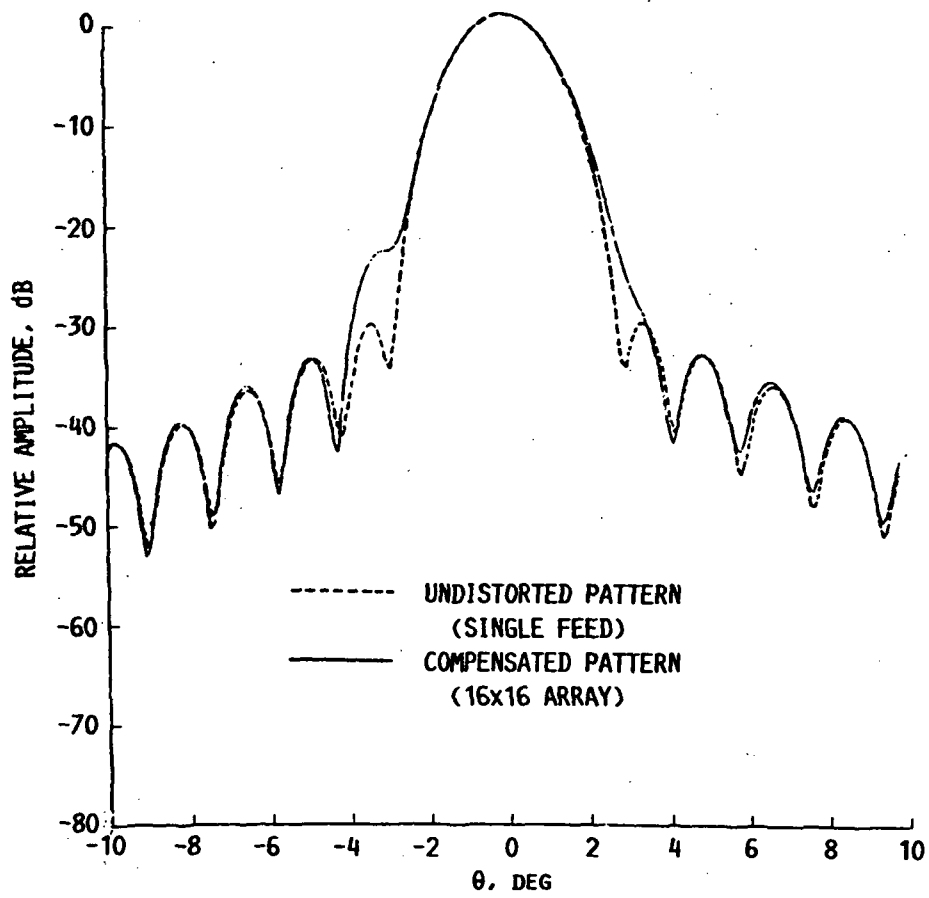
(b) -9 dB amplitude taper case.

Fig. 48. - Cont.



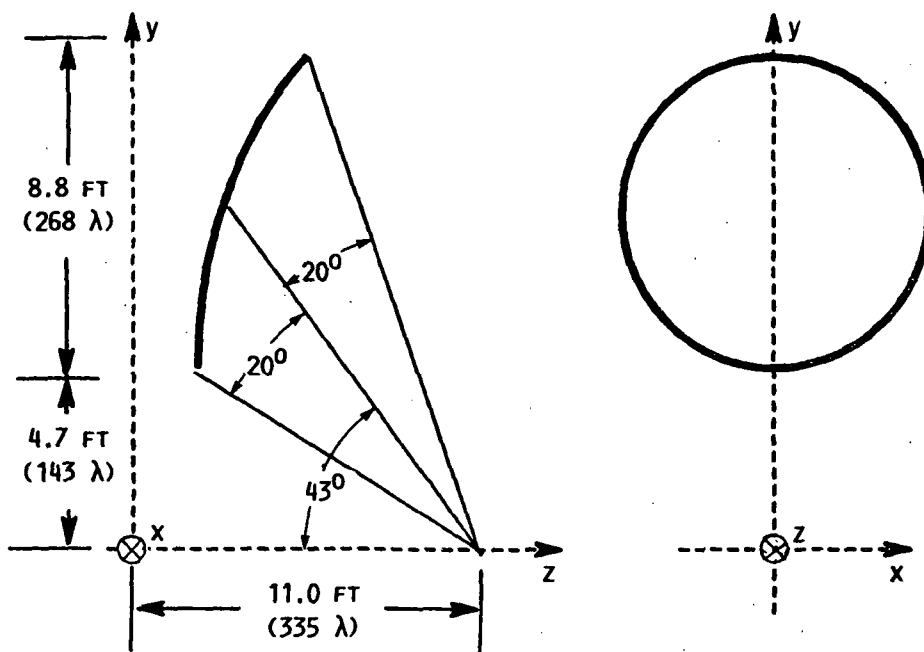
(c) -17 dB amplitude taper case.

Fig. 48. - Cont.

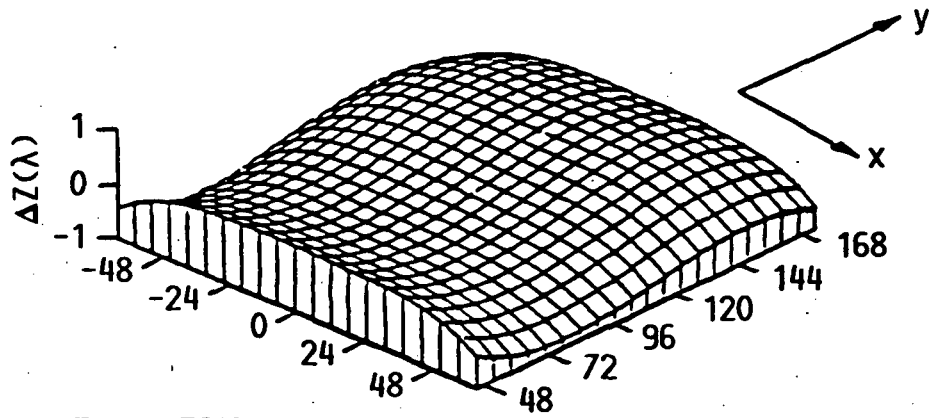


(d) -26 dB amplitude taper case.

Fig. 48. - Concl.



49 Offset parabolic reflector geometry



$$T = 0.7697$$

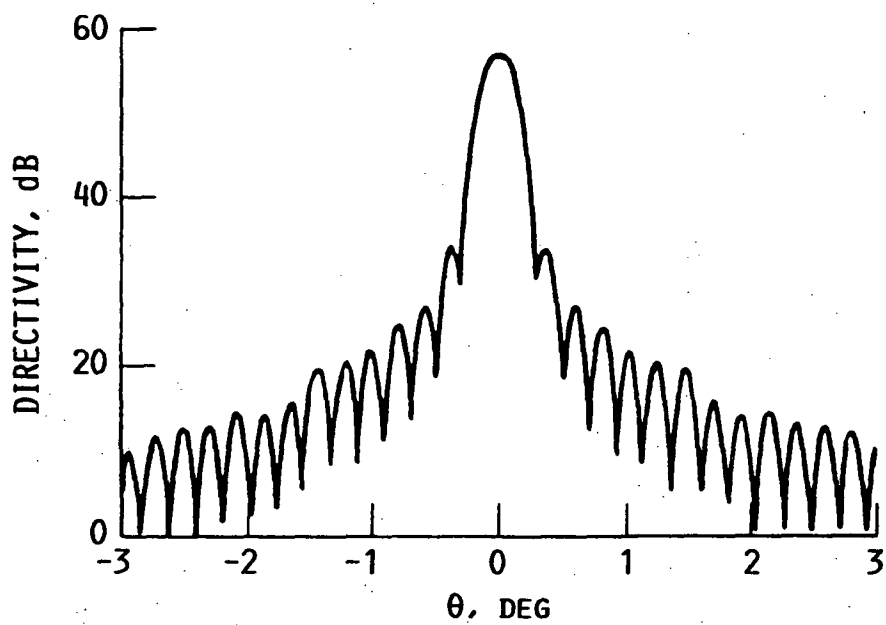
$$B = 0.5\lambda$$

50 Surface error profile

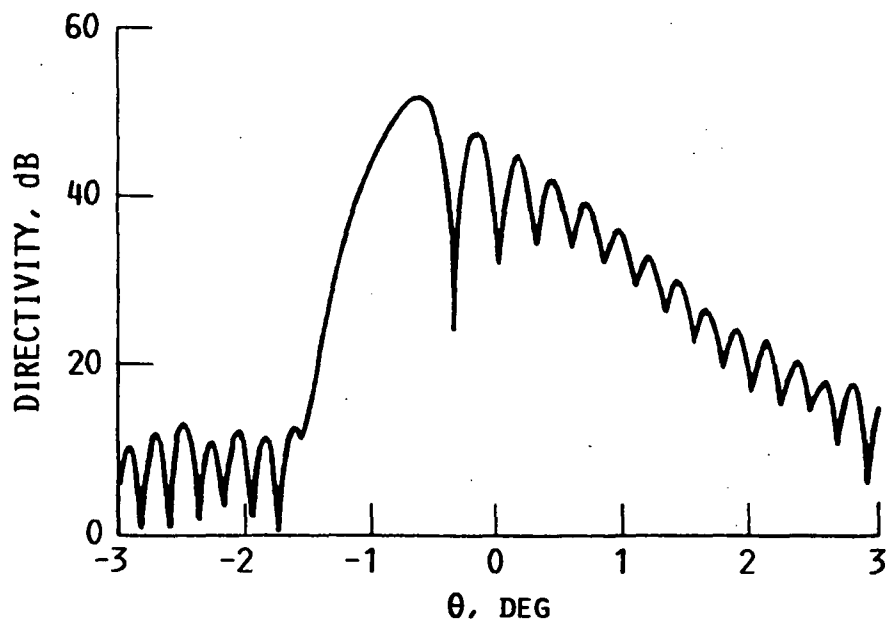
incident on the distorted reflector. The compensated directivity for both approaches were within 2 dB of the undistorted value. The major differences occurred in the compensated sidelobe level envelopes. Note the sidelobe level for the receiving approach were 3 to 5 dB lower than those produced by the transmitting approach. This again indicates that amplitude tapering of the incident plane wave have a direct control on the compensated sidelobe envelopes.

Considering the computational speed, the receiving approach was fast and numerically efficient in computing the compensating feed array coefficients. The receiving approach requires N steps for computing the distorted reflector currents induced by the tapered plane wave. The transmitting approach will require $M \cdot N$ steps, to calculate distorted reflector currents induced by the M feed elements in the focal plane. This makes the transmitting approach slower and numerically inefficient. For the case that has just been illustrated the receiving algorithm was very fast requiring about 20 min of C.P.U. time about 1 hr of C.P.U. time in an IBM 370.

The receiving approach for compensating large scale reflector surface distortions was demonstrated and compared with other exciting techniques. The effects of truncating the focal plane fields to a finite amplitude level and the effects of the tapering the incident plane wave in the receiving approach were investigated. The results shows that the receiving approach was able to compensate sidelobe levels and also provided a reasonably good compensated directivity (withing 1-3 dB). The method also indicates computational ease and suggests its application in an adaptive type of implementation involving large reflector antenna system.



51 Undistorted E-plane radiation pattern



52 Distorted E-plane radiation pattern

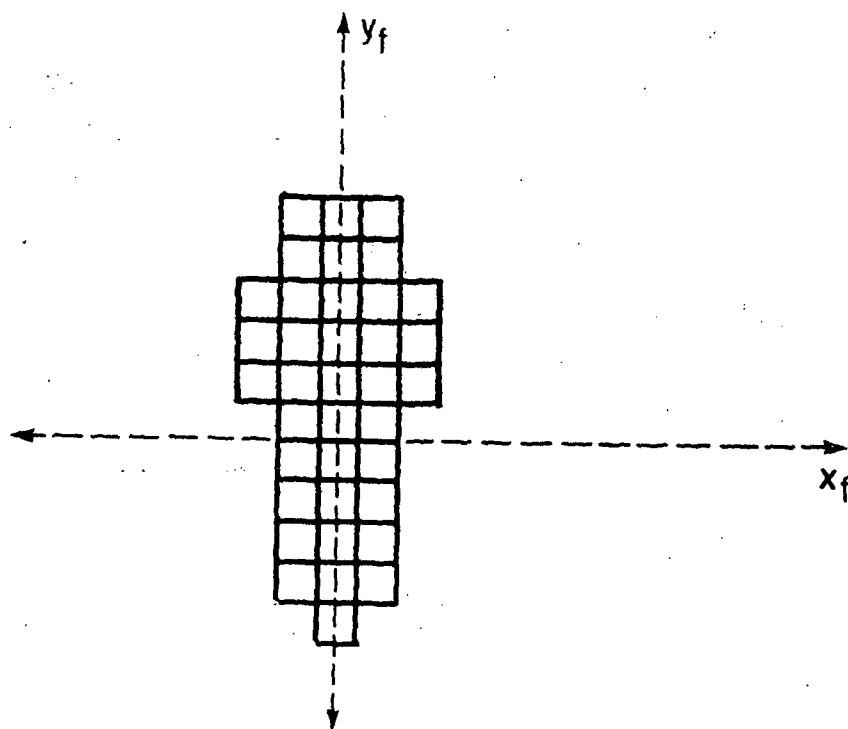
TABLE 10. - SURFACE ERROR PROFILE
PARAMETERS

$$f(x,y) = \beta y \cos \left[\frac{N_y \pi (y - 145.8)}{y_{MAX}} \right]$$

$$\beta y = 0.5\lambda$$

$$N_y = 0.7697$$

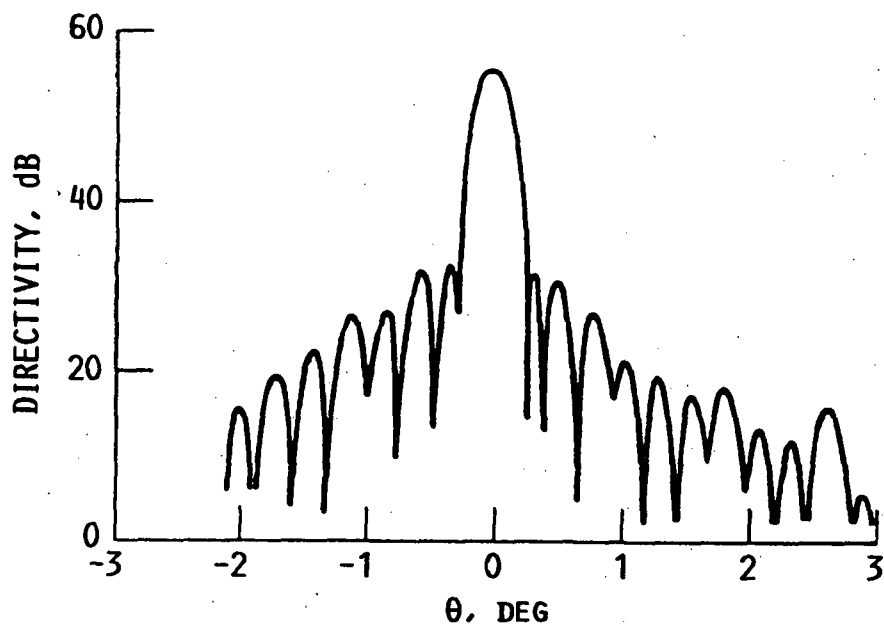
$$y_{MAX} = 52.8 \text{ IN.}$$



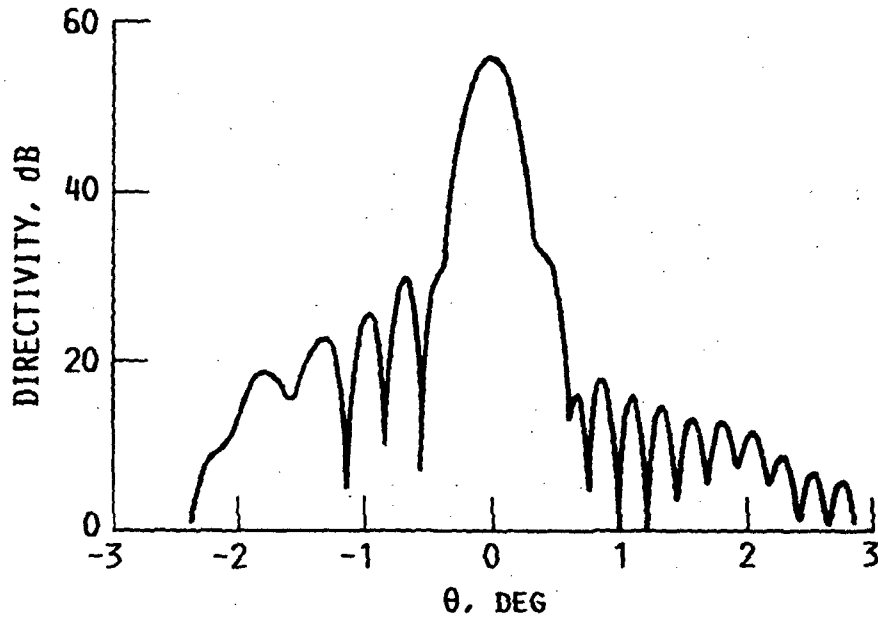
53 Compensating array geometry (37 elements)

TABLE 11. - SUMMARY OF FEED ARRAY PARAMETERS

OPERATING FREQUENCY, GHz	30
FEED POLARIZATION	LINEAR
E-PLANE PATTERN $\cos^{qE}(\theta)$	$qE = 20$
H-PLANE PATTERN $\cos^{qH}(\theta)$	$qH = 20$
FEED LOCATION (FOCUS), METERS	(0,0,3.35)
EDGE TAPER, dB	-11



54 Compensated E-plane radiation pattern using the receiving approach (DCFM)



55 Compensated E-plane radiation pattern using the transmitting transmitting approach (ICFM)

CHAPTER 6

SUMMARY

6.1 Concluding Remarks

The reflector antenna surface distortion arising from thermal effects can be adequately compensated by using an active phased array feed. There are two approaches to design the array excitation coefficients, the indirect conjugate field matching (ICFM) discussed in chapter 4 and the direct conjugate field matching (DCFM) in chapter 5. The DCFM method produces the lowest compensated sidelobe and the ICFM method produces the highest directivity. Due to its computational ease (computational speed) DCFM lends itself to a simple realization in hardware (if the distorted reflector surface is known at all time), and may be very useful in an adaptive type implementation. This is particularly true considering the recent advances in MMIC feed array technology, where each radiating element in the feed array can be controlled independently to provide the compensating excitations (amplitude and phase).

6.2 Suggestion for Future Work

The compensation technique should be experimentally demonstrated by using a distorted reflector with an MMIC feed array. A detection scheme is necessary to obtain the distorted discrete surface points as input to the compensation algorithm for any real time application. The two algorithms can be used in an adaptive implementation for compensating thermal distortion in a space

environment. The method presented here can be extended for nonparabolic surfaces, such as spherical reflectors and should find applications in antennas used in satellite communications, space radiotelescopes, microwave power transmission and radiometers.

REFERENCES

1. Ruze, J.: Antenna Tolerance Theory - A Review. IEEE Proc., vol. 54, no. 4, Apr. 1966, pp. 633-640.
2. Ling, H.; Lo, Y.T.; and Rahmat-Samii, Y.: Reflector Sidelobe Degradation Due to Random Surface Errors. IEEE Trans. Antennas Propag., vol. AP-34, no. 2, Feb. 1986, pp. 164-172.
3. Rusch, W.V.T.: The Current State of the Reflector Antenna Art. IEEE Trans. Antennas Propag., vol. AP-32, no. 4, Apr. 1984, pp. 313-329.
4. Steinbach, R.E.; and Winegar, S.R.: Interdisciplinary Design Analysis of a Precision Spacecraft Antenna. 26th Structures, Structural Dynamics and Materials Conference, Part 1, AIAA, 1985, pp. 704-712.
5. Collin, R.E.; and Zucker, F.J.: Antenna Theory. McGraw-Hill, 1969.
6. Silver, S.: Microwave Antenna Theory and Design. Boston Technical Publisher, Inc., 1964.
7. Rush, W.V.T.; and Potter, P.D.: Analysis of Reflector Antennas. Academic Press, 1970.
8. Wood, P.J.: Reflector Antenna Analysis and Design. The Institute of Electrical Engineers, London, 1980.
9. Harrington, R.F.: The Time-Harmonic Electromagnetic Fields. McGraw-Hill, 1961.
10. Balanis, C.A.: Antenna Theory Analysis and Design. Harper & Row, 1982.

11. Hung, C.C.; and Mittra, R.: Secondary Pattern and Focal Region Distribution of Reflector Antennas Under Wide-Angle Scanning. IEEE Trans. Antennas Propag., vol. AP-31, no. 5, Sept. 1983, pp. 756-763.
12. Rahmat-Samii, Y.; and Galindo-Israel, V.: Shaped Reflector Antenna Analysis Using the Jacobi-Bessel Series. IEEE Trans. Antennas Propag., vol. AP-28, no. 4, July 1980, pp. 425-435.
13. Hung, C.C.: Fourier-Bessel Series Representation for the Far-Field Pattern of Arbitrary Reflector Antennas. Lockheed Missiles and Space Company, Sunnyvale, CA, LMSC Rept. 844955, 1982.
14. Galindo-Israel, V.; and Mitra, R.: A New Series Representation for the Radiation Integral With Application to Reflector Antennas. IEEE Trans. Antennas Propag., vol. AP-25, no. 5, Sept. 1977, pp. 631-641.
15. Mitra, R., et al.: An Efficient Technique for the Computation of Vector Secondary Patterns of Offset Paraboloid Reflectors. IEEE Trans. Antennas Propag., vol AP-27, no. 3, May 1979, pp. 294-304.
16. Ratnasiri, P.A.J.; Kouyoumjian, R.G.; and Pathak, P.H.: The Wide Angle Sidelobes of Reflector Antennas. ElectroScience, The Ohio State University, Columbus, OH, Report 2183-1, 1970.
17. Rusch, W.V.T.: Geometrical Scattering From Inflected Surfaces of Revolution. Tech. Rept., Jet Propulsion Lab., Pasadena, CA, Aug. 1975.
18. Rusch, W.V.T.; and Sorensen, O.: The Geometrical Theory of Diffraction for Axially Symmetric Reflectors. IEEE Trans. Antennas Propag., vol. AP-23, no. 3, May 1975, pp. 414-419.

19. Kauffman, J.F.; Croswell, W.F.; and Jowers, L.J.: Analysis of the Radiation Patterns of Reflector Antennas. IEEE Trans. Antennas Propag., vol. AP-24, no. 1, Jan. 1976, pp. 53-65.
20. Rahmat-Samii, Y.: A Comparison Between GO/Aperture-Field and Physical-Optics Methods for Offset Reflectors. IEEE Trans. Antennas Propag., vol. AP-32, no. 3, Mar. 1984, pp. 301-306.
21. Albertsen, N.C.; and Pontoppidan, K.: Analysis of Subreflectors for Dual Reflector Antennas. Proc. IEE, vol. 131, pt. H, no. 3, June 1984, pp. 205-213.
22. Acosta, R.J.: Secondary Pattern Computation of an Offset Reflector Antenna. NASA TM-87160, 1985.
23. Lam, P.T.C.; Lee, S.W.; and Acosta, R.: Secondary Pattern Computation of an Arbitrarily Shaped Main Reflector. NASA TM-87162, 1985.
24. Franceschetti, G.; and Mohsen, A.: Recent Developments in the Analysis of Reflector Antennas: A Review. IEE Proc., vol. 133, pt. H., no. 1, Feb. 1986, pp. 65-76.
25. Rudge, A.W.; and Adata, N.A.: Offset-Parabolic Reflector Antennas: A Review. IEEE Proc., vol. 66, no. 12, Dec. 1978, pp. 1592-1618.
26. Luneberg, R.K.: Mathematical Theory of Optics. Brown University, Providence RI, 1944.
27. Kline, M.: An Asymptotic Solution of Maxwell's Equation. Symposium on the Theory of Electromagnetic Waves. Interscience, 1951.

28. Kummer, W.H.; and Gillespie, E.: Antenna Measurements - 1978. IEEE Proc., vol. 66, no. 4, Apr. 1978, pp. 483-507.
29. Rahmat-Samii, Y.: Useful Coordinate Transformations for Antenna Applications. IEEE Trans. Antennas Propag., vol. AP-27, no. 4, July 1979, pp. 571-574.
30. Akima, H.: A Method of Bivariate Interpolation and Smooth Surface Fitting for Irregularly Distributed Data Points. ACM Trans. Math. Software, vol. 4, no. 2, June 1978, pp. 148-159.
31. Shepard, D.: A Two-Dimensional Interpolation Function for Irregularly-Spaced Data. Proc. ACM National Conference, 1968, pp. 517-524.
32. Ngai, E.C.; and Profera, C.E., Jr.: Application of Bivariate Interpolation to Antenna Related Problems. IEEE Trans. Antennas Propag., vol. AP-32, no. 7, July 1984, pp. 735-739.
33. Lam, P.T., et al.: Directivity Optimization of a Reflector Antenna With Cluster Feeds: A Closed-Form Solution. IEEE Trans. Antennas Propag., vol. AP-33, no. 11, Nov. 1985, pp. 1163-1174.
34. Lee, S.W.; and Cramer, P.W., Jr.: Determination of Specular Points on a Surface of Revolution. IEEE Trans. Antennas Propag., vol. AP-29, no. 4, July 1981, pp. 662-664.
35. Kouyoumjian, R.G.: Asymptotic High-Frequency Methods. IEEE Proc., vol. 53, no. 8, Aug. 1965, pp. 864-876.
36. Lee, S.W.: Electromagnetic Reflection From a Conducting Surface: Geometrical Optics Solution. IEEE Trans. Antennas Propag., vol. AP-23, no. 2, Mar. 1975, pp. 184-191.

37. Keller, J.B.: Geometrical Theory of Diffraction. J. Opt. Soc. Am., vol. 52, no. 2, Feb. 1962, pp. 116-130.
38. Lee, S.W.: Uniform Asymptotic Theory on Electromagnetic Edge Diffraction: A Review. Electromagnetic Scattering, P.L.E. Uslenghi, ed., Academic Press, 1978, pp. 67-119.
39. Ahluwalia, D.S.; Lewis, R.M.; and Boersma, J.: Uniform Asymptotic Theory of Diffraction by a Plane Screen. SIAM J. Appl. Math., vol. 16, no. 4, July 1968, pp. 783-807.
40. Lewis, R.M.; and Boersma, J.: Uniform Asymptotic Theory of Edge Diffraction. J. Math. Phys., vol. 10, no. 12, Dec. 1969, pp. 2291-2305.
41. Lee, S.W.; and Deschamps, G.A.: A Uniform Asymptotic Theory of Electromagnetic Diffraction by a Curved Wedge. IEEE Trans. Antennas Propag., vol. AP-24, no. 1, Jan. 1976, pp. 25-34.
42. Kouyoumjian, R.G.; and Pathak, P.H.: A Uniform Geometrical Theory of Diffraction for an Edge in a Perfectly Conducting Surface. IEEE Proc., vol. 62, no. 11, Nov. 1974, pp. 1448-1461.
43. Lee, S.W., et al.: Diffraction by an Arbitrary Subreflector: GTD Solution. IEEE Trans. Antennas Propag., vol. AP-27, no. 3, May 1979, pp. 305-316.
44. Ufimtsev, P.Y.: The Method of Edge Waves in the Physical Theory of Diffraction. Sovjetskaye Rad, Moscow, 1962.
45. Lam, P.T., et al.: Strategy for Reflector Pattern Calculation: Let the Computer do the Work. NASA TM-87137, 1985.
46. Ludwig, A.C.: The Definition of Cross Polarization. IEEE Trans. Antennas Propag., vol. AP-21, no. 1, Jan. 1973, pp. 116-119.

47. Chan, K.K.; and Raab, A.R.: Surface-Current Analysis of Distorted Reflector Antennas. IEE Proc., vol. 128, pt. H, no. 4, July 1981, pp. 206-212.
48. Agrawal, P.K.; Kauffman, J.F.; and Croswell, W.F.: A Method for Pattern Calculation for Reflector Antennas Whose Geometry is Described by a Finite Number of Discrete Surface Points. IEEE 1979 Antennas and Propagation International Symposium Digest, Vol. 1, IEEE, 1979, pp. 67-70.
49. Mittra, R.; and Rushdi, A.: An Efficient Approach for Computing the Geometrical Optics Field Reflected from a Numerically Specified Surface. IEEE Trans. Antennas Propag., vol. AP-27, no. 6, Nov. 1979, pp. 871-877.
50. Lee, R.Q.; and Acosta, R.: A Numerical Method for Approximating Antenna Surfaces Defined by Discrete Surface Points. NASA TM-87125, 1985.
51. Parekh, S.: On the Solution of Best Fit Paraboloid as Applied to Shaped Dual Reflector Antennas. IEEE Trans. Antennas Propag., vol. AP-28, no. 4, July 1980, pp. 560-562.
52. Graham, B.S.; Graham, R.K.; and Wolton, I.C.: Synthesis of Dual-Offset Shaped Reflectors for Arbitrary Aperture Shapes Using Continuous Domain Deformations. IEE Proc., vol. 133, pt. H, no. 1, Feb. 1986, pp. 57-64.
53. Harrington, R.F., Field Computation by Moment Method. Krieger, Malabar, FL, 1982.
54. DeBoor, C.: Bicubic Spline Interpolation. J. Mathematics and Phys., vol. 41, 1962, pp. 212-218.

55. Davies, W.A.: Splines for Electromagnetics. IEEE Trans. Antennas Propag., vol. AP-30, no. 4, July 1982, pp. 760-764.
56. Goldstein, H.: Classical Mechanics. Addison-Wesley, 1950, pp. 107-109.
57. James, M.L.; Smith, G.M.; and Woford, J.C.: Applied Numerical Methods for Digital Computation. 3rd ed., Harper & Row, 1985.
58. O'Neil, B.: Elementary Differential Geometry. Academic Press, 1966.
59. Struik, D.J.: Lectures on Classical Differential Geometry. 2nd ed., Addison-Wesley, 1961.
60. Hanna, J.R.: Fourier Series and Integrals of Boundary Value Problems. John Wiley & Sons, 1982.
61. Rahmat-Samii, Y.: A Generalized Reflector/Array Surface Compensation Algorithm for Gain and Sidelobe Control. IEEE 1987 Antennas and Propagation International Symposium Digest, Vol. 2, IEEE, 1986, pp. 760-763.
62. Cherrette, A.R., et al.: Compensation of a Reflector Antenna Surface Distortion Using an Array Feed. To be published in IEEE Trans. Antennas Propag., 1988.
63. Rahmat-Samii, Y., et al.: Realizable Feed-Element Patterns for Multibeam Reflector Antenna Analysis. IEEE Trans. Antennas Propag., vol. AP-29, no. 6, Nov. 1981, pp. 961-963.
64. Lee, S.W.; and Rahmat-Samii, Y.: Simple Formulas for Designing an Offset Multibeam Parabolic Reflector. IEEE Trans. Antennas Propag., vol. AP-29, no. 3, May 1981, pp. 472-478.

65. Cherrette, A.R., et al.: Compensation of Distorted Offset Parabolic Reflector Using an Array Feed. IEEE 1986 Antennas and Propagation International Symposium Digest, Vol. 2, IEEE, 1986, pp. 515-518.
66. Rudge, A.W.; and Davies, D.E.N.: Electronically Controllable Primary Feed for Profile-Error Compensation of Large Parabolic Reflectors. IEE Proc., vol. 117, no. 2, Feb. 1970, pp. 351-358.
67. Amitay, N.; and Zucker, H.: Compensation of Spherical Reflector Aberrations by Planar Array Feeds. IEEE Trans. Antennas Propag., vol. AP-20, no. 1, Jan. 1972, pp. 49-56.
68. Blank, S.J.; and Imbriale, W.A.: Array Feed Synthesis for Correction of Reflector Distortion and Vernier Beamsteering. Telecommunications and Data Acquisition Report, (JPL-TDA-PR-42-86, Jet Propulsion Lab.; NASA Contract NAS7-918) NASA CR-179715, Apr.-June 1986, pp. 43-55.
69. Watson, W.H.: The Field Distribution in the Focal Plane of a Paraboloidal Reflector. IEEE Trans. Antennas Propag., vol. AP-12, no. 5, Sept. 1964, pp. 561-569.
70. Midgley, D.: A Theory of Receiving Aerials Applied to the Reradiation of an Electromagnetic Horn. IEE Proc., vol. 108, pt. B, no. 42, Nov. 1961, pp. 645-650.
71. Visocekas, R.: Non-Cassegrain Indirect System for Aerial Illumination. Proc. IEE, vol. 111, 1964, pp. 1969-1975.
72. Minnett, H.C.; and Thomas, B.MacA.: Fields in the Image Space of Symmetrical Focusing Reflectors. Proc. IEE, vol. 115, no. 10, Oct. 1968, pp. 1419-1430.

73. Rudge, A.W.; and Withers, M.J.: Design of Flared-Horn Primary Feeds for Parabolic Reflector Antennas. Proc. IEE, vol. 117, no. 9, Sept. 1970, pp. 1741-1749.
74. Luh, H.H.S.: On the Radiation Pattern of a Multibeam Antenna. IEEE Trans. Antennas Propag., vol. AP-24, no. 1, Jan. 1976, pp. 101-102.
75. Rahmat-Samii, Y.; and Lee, S.W.: Application of the Conjugate Field Matching Technique to Reflector Antennas - A Critical Review. URSI Digest, 1981, p. 85.
76. Mrstik, A.V.; and Smith, P.G.: Scanning Capabilities of Large Parabolic Cylinder Reflector Antennas with Phased-Array Feeds. IEEE Trans. Antennas Propag., vol. AP-29, no. 3, May 1981, pp. 455-462.
77. Jong, H.Y., et al.: Analysis of Paraboloidal Reflector Fields Under Oblique Incidence. IEEE 1984 Antennas and Propagation International Symposium Digest, Vol. 1, IEEE, 1984, pp. 305-308.
78. Smetana, J.: Application of MMIC Modules in Future Multiple Beam Satellite Antenna Systems. NASA TM-83344, 1982.
79. Mauri, R.E.; and Crossman, F.W.: Space Radiation Effects on Structural Composites. AIAA Paper 83-0591, Jan. 1983.
80. Miller, J.B., et al.: Surface Control System for the 15 Meter Hoop-Column Antenna. NASA/DOD Control/Structures Interaction Technology 1986, R.L. Wright, ed., NASA CP-2447, Part 2, 1986, pp. 533-545.
81. Acosta, R.: Compensation of Reflector Surface Distortions Using Conjugate Field Matching. NASA TM-87198, 1986.

82. Rusch, W.V.T.; and Ludwig, A.C.: Determination of the Maximum Scan-Gain Contours of Beam-Scanning Paraboloid and Their Relation to the Petzval Surface. IEEE Trans. Antennas Propag., vol. AP-21, no. 2, Mar. 1973, pp. 141-147.
83. Lee, S.W.: Differential Geometry for GTD Application. EM Lab. Rep. 77-21, University of Illinois at Urbana-Champaign, Oct. 1977.

APPENDICES

APPENDIX A

POWER RADIATED BY AN ARRAY FEED

The generalized feed array geometry is illustrated in Fig. A-1. The feed position corresponding to the m th element is at (x_m, y_m, z_m) and its complex current excitation is I_m . The radiated electric field due to this element in the array can be expressed by,

$$\vec{E}_m(\vec{r}) \sim \frac{e^{-jKr}}{r} \vec{f}_m(\theta, \phi) \quad (\text{A.1})$$

where the vector function $\vec{f}_m(\theta, \phi)$ defines the m th element polarization and far-field radiation pattern. This vector function may be approximated by,

$$\vec{f}_m(\theta, \phi) = \hat{\theta} U E_m(\theta) (ae^{j\Psi} \cos \phi + b \sin \phi) + \hat{\phi} U H_m(\theta) (b \cos \phi - ae^{j\Psi} \sin \phi) \quad (\text{A.2})$$

where

$U E_m(\theta)$ E-plane pattern of the m th element

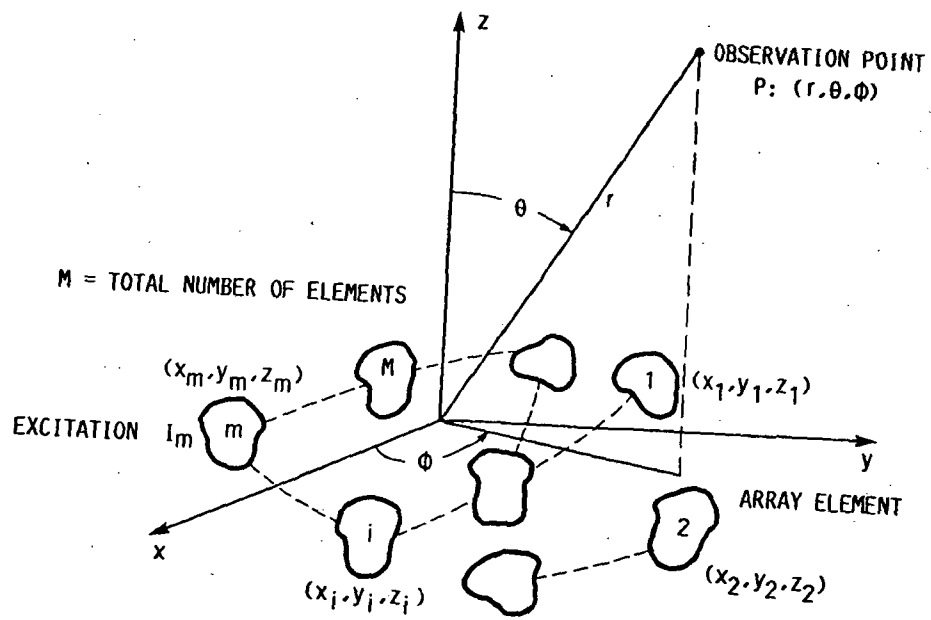
$U H_m(\theta)$ H-plane pattern of the m th element.

Typically, the far-field element patterns may be approximated by a $(\cos \theta)^q$ function, i.e.,

$$U E_m(\theta) = (\cos \theta)^q E \quad (\text{A.3a})$$

$$U H_m(\theta) = (\cos \theta)^q H \quad (\text{A.3b})$$

The radiated far-field of the feed array is the product of the element pattern given by A.1 and the array factor, i.e.,



A-1 Geometry of the generalized feed array

$$\vec{E}_{\text{array}}(r) = \sum_{m=1}^M \vec{E}_m(r) I_m e^{jK\hat{u} \cdot \vec{P}_m} \quad (\text{A.4})$$

where $\vec{E}_m(r)$ is given by A.1 and

$$\hat{u} = \sin \theta \cos \phi \hat{x} + \sin \theta \sin \phi \hat{y} + \cos \theta \hat{z} \quad (\text{A.5a})$$

$$\vec{P}_m = x_m \hat{x} + y_m \hat{y} + z_m \hat{z} \quad (\text{A.5b})$$

The total time-averaged radiated power of the array is given by,

$$P_{\text{rad}} = \frac{1}{Z_0} \int_0^{\pi/2} \int_0^{2\pi} \vec{E}_{\text{array}}(r) \cdot \vec{E}_{\text{array}}^*(r) r^2 \sin \theta d\theta d\phi \quad (\text{A.6})$$

where $\vec{E}_{\text{array}}(r)$ is the electric field radiated by the feed array given by A.4 and $Z = \sqrt{\mu/\epsilon} = 120 \pi$.

Substituting (A.4) into (A.6) we obtain

$$P_{\text{rad}} = \sum_{m=1}^M \sum_{n=1}^M \left\{ I_m I_n^* \frac{1}{Z_0} \int_0^{\pi/2} \int_0^{2\pi} \text{INTEGRAND}(m,n,\theta,\phi) d\theta d\phi \right\} \quad (\text{A.7a})$$

where

$$\text{INTEGRAND}(m,n,\theta,\phi) = \vec{E}_m(r) \cdot \vec{E}_n^*(r) e^{jK\hat{u} \cdot (\vec{P}_m - \vec{P}_n)} r^2 \sin \theta \quad (\text{A.7b})$$

Defining the power radiated as follows,

$$P_{\text{rad}} = \sum_{m=1}^M \sum_{n=1}^M I_m I_n^* A_{mn} \quad (\text{A.8})$$

where A_{mn} is given by the expression in the brackets of Eq. (A.7a).

It can be shown that,

$$\begin{aligned} E_m(r) \cdot E_n^*(r) = & \frac{1}{r^2} \left\{ \left(a^2 U E_m(\theta) U E_n^*(\theta) + b^2 U H_m(\theta) U H_n^*(\theta) \right) \cos^2 \phi \right. \\ & + \left(b^2 U E_m(\theta) U E_n^*(\theta) + a^2 U H_m(\theta) U H_n^*(\theta) \right) \sin^2 \phi \\ & \left. + ab \cos \phi \left(U E_m(\theta) U E_n^*(\theta) - U H_n(\theta) - U H_m(\theta) U H_n^*(\theta) \right) \sin 2\phi \right\} \quad (\text{A.9}) \end{aligned}$$

substituting (A.9) into (A.7b), then the expression for A_{mn} is given by

$$\begin{aligned}
 A_{mn} = \frac{1}{Z_0} \int_0^{\pi/2} \int_0^{2\pi} & \left\{ \left(a^2 U E_m(\theta) U E_n^*(\theta) + b^2 U H_m(\theta) U H_n^*(\theta) \right) \cos^2 \phi + \right. \\
 & + \left(b^2 U E_m(\theta) U H_n^*(\theta) + a^2 U H_m(\theta) U E_n^*(\theta) \right) \sin^2 \phi + ab \cos \psi \left(U E_m(\theta) U E_n^*(\theta) \right. \\
 & \left. \left. - U H_m(\theta) U H_n^*(\theta) \right) \sin 2 \phi \right\} \times e^{j K r_{mn} (\sin \theta_{mn} \sin \theta \cos (\phi - \phi_{mn})} \\
 & + \cos \theta_{mn} \cos \theta) \sin \theta \, d\theta \, d\phi
 \end{aligned} \tag{A.10a}$$

where

$$r_{mn} = \sqrt{(x_m - x_n)^2 + (y_m - y_n)^2 + (z_m - z_n)^2} \tag{A.10b}$$

$$\theta_{mn} = \cos^{-1} \left(\frac{z_m - z_n}{r_{mn}} \right) \tag{A.10c}$$

$$\phi_{mn} = \tan^{-1} \frac{y_m - y_n}{x_m - x_n} \tag{A.10d}$$

With the use of the following integration formulas,

$$\int_0^{2\pi} e^{j \xi \cos (\phi - \phi_c)} \, d\phi = 2\pi J_0(\xi) \tag{A.11a}$$

$$\int_0^{2\pi} \left\{ \begin{array}{l} \cos^2 \phi \\ \sin^2 \phi \end{array} \right\} e^{j \xi \cos (\phi - \phi_c)} \, d\phi = \pi J_0(\xi) \mp \pi \cos(2 \phi_c) J_2(\xi)$$

(A.11b)

The result after ϕ integration is reduced to

$$\begin{aligned}
A_{mn} = & \frac{\pi}{Z} \int_0^{\pi/2} \left(UE_m(\theta)UE_n^*(\theta) + UH_m(\theta)UH_n^*(\theta) \right) J_0(Kr_{mn} \sin \theta_{mn} \sin \theta) \\
& \times \sin \theta e^{jKr_{mn} \cos \theta_{mn} \cos \theta} d\theta + (1 - C_0) \int_0^{\pi/2} \left(UE_m(\theta)UE_n^*(\theta) \right. \\
& \left. - UH_m(\theta)UH_n^*(\theta) \right) J_2(Kr_{mn} \sin \theta_{mn} \sin \theta) \sin \theta e^{jKr_{mn} \cos \theta_{mn} \cos \theta} d\theta
\end{aligned} \tag{2-12a}$$

where

$$C_0 = 1 + 2ab \cos \psi \sin 2 \phi_{mn} + (a^2 - b^2) \cos 2 \phi_{mn} \tag{2-12b}$$

APPENDIX B

SPECULAR REFLECTION

For a given feed at point $P_1 (x_1, y_1, z_1)$ and an observation point $P_2 (x_2, y_2, z_2)$ (Fig. B.1), a reflection point O^r may exist on the reflector surface $(x, y, f(x, y))$. The vectors

$$d_1 = (x - x_1) x + (y - y_1) y + (z - z_1) z \quad (\text{B.1a})$$

$$d_2 = (x - x_2) x + (y - y_2) y + (z - z_2) z \quad (\text{B.1b})$$

are the connecting vectors between P_1 and O^r , and from O^r to P_2 , respectively. A necessary condition for which the reflection points must satisfy is that the total distance $(d_1 + d_2)$ must be stationary, i.e.,

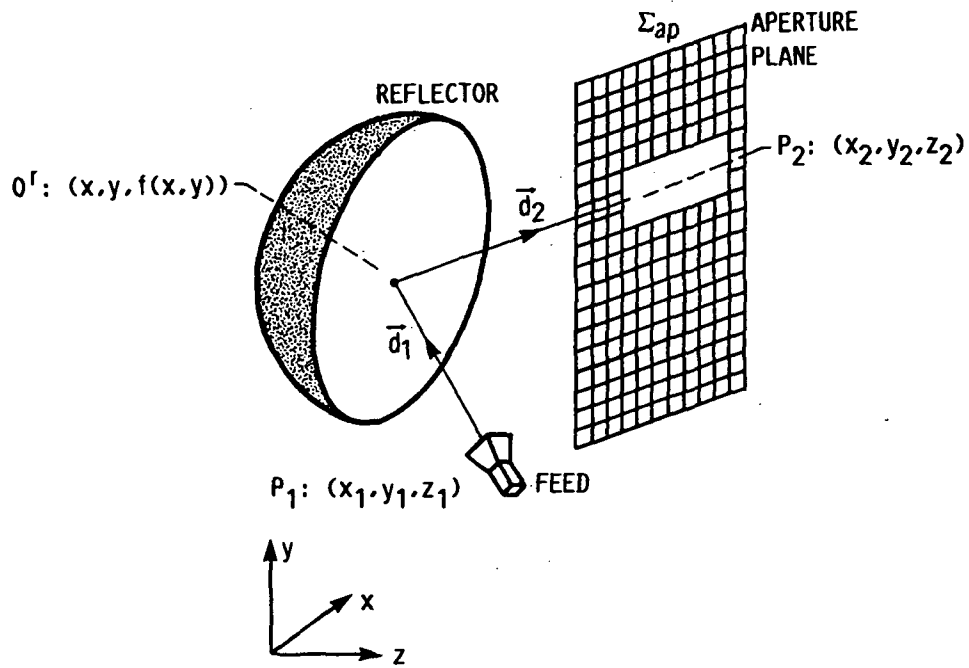
$$\frac{d}{dx} (d_1 + d_2) = 0 \quad \text{and} \quad \frac{d}{dy} (d_1 + d_2) = 0 \quad (\text{B.2})$$

after differentiation we obtain,

$$\frac{1}{d_1} (x - x_1) + (f(x, y) - z_1) \frac{df}{dx} + \frac{1}{d_2} (x - x_2) + (f(x, y) - z_2) \frac{df}{dx} = 0 \quad (\text{B.3a})$$

$$\frac{1}{d_1} (y - y_1) + (f(x, y) - z_1) \frac{df}{dy} + \frac{1}{d_2} (y - y_2) + (f(x, y) - z_2) \frac{df}{dy} = 0 \quad (\text{B.3b})$$

A root $(x, y, z = f(x, y))$ of the two nonlinear equations in (B.3a) and (b) gives location of a reflection point. For a given point P_1 and P_2 , there may be none, one, or more than one reflection point. It may be shown that (B.3a) and (b) is equivalent to satisfying Snell's law of reflection (Ref. 6).



B.1 Geometry for the specular reflection calculation

The system of Eqs. (B.3a), and (b) can also be satisfied if P_1 , O^r , and P_2 are collinear. Such an unwanted root may be eliminated by imposing an additional condition.

$$\left(\frac{x - x_1}{d_1} + \frac{x - x_2}{d_2}\right)^2 + \left(\frac{y - y_1}{d_1} + \frac{y - y_2}{d_2}\right)^2 + \left(\frac{z - z_1}{d_1} + \frac{z - z_2}{d_2}\right)^2 > \epsilon \quad (\text{B.4})$$

where ϵ is a small positive number. One can preset $\epsilon = 0.00001$. A root of (B.1) may or may not fall inside the boundary of the reflector. Each root $(x, y, f(x, y))$ must be checked if it is inside the desired boundary.

APPENDIX C

PRINCIPAL RADII OF CURVATURES OF THE REFLECTED WAVEFRONT

Differential Geometry (Ref. 83) forms the basis of the computation of principal curvatures of the reflected wavefront (R_1^r, R_2^r) . The three orthonormal base vector of the incident ray bundle are chosen to be (Fig. C-1)

$$\hat{x}_1^i = \frac{\hat{y} \times \hat{x}_3}{|\hat{y} \times \hat{x}_3|} = \frac{\hat{x}(z - z_1) - \hat{z}(x - x_1)}{\sqrt{(z - z_1)^2 + (x - x_1)^2}} \quad (\text{C.1a})$$

$$\hat{x}_2^i = \frac{\hat{x}_3^i \times \hat{x}_1^i}{|\hat{x}_3^i \times \hat{x}_1^i|} \quad (\text{C.1b})$$

$$\hat{x}_3^i = \frac{\hat{x}(x - x_1) + \hat{y}(y - y_1) + \hat{z}(z - z_1)}{\sqrt{(x - x_1)^2 + (y - y_1)^2 + (z - z_1)^2}} \quad (\text{C.1c})$$

where (x, y, z) are the coordinates of the reflection point O^r . The reflected orthonormal unit base vectors are given by

$$\hat{x}_1^r = \hat{x}_1^i - 2(\hat{x}_1^i \cdot \hat{n}) \hat{n} \quad (\text{C.2a})$$

$$\hat{x}_2^r = \hat{x}_2^i - 2(\hat{x}_2^i \cdot \hat{n}) \hat{n} \quad (\text{C.2b})$$

$$\hat{x}_3^r = \frac{\hat{x}(x_2 - x) + \hat{y}(y_2 - y) + \hat{z}(z_2 - z)}{\sqrt{(x_2 - x)^2 + (y_2 - y)^2 + (z_2 - z)^2}} \quad (\text{C.2c})$$

The vectors (C.2a) to (c) are chosen to satisfy a left-hand system, i.e., $\hat{x}_1^r \times \hat{x}_2^r = -\hat{x}_3^r$. This selection is invariant with respect to the

reflected curvatures (R_1^r, R_2^r). The three orthonormal base vectors of the reflector surface at O^r are chosen to be

$$\hat{x}_1^s = \frac{\hat{x} + \hat{z} f_x}{\sqrt{(1 + f_x^2)}} \quad (\text{C.3a})$$

$$\hat{x}_2^s = \frac{\hat{x}_3^s \times \hat{x}_1^s}{|\hat{x}_3^s \times \hat{x}_1^s|} \quad (\text{C.3b})$$

$$\hat{x}_3^s = \hat{n} = \frac{-f_x \hat{x} - f_y \hat{y} + \hat{z}}{\sqrt{(f_x^2 + f_y^2 + 1)}} \quad (\text{C.3c})$$

where

$$f_x = \frac{d f(x,y)}{dx} \quad (\text{C.3d})$$

$$f_y = \frac{d f(x,y)}{dy} \quad (\text{C.3e})$$

$$z = f(x,y) \text{ reflector surface function} \quad (\text{C.3f})$$

Let define the following parameters be defined,

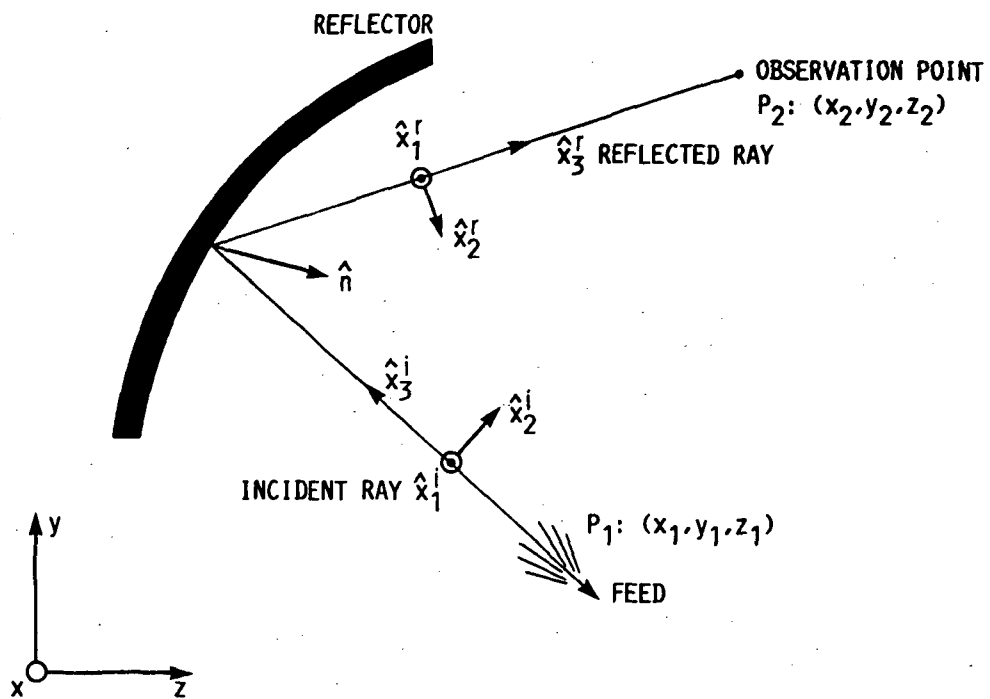
$$P_{mn}^i = \hat{x}_m^i \cdot \hat{x}_n^s \quad m = 1,2,3, \quad n=1,2,3. \quad (\text{C.4})$$

Substituting Eqs. (C.1a) to (c) and (C.3a) to (c) into (C.4) we obtain,

$$P_{11}^i = \frac{(z - z_1) - f_x(x - x_1)}{\sqrt{(1 + f_x^2)} \sqrt{((x - x_1)^2 + (z - z_1)^2)}} \quad (\text{C.5a})$$

$$P_{12}^i = \frac{-f_y(x - x_1) + f_x(z - z_1)}{\sqrt{\Delta(1 + f_x^2)} \sqrt{[(x - x_1)^2 + (z - z_1)^2]}} \quad (\text{C.5b})$$

$$P_{21}^i = \frac{-(x - x_1)(y - y_1) - f_x(y - y_1)(z - z_1)}{\sqrt{(1 + f_x^2)} \sqrt{\{(x - x_1)^2 (y - y_1)^2 + [(z - z_1)^2 + (x - x_1)^2]^2 + (y - y_1)^2 (z - z_1)^2\}}} \quad (\text{C.5c})$$



C.1 Principal vector directions of the incident and reflected rays

$$P_{22}^i = \frac{f_x f_y (x - x_1)(y - y_1) + (1 + f_x) [(z - z_1)^2 + (x - x_1)^2] - f_y (y - y_1)(z - z_1)}{\sqrt{\Delta(1 + f_x^2)} \sqrt{\{(x - x_1)^2 (y - y_1)^2 + [(z - z_1)^2 + (x - x_1)^2]^2 + (y - y_1)^2 (z - z_1)^2\}}} \quad (\text{C.5d})$$

$$P_{33}^i = \frac{1}{d_1} \Delta (f_x (x - x_1) + f_y (y - y_1) - (z - z_1)) \quad (\text{C.5e})$$

where

$$\Delta = (f_x^2 + f_y^2 + 1)^{-1/2} \quad (\text{C.5f})$$

Let the 2x2 matrix \bar{P}^i be defined for the first four parameters in Eq. (C.5a) to (d). If we define another set of parameters by the following definition,

$$P_{mn}^r = \hat{x}_m^r \cdot \hat{x}_n^s \quad m=1,2,3 \quad \text{and} \quad n=1,2,3 \quad (\text{C.6})$$

it can be shown that

$$P_{11}^r = P_{11}^i \quad (\text{C.7a})$$

$$P_{12}^r = P_{12}^i \quad (\text{C.7b})$$

$$P_{21}^r = P_{21}^i \quad (\text{C.7c})$$

$$P_{22}^r = P_{22}^i \quad (\text{C.7d})$$

The curvature matrix of incident ray bundle is given by

$$\bar{Q}^i = \begin{bmatrix} d_1^1 & 0 \\ 0 & d_1^{-1} \end{bmatrix} \quad (\text{C.8})$$

The curvature matrix of the reflector surface at the reflecting point is given by

$$\bar{Q}^S = \begin{bmatrix} e\Delta^2(G - F^2/E) & \Delta(eF - fE)/E \\ \Delta(eF - fE)/E & \Delta^2(gE - 2fF + eF^2/E) \end{bmatrix} \quad (C.9)$$

where

$$\begin{aligned} E &= 1 + f_x^2, & F &= f_x f_y, & G &= 1 + f_y^2 \\ e &= -\Delta f_{xx}, & f &= -\Delta f_{xy}, & g &= \Delta f_{yy} \\ f_{xx} &= \frac{d^2 f(x,y)}{dx^2}, & f_{xy} &= \frac{d^2 f(x,y)}{dx dy}, & f_{yy} &= \frac{d^2 f(x,y)}{dy^2} \end{aligned}$$

The desired reflected curvature matrix \bar{Q}^r may be computed from the following equation

$$\bar{Q}^r = \bar{Q}^i + 2 P_{33}^i ((\bar{P}^i)^T)^{-1} \bar{Q}^S (\bar{P}^i)^{-1} \quad (C.10)$$

in general \bar{Q}^r is a 2x2 matrix, with elements denoted by Q_{11} , Q_{12} , Q_{21} and Q_{22} .

Then radii of curvature of the reflected wavefront is given by the following expression,

$$\frac{1}{R_1^r}, \frac{1}{R_2^r} = \frac{1}{2} \left\{ (Q_{11} + Q_{22}) \pm \sqrt{(Q_{11} + Q_{22})^2 - 4(Q_{11}Q_{22} - Q_{12}Q_{21})} \right\} \quad (C.11)$$

APPENDIX D

FOCAL PLANE FIELDS COMPUTATION BY THE RECIPROCITY PRINCIPLE

It is required to calculate the focal plane electric field at point 1 produced by an incident uniform plane wave (Fig. (D-1)) from an observation direction $(\theta_{\text{BEAM}}, \phi_{\text{BEAM}})$. It is assumed that the uniform plane wave is generated by a dipole source located at point 2 in the far field of the distorted reflector antenna. The dipole source at point 2 has the following current distribution,

$$\vec{J}_2(\vec{r}) = \hat{u}_2 \delta(\vec{r} - \vec{r}_2) \quad (\text{D.1})$$

where \hat{u}_2 is a unit vector describing the polarization of the dipole. In the neighborhood of any distorted reflector surface point the incident field is a local uniform plane wave. This uniform plane wave can be described by,

$$E^i = \hat{u}_2 e^{+j\vec{K} \cdot \vec{r}} \quad (\text{D.2})$$

where

$$\vec{r} = x \hat{x} + y \hat{y} + z \hat{z}$$

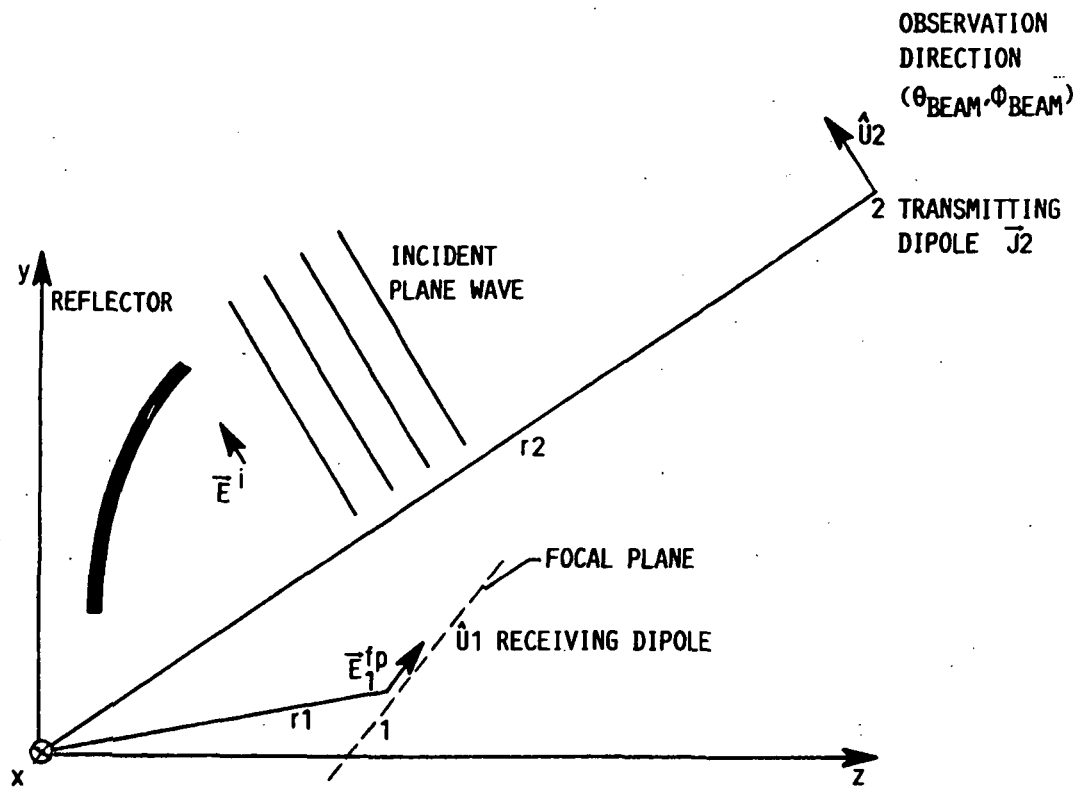
(x, y, z) any point on the distorted reflector surface

$$\vec{K} = K (\sin \theta \cos \phi \hat{x} + \sin \theta \sin \phi \hat{y} + \cos \theta \hat{z})$$

$$\theta = \theta_{\text{BEAM}} \quad \text{and} \quad \phi = \phi_{\text{BEAM}}$$

$$K = 2\pi/\lambda$$

the received focal plane field at point 1 is denoted by,



D.1 Uniform plane wave incident on the reflector surface

$$\vec{E}_1^{fP}(\vec{r}_1), \quad \vec{H}_1^{fP}(\vec{r}_1) \quad (D.3)$$

Let us now assume that the distorted reflector is being considered in the transmitting mode with a dipole source \vec{J}_1 located at point 1 in the focal plane of the reflector (Fig. D.2). The dipole source at point 1 have the following current distribution

$$\vec{J}_1(\vec{r}) = \hat{u}_1 \delta(\vec{r} - \vec{r}_1) \quad (D.4)$$

where \hat{u}_1 is a unit vector describing the transmitting polarization of the dipole source in the focal plane. With this dipole as the radiating element, the distorted antenna produces a far zone electric field at point 2 denoted by

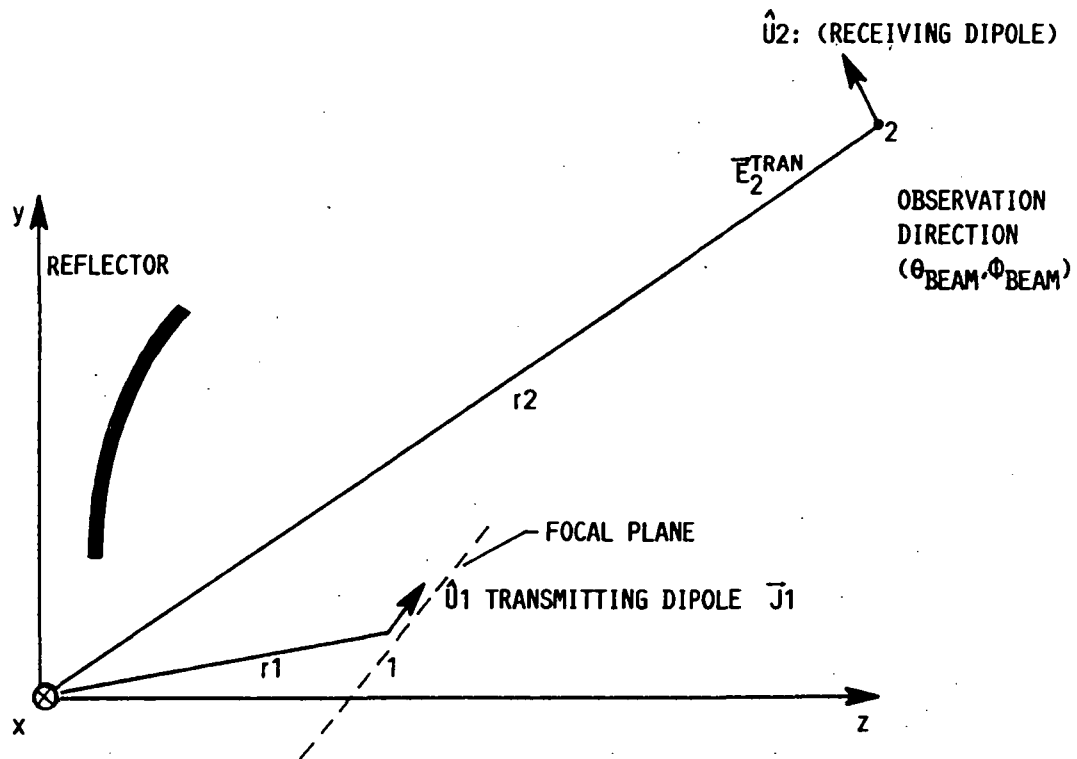
$$\vec{E}_2^{tran}(\vec{r}_2), \quad \vec{H}_2^{tran}(\vec{r}_2) \quad (D.5)$$

The Lorentz reciprocity theorem relates the transmitting fields on Eqs. (D.3) and (D.5) with the respective sources described by Eqs. (D.1) and (D.4) respectively. Mathematically the reciprocity principle can be expressed as follows,

$$\begin{aligned} & \int_S \int [\vec{E}_1^{fP} \cdot \vec{H}_2^{trans} - \vec{E}_2^{trans} \cdot \vec{H}_1^{fP}] \cdot dS = \\ & \iiint_V [\vec{E}_1^{fP} \cdot \vec{J}_2 - \vec{E}_2^{trans} \cdot \vec{J}_1 + \vec{H}_2^{trans} \cdot \vec{M}_1 - \vec{H}_1^{fP} \cdot \vec{M}_2] dv \quad (D.6) \end{aligned}$$

for the particular case under consideration one can use the following assumptions,

$$\vec{M}_1 = \vec{M}_2 = 0 \quad \text{and} \quad \vec{H}_1^{fP} = -\frac{\vec{E}_1^{fP} \times \hat{r}}{Z}, \quad \vec{H}_2^{tran} = -\frac{\vec{E}_2^{tran} \times \hat{r}}{Z} \quad (D.7)$$



D.2 Illumination of the reflector surface by a dipole source on the focal plane

under this assumptions the following result is obtained.

$$0 = \iiint_V [\vec{E}_1^{fp} \cdot \vec{J}_2 - \vec{E}_2^{tran} \cdot \vec{J}_1] dv \quad (D.8)$$

substituting Eq. (D.1) and (D.4) into Eq. (D.8) yields the final result,

$$\vec{E}_1^{fp} \cdot \hat{u}_2 = \vec{E}_2^{tran} \cdot \hat{u}_1 \quad (D.9)$$

This result shows that by reciprocity, the focal plane fields produced by an incident uniform plane wave on the distorted reflector surface can be obtained indirectly from the far zone electric field generated by a dipole source at a specified location in the focal plane of the distorted reflector.



Report Documentation Page

1. Report No. NASA TM-100826		2. Government Accession No.		3. Recipient's Catalog No.	
4. Title and Subtitle Active Feed Array Compensation for Reflector Antenna Surface Distortions				5. Report Date June 1988	
				6. Performing Organization Code	
7. Author(s) Roberto J. Acosta				8. Performing Organization Report No. E-4015	
				10. Work Unit No. 650-60-20	
9. Performing Organization Name and Address National Aeronautics and Space Administration Lewis Research Center Cleveland, Ohio 44135-3191				11. Contract or Grant No.	
				13. Type of Report and Period Covered Technical Memorandum	
12. Sponsoring Agency Name and Address National Aeronautics and Space Administration Washington, D.C. 20546-0001				14. Sponsoring Agency Code	
15. Supplementary Notes <p>This report is a dissertation presented to The University of Akron in partial fulfillment of the requirements for the degree Doctor of Philosophy in May 1988.</p>					
16. Abstract <p>The feasibility of electromagnetic compensation for reflector antenna surface distortions (non-random) is investigated. The performance characteristics (gain, sidelobe levels, etc.) of large satellite communication reflector antenna systems degrade as the reflector surface distorts, mainly due to thermal effects from a solar radiation. The technique developed in this dissertation can be used to maintain the antenna boresight directivity and sidelobe level independent of thermal effects on the reflector surface. With the advent of monolithic micro-wave integrated circuits (MMIC), a greater flexibility in array-fed reflector antenna systems can be achieved. MMIC arrays provide independent control of amplitude and phase for each of the many radiating elements in the feed array. By assuming a known surface distortion profile, a simulation study is carried out to examine the antenna performance as a function of feed array size and number of elements. Results indicate that the compensation technique can effectively control boresight directivity (within 1-3 dB of the undistorted) and sidelobe level (within 1-5 dB of the undistorted) under peak surface distortion in the order of tenth of a wavelength. Furthermore, the computational ease of the compensation technique allows it to be implemented adaptively in a large satellite reflector antenna system.</p>					
17. Key Words (Suggested by Author(s)) Compensation; Distorted antenna; Radiation pattern; Feed array; Conjugate field matching			18. Distribution Statement Unclassified - Unlimited Subject Category 32		
19. Security Classif. (of this report) Unclassified		20. Security Classif. (of this page) Unclassified		21. No of pages 178	22. Price* A09

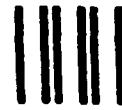
National Aeronautics and
Space Administration

Lewis Research Center
Cleveland, Ohio 44135

Official Business
Penalty for Private Use \$300

SECOND CLASS MAIL

ADDRESS CORRECTION REQUESTED



Postage and Fees Paid
National Aeronautics and
Space Administration
NASA-451

NASA
